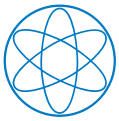

Technische Universität München

TUM School of Natural Sciences

Equilibrium and initial value problem simulation studies of nonlinear magnetohydrodynamics in stellarators

Rohan Ramasamy

Vollständiger Abdruck der von der TUM School of Natural Sciences der Technischen Universität München zur Erlangung des akademischen Grades eines

Doktors der Naturwissenschaften

genehmigten Dissertation.

Vorsitzende:	Prof. Dr. Katharina Krischer
Prüferinnen der Dissertation:	1. Hon.-Prof. Dr. Sibylle Günter
	2. Prof. Dr. Josefine Proll

Die Dissertation wurde am 23.08.2022 bei der Technischen Universität München eingereicht und durch die TUM School of Natural Sciences am 02.11.2022 angenommen.

DEPARTMENT OF PHYSICS

TECHNISCHE UNIVERSITÄT MÜNCHEN

Equilibrium and initial value problem simulation studies of nonlinear magnetohydrodynamics in stellarators

Author:	Rohan Ramasamy
Supervisor:	Hon.-Prof. Dr. Sibylle Günter
Advisors:	Dr. Matthias Hoelzl
Submission Date:	23.08.2022

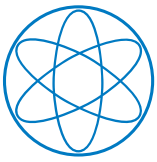

For Ammamma

Abstract

Macroscopic current driven magnetohydrodynamic (MHD) instabilities pose a significant threat to the viability of reactor relevant tokamak scenarios. While stellarators are generally considered to have much milder MHD stability properties than tokamaks, because of the reduction or removal of the toroidal plasma current carried in such devices, there are still unanswered questions regarding their nonlinear MHD stability limits. In particular for the context of this work, quasi-axisymmetric (QA) stellarator concepts feature bootstrap currents comparable to tokamaks. These currents could re-introduce the problem of nonlinear MHD stability to the optimisation process of such stellarators. The main purpose of this work is to use existing MHD codes to gain an understanding of the dynamics of current carrying stellarators. Particular attention is given to low n external kink modes, where n defines the toroidal mode number of the instability. These global instabilities limit the operational space of QA devices. How such modes are modified by the introduction of an external rotational transform, produced through loosely wound helical field coils, is the main research question of interest.

The work can be divided into three parts. In the first part, the ideal MHD equilibrium code, VMEC, is used to study saturated external kink modes in tokamaks and classical $l = 2$ stellarators. As this method has never been compared with an initial value problem approach for external modes, tokamak computations are first compared against results from the nonlinear MHD code, JOREK. It is shown that the two approaches compare favourably, especially in the case where the MHD dynamics are dominated by a single MHD instability. The approach is then extended to consider external MHD modes in $l = 2$ stellarators, where l refers to the poloidal periodicity number of the external field coils. This provides a full MHD interpretation of how the dynamics of external kink modes can change with the introduction of an external rotational transform.

In the second part, a nonlinear approach is developed within the JOREK code to simulate stellarators axisymmetrically. This method is based on the well known stellarator expansion and has a long history of use in the stellarator community as a first approximation of MHD dynamics. The model is first tested against a variety of ideal and resistive MHD instabilities. It is shown that the fully non-axisymmetric growth rates of resistive instabilities modelled linearly in Wendelstein 7-X (W7-X) can be captured by this model, and reasonable agreement is obtained for the linear growth rates of external kink modes in a candidate QA stellarator. The current in this stellarator is 8.25 MA, which trig-

gers strong external MHD activity at low order rational surfaces lying just outside the confined region. Simulations of the QA stellarator are then continued into the nonlinear regime to gain a first understanding of whether the relatively weak external rotational transform of this configuration is sufficient to stabilise the MHD dynamics triggered by the linearly unstable mode. Violent MHD dynamics are still observed which would lead to a significant loss of confinement. In order to understand how much current needs to be removed to stabilise the mode, artificial stellarator approximations are made by incrementally removing more plasma current from the simulated device, such that the external rotational transform is increased. It is shown that the MHD dynamics are only significantly stabilised when nonlinearly triggered internal MHD activity in the plasma mid-region is avoided. This occurs after most of the plasma current is removed from the device.

In the final part of this work, steps are made towards fully non-axisymmetric simulations of stellarators using JOREK. These numerical developments are separate from the physics studies in previous sections. The grid structure in JOREK is modified to handle non-axisymmetric grids enabling stellarator simulations in full 3D geometry. An initial study of tearing and ballooning modes is then designed, based on the experimental observations of such modes in the classical stellarator Wendelstein 7-A (W7-A). The linear verification of this instability against CASTOR3D builds confidence in using this approach to model optimised stellarators in the future.

Zusammenfassung

Makroskopische stromgetriebene MHD-Instabilitäten stellen eine erhebliche Bedrohung für die Realisierbarkeit von reaktorrelevanten Tokamak-Szenarien dar. Während Stellaratoren im Allgemeinen wesentlich mildere MHD-Stabilitätseigenschaften haben als Tokamaks, da der toroidale Plasmastrom in diesen Geräten fehlt oder reduziert ist, gibt es immer noch offene Fragen bezüglich ihrer nichtlinearen MHD-Stabilitätsgrenzen. Insbesondere relevant für den Kontext dieser Arbeit, weisen quasi-axialsymmetrische (QA) Stellaratorkonzepte mit Tokamaks vergleichbare Bootstrap Ströme auf. Diese Ströme erfordern die Berücksichtigung nichtlinearer MHD-Stabilität in den Optimierungsprozessen solcher Stellaratoren. Das Hauptziel dieser Arbeit besteht darin, bestehende MHD-Codes zu nutzen, um ein Verständnis der Dynamik von stromführenden Stellaratoren zu gewinnen. Ein besonderes Augenmerk liegt dabei auf externe Kink-Moden mit niedriger toroidaler Modenzahl und deren Auswirkung auf den Betriebsbereich von QA-Stellatoren. Wie solche Moden durch die Einführung einer externen Rotationstransformation verändert werden, die durch lose gewickelte helikale Spulen erzeugt wird, ist die wichtigste Forschungsfrage von Interesse.

Die Arbeit lässt sich in drei Teile gliedern. Im ersten Teil wird der ideale MHD-Gleichgewichts-Code, VMEC, verwendet, um gesättigte externe Kink-Moden in Tokamaks und klassischen $l = 2$ Stellaratoren zu untersuchen. Da diese Methode zuvor noch nicht mit der Lösung eines Anfangswertproblems für externe Moden verglichen wurde, werden zunächst Tokamak-Berechnungen mit Ergebnissen aus dem nichtlinearen MHD-Code JOREK verglichen. Es wird gezeigt, dass die beiden Ansätze generell vergleichbare Ergebnisse liefern, insbesondere wenn die MHD-Dynamik von einer einzigen MHD-Instabilität dominiert wird. Der Ansatz wird dann erweitert, um externe MHD-Moden in $l = 2$ Stellaratoren. Dies ermöglicht eine vollständige MHD-Interpretation der Dynamik externer Kink-Moden unter Einführung einer externen Rotationstransformation.

Im zweiten Teil wird ein nichtlinearer Ansatz innerhalb des JOREK-Code entwickelt, um Stellaratoren axialsymmetrisch zu simulieren. Diese Methode basiert auf der bekannten Stellarator-Expansion und wird in der Stellarator-Gemeinschaft schon seit langem als erste Annäherung an die MHD-Dynamik verwendet. Das Modell wird zunächst an einer Reihe von idealen und resistiven MHD-Instabilitäten getestet. Es wird gezeigt, dass die Wachstumsraten von resistiven Instabilitäten in Wendelstein 7-X (W7-X), mit diesem Modell reproduziert werden. Auch eine angemessene Übereinstimmung für die lin-

earen Wachstumsraten externer Kink-Moden in einem QA-Stellarator-Kandidaten wird gezeigt. Der Strom in diesem Stellarator beträgt 8,25 MA, was eine starke externe MHD-Aktivität an einer q = 2 Oberfläche auslöst, die direkt außerhalb der eingeschlossenen Plasma-Region liegt. Die Simulationen des QA-Stellarators werden dann in das nichtlineare Regime fortgesetzt, um ein erstes Verständnis dafür zu gewinnen, ob die in diesem Fall relativ schwache externe Rotationstransformation ausreicht, um die MHD-Dynamik zu stabilisieren. Es werden immer noch starke MHD-Dynamiken beobachtet, die zu einem erheblichen Verlust des Plasma-Einschlusses führen würden. Um zu verstehen, wie viel Strom entfernt werden muss, um die Moden zu stabilisieren, werden künstliche Stellarator-Näherungen vorgenommen, indem schrittweise mehr Plasmastrom aus dem simulierten Gerät entfernt und die externe Rotations-Transformation entsprechend erhöht wird. Es wird gezeigt, dass die MHD-Dynamik nur signifikant stabilisiert wird, wenn die nichtlinear getriebene interne MHD-Aktivität in der Plasmamittelregion stabilisiert ist. Dies geschieht, wenn der größte Teil des Plasmastroms entfernt wurde.

Im letzten Teil dieser Arbeit werden Schritte zur vollständig nicht-axialsymmetrischen Simulation von Stellaratoren mit JOREK erläutert. Diese numerischen Entwicklungen sind unabhängig von den physikalischen Studien in den vorangegangenen Abschnitten. Die Gitterstruktur in JOREK wird so modifiziert, dass sie nicht-axialsymmetrische Gitter handhaben kann, um Stellarator-Simulationen in vollständiger 3D-Geometrie zu ermöglichen. Eine erste Studie zu Tearing- und Ballooning- Moden auf der Grundlage der experimentellen Beobachtungen am klassischen Stellarator Wendelstein 7-A (W7-A) wird gezeigt. Der lineare Vergleich dieser Instabilitäten mit CASTOR3D stärkt das Vertrauen in die künfige Verwendung dieses Ansatzes zur Modellierung optimierter Stellaratoren.

List of publications

Publications in peer-reviewed journals

- **R. Ramasamy**, G. Bustos Ramirez, M. Hoelzl, J. Graves, G. Suárez López, K. Lackner, S. Günter, and JOREK team. Modelling of saturated external MHD instabilities in tokamaks: a comparison of 3D free boundary equilibria and nonlinear stability calculations. Physics of Plasmas 29, 072303, 2022. https://doi.org/10.1063/5.0090008
- **R. Ramasamy**, M. Hoelzl, E. Strumberger, K. Lackner, and S. Günter. Nonlinear MHD simulations of external kinks in quasi-axisymmetric stellarators using an axisymmetric external rotational transform approximation. Nuclear Fusion, 61(7), 076017, 2021. https://doi.org/10.1088/1741-4326/abffdf
- N. Nikulsin, **R. Ramasamy**, M. Hoelzl, F. Hindenlang, E. Strumberger, K. Lackner, and S. Günter. JOREK3D: An extension of the JOREK nonlinear MHD code to stellarators. Physics of Plasmas, 29.(6):063901, 2022. doi:10.1063/5.0087104
- M. Hoelzl, G.T.A. Huijsmans, S.J.P. Pamela, M. Béecoulet, E. Nardon, F.J. Artola, B. Nkonga, C.V. Atanasiu, V. Bandaru, A. Bhole, D. Bonfiglio, A. Cathey, O. Czarny, A. Dvornova, T. Fehér, A. Fil, E. Franck, S. Futatani, M. Gruca, H. Guillard, J.W. Haverkort, I. Holod, D. Hu, S.K. Kim, S.Q. Korving, L. Kos, I. Krebs, L. Kripner, G. Latu, F. Liu, P. Merkel, D. Meshcheriakov, V. Mitterauer, S. Mochalskyy, J.A. Morales, R. Nies, N. Nikulsin, F. Orain, J. Pratt, **R. Ramasamy**, P. Ramet, C. Reux, K. Särkimäki, N. Schwarz, P. Singh Verma, S.F. Smith, C. Sommariva, E. Strumberger, D.C. van Vugt, M. Verbeek, E. Westerhof, F. Wieschollek and J. Zielinski. The JOREK non-linear extended MHD code and applications to large-scale instabilities and their control in magnetically confined fusion plasmas. Nuclear Fusion, 61(6):065001, 2021. doi:10.1088/1741-4326/abf99f.

Contributions at conferences, seminars, and workshops

- Talk: R. Ramasamy, M. Hoelzl., K. Lackner, S. Günter. Studying saturated external kink modes in tokamaks and $l = 2$ stellarators using VMEC, Spectaculars Meeting (August 2022, Virtual)
- Poster: R. Ramasamy, N. Nikulsin, K. Aleynovika, M. Hoelzl, F. Hindenlang, E. Strumberger, K. Lackner, S. Günter and the JOREK team. Towards nonlinear MHD simulations of optimised stellarators, 23nd Int. Stellarator and Heliotron Workshop (June 2022, Warsaw, Poland)
- Talk: R. Ramasamy, M. Hoelzl, E. Strumberger, S. Henneberg, G. Suárez López, K. Lackner and S. Günter and the JOREK Team, Simplified nonlinear

MHD models of external kink modes in stellarators, DPG Meeting of the Matter and Cosmos Section, (September 2021, Virtual).

- Talk: R. Ramasamy, M. Hoelzl, E. Strumberger, Q. Yu, K. Lackner, and S. Günter, Nonlinear MHD assessments of Quasi-Axisymmetric Stellarators using an axisymmetric approximation, JOREK Seminar (November 2020, Virtual)

- Poster: R. Ramasamy, M. Hoelzl, E. Strumberger, Q. Yu, K. Lackner, S. Günter and the JOREK team. Non-linear MHD stability assessments of stellarators using an axisymmetric approximation, Theory of Fusion Plasmas, Joint Varenna-Lausanne International Workshop, Lausanne, Switzerland (October 2020, Virtual)

- Poster: R. Ramasamy, M. Hoelzl, E. Strumberger, N. Nikulsin, K. Lackner and S. Günter. Towards linear and non-linear assessments of quasi-axisymmetric stellarators, 22nd Int. Stellarator and Heliotron Workshop (September 2019, Madison, USA) (https://uwmadison.eventsair.com/ishw19/)

Contents

1 Introduction

This thesis is concerned with the development and use of numerical models for the nonlinear analysis of magnetohydrodynamic (MHD) instabilities in stellarators - non-axisymmetric, toroidal magnetic confinement systems that are one of the main prospects for developing a viable fusion reactor [1]. Conventional wisdom states that optimised stellarators are very likely to be free from disruptions - strong MHD activity that can lead to a sudden complete loss of confinement [2–4]. For this reason, it is worth asking at the outset of this work, why does the magnetic confinement fusion community need to develop nonlinear codes for modelling MHD activity in such devices?

To answer this question, a brief summary of the context of MHD research in stellarators follows. The meaning and nature of magnetic confinement is outlined in Section 1.1, as an introduction to the physical systems that are of interest herein - tokamaks and stellarators. The current prospects for developing a fusion reactor from such devices is considered in Section 1.2. This leads naturally onto the question of MHD stability, which is one of the root causes of their performance limits. In Section 1.3, the main instabilities that have been modelled as part of this thesis are discussed, highlighting their relevance to stellarators. Section 1.4 turns to the value of using numerical approaches to model such instabilities, in order to understand them. A strategy is outlined within the community around the nonlinear MHD code JOREK for developing and using such numerical methods to model stellarators, and understand the nature of observed and predicted MHD activity. In Section 1.5, the structure of the remainder of the thesis is outlined.

1.1 Magnetic confinement in tokamaks and stellarators

The objective of magnetic confinement research is to confine a hot plasma at sufficiently high density for an appreciable amount of time, such that the fusion reaction rate is sufficient to enable an economically viable reactor. Magnetic confinement relies on the principle that a magnetised plasma, being an ionised gas whose motion is governed by collective behaviour [5], is tied to the magnetic field it moves through, due to the Lorentz force [6]. As a result, particles are free to move parallel to the magnetic field, but are constrained in their perpendicular motion, such that they gyrate around the magnetic field lines. In this way, it is possible to significantly reduce the transport of thermal energy and particles perpendicular to the magnetic field.

While there are straight magnetic confinement concepts, such as magnetic mirrors

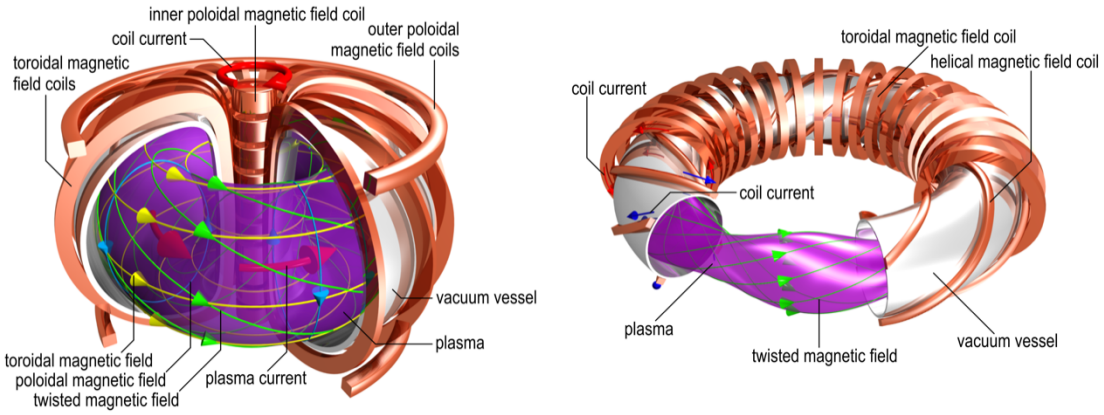

(a) (b)

Figure 1.1: Sketch of a typical tokamak configuration (a) and a classical $l = 2$ stellarator (b). The tokamak has an axisymmetric geometry, with planar toroidal and poloidal field coils, relying on plasma current to generate the poloidal component of the helical magnetic field within the torus. In contrast, the classical stellarator uses plasma current and helical coils to generate the complete field. Reproduced from IPP.

[7], typically the magnetic field is bent into a torus in order to solve the problem of significant end losses, through unconstrained parallel transport along the magnetic field. On the other hand, it can be shown that a simple torus with a purely toroidal magnetic field has poor particle confinement as a result of drift motions [8]. As a result, a helical field is needed to confine the plasma. In such devices, the magnetic field winds around the toroidally confined region, such that particle trajectories cover a radially localised region of the plasma volume. If the device is designed well, the magnetic topology, or field structure, will form a series of nested flux surfaces, as shown in Section 1.3.2. The winding of the helical field is characterised by the rotational transform, $\iota/2\pi$, which gives the average number of poloidal turns completed by a field line, per toroidal transit around the torus. Alternatively, its inverse, called the safety factor, q, can be used to describe the winding. These quantities are important in MHD stability theory, as will be shown in Chapter 2.

The above design constraint leads to two closely related concepts for a fusion reactor — tokamaks and stellarators, sketched in Figure 1.1. In order to produce the required helical field, tokamaks, shown in Figure 1.1 (a), make use of a toroidal plasma current to generate the required poloidal magnetic field. The toroidal magnetic field, and axisymmetric poloidal shaping of the plasma column are generated using relatively simple planar field coils. As a result, the geometry is near-axisymmetric, subject to the finite number of toroidal field coils that create the approximately axisymmetric toroidal magnetic field.

Early classical stellarators were designed using helical coils of a certain poloidal field number, l, to generate a helical ripple around the torus. The helical ripple is

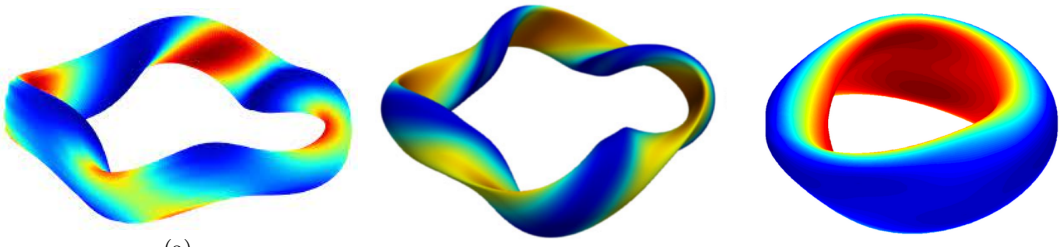

(a) (b) (c)

Figure 1.2: Plots of the magnitude of the magnetic field in optimised stellarators, targeting quasi-isodynamicity (a), quasi-helical symmetry (b) and quasi-axisymmetry (c). Reproduced from [9–11]

one of the ways in which an external rotational transform, ι_{ext} — the contribution to the rotational transform from the external coil currents, which produce the vacuum field — can be generated. An example of such a simple stellarator is shown in Figure 1.1 (b). Early stellarators suffered from enhanced particle and thermal transport out of the device, such that the experimentally observed confinement was worse than in contemporary tokamaks [12]. Designing an optimal non-axisymmetric field for a stellarator, which minimises both the drift motion and collisional transport out of the confined region, is much more challenging than in tokamaks.

Significant efforts have been made to design such optimised configurations, leading to different families of optimised stellarators. The Wendelstein 7-X (W7-X) stellarator is the largest stellarator experiment currently operational. This stellarator was designed to limit collisional transport, approaching the limit of quasi-isodynamicity, where contours of the magnitude of the magnetic field are poloidally closed [2], as shown in Figure 1.2 (a). Other stellarators have been designed to approach the limit of quasi-symmetry [13]. In this limit, the magnetic field is chosen such that its magnitude depends on only two of the three Boozer coordinates [14]. The field is thus in some sense symmetric. This leads to quasi-axisymmetric and quasi-helical stellarators, which have improved confinement properties over classical stellarators. Example quasi-helical and quasi-axisymmetric stellarators are shown in Figure 1.2 (b) and (c).

1.2 Current performance and prospects of tokamaks and stellarators

The development of magnetic confinement devices can be measured through the Lawson criterion or triple product, $n_{\text{i}}T_{\text{i}}\tau_{\text{E}}$, which is the product of the plasma ion density, n_{i}, the plasma ion temperature, T_{i}, and confinement time, τ_{E} [15]. Values of the triple product for different tokamaks and stellarators are shown in Figure 1.3. It can be seen that the highest values of the triple product achieved at the time of writing are from the largest existing tokamak reactors, such as JET and

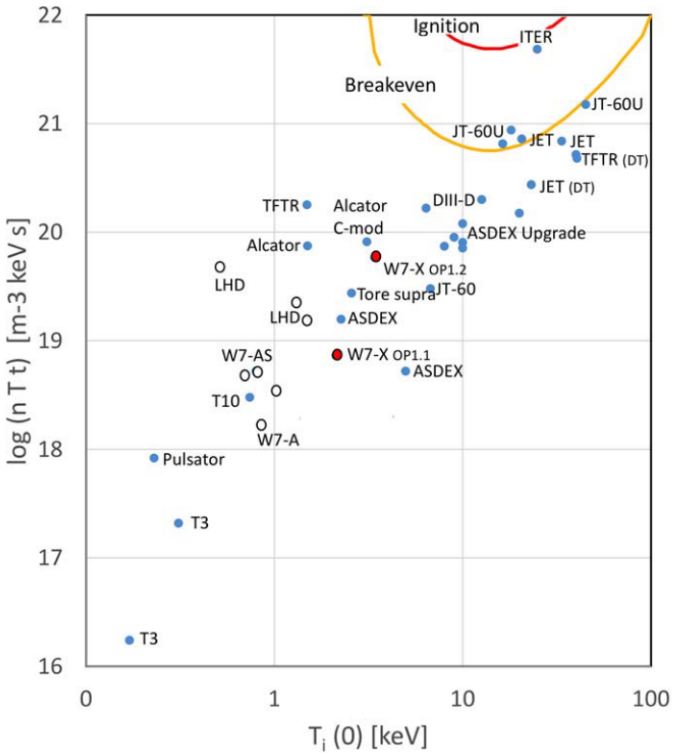

Figure 1.3: Comparison of triple product for stellarators and tokamaks. Reproduced from [16]

JT-60U. The result shown for ITER is a prediction for its $Q = 10$ scenario.

In this sense tokamaks are ahead of stellarators in their development, but they are not without their challenges. The toroidal current that is necessary to confine particles is large, and can drive MHD instabilities — macroscopic perturbations of the desired field structure which can degrade confinement. Although significant efforts have been made to avoid, or control these instabilities, tokamaks are still susceptible to disruptive instabilities — a chain of events that leads to a total loss of the plasma discharge [4]. Disruptions are highly nonlinear processes, such that there is no one root cause to the loss of MHD stability. As such events expel a large fraction of the thermal energy of the plasma onto the reactor vessel, damaging components of the wall structures, they cannot be tolerated in an energy producing reactor concept. This demanding constraint is currently one of the central challenges for the tokamak community.

Tokamaks have developed faster than stellarators and became the main reactor concept for magnetic confinement, because of the increased complexity of non-axisymmetric configurations. However with time, advanced stellarators have been designed which can overcome the major transport losses that prevented early stellarators from advancing. It can be seen that in recent years, advanced stellarators such as W7-X are reaching far higher values of the Lawson's criterion that

have begun to be comparable to modern tokamaks. The next operational phase of W7-X aims to exceed a triple product of 10^{20} m^{-3}keVs [16]. In addition, significant advancements have been made in recent years regarding the optimisation of quasi-axisymmetric stellarators [17]. Although these configurations are a generation behind quasi-isodynamic stellarators, they offer a promising, compact alternative stellarator concept.

As MHD stability becomes a limitation in the development of viable tokamak reactors, stellarators have received increased attention as an alternative path to a fusion reactor. Nowadays, stellarators are typically designed to minimise their toroidal plasma current so as to prevent MHD stability thresholds from being overcome. In such a way, the *magnetic cage* confining the plasma does not depend on the plasma state itself. Modern stellarators that have been developed using this strategy have shown far more robustness against the typical failure mechanisms observed in tokamaks. However, constructing the helical field coils used in such machines is a challenging engineering task.

As an alternative, stellarators can be designed which use both plasma current, and an externally imposed helical field, which reduces the complexity of the coil design. In reality, there is a spectrum of magnetic confinement configurations between typical zero net current stellarators and tokamaks. QA stellarators are of particular interest in this regard, because they are known to have a significant bootstrap current — a type of plasma current which occurs naturally in plasmas as a result of collisional processes, such that it does not need to be externally driven [18]. While such hybrid configurations can simplify the design of the external magnetic field coils, by reducing their 3D shaping, they can reintroduce the problems of MHD stability. Despite this limitation, the parameter space of stellarators is far larger than the one of tokamaks [3], and it is likely that more attractive reactor configurations can be found, provided the understanding of 3D configurations continues to develop. The main research questions considered in this thesis aim to progress understanding of the detailed MHD stability properties of current carrying stellarators.

1.3 Macroscopic MHD instabilities of interest in stellarators

In this section, several of the main MHD instabilities that are relevant for stellarators are outlined. The characterisation of MHD instabilities in fusion plasmas is described in detail in Section 2.4.1. For now, the instabilities are qualitatively described, making use of observations from tokamaks where these MHD effects have been analysed more extensively. The current understanding of the instabilities in stellarators are then considered to motivate their further study.

The main MHD instability of interest within this thesis is called the external kink. It will be shown in this section how such modes are relevant in defining the operational limits of QA stellarators, where the toroidal plasma current is significant. The external kink is studied with the objective of understanding how the

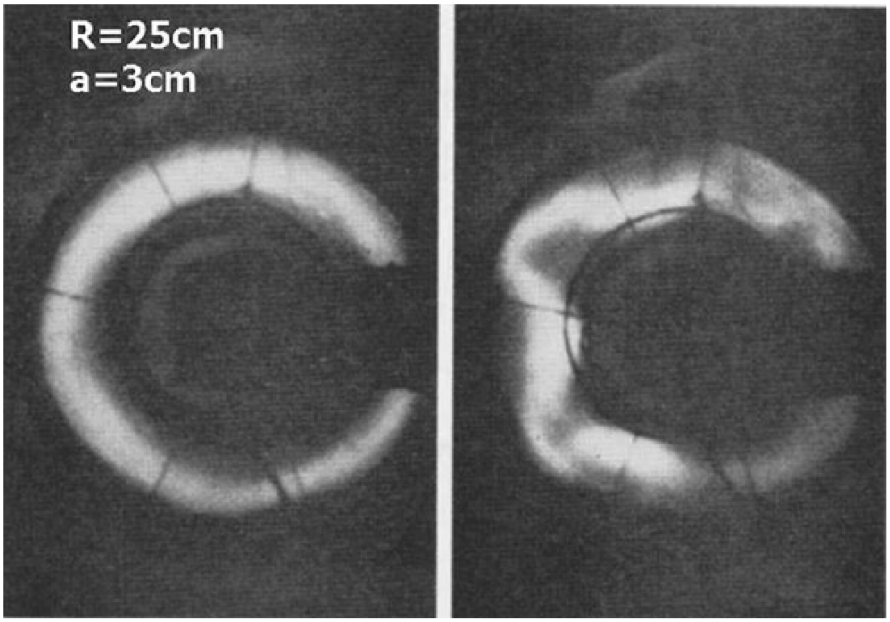

Figure 1.4: A 1950s experimental observation of a kink instability in a Z-pinch at Aldermaston. Reproduced from UK Atomic Energy Authority. Public domain image, by virtue of being published before 1960.

externally generated rotational transform of a stellarator can influence the nonlinear dynamics of the instability.

In addition to external modes, non-ideal tearing modes, and internal kinks are considered as part of validation studies for the numerical tools that have been developed during this thesis. These studies are also contributing to the long term goal of modelling the nonlinear dynamics observed in Wendelstein 7-X, using full non-axisymmetric geometry.

1.3.1 External kinks and the performance limits of quasi-axisymmetric stellarators

The external kink mode is named after the radially kinked flux surfaces that are produced by the instability, as shown in Figure 1.4. This figure shows a kink mode in a Z pinch — an early fusion device, which used a purely toroidal plasma current to achieve confinement. MHD instabilities are generally characterised by the dominant poloidal and toroidal mode numbers, m and n of the perturbation. For example, in Figure 1.4, the dominant poloidal mode number can be identified as $m = 1$. The kink instability is primarily driven by toroidal plasma current, and was one of the main reasons this early proposal failed, because it can be shown to be unconditionally unstable to this mode [12].

For tokamak plasmas, the external kink limits the plasma current, constraining the edge safety factor to be above $q = 2$, in order to avoid the most threatening

global versions of this instability. While the external kink is not a significant threat for low pressure discharges with an Ohmic current profile, this is not the case at finite pressure where some of the instability drive comes from destabilising pressure gradients [19]. As part of the ITER physics basis, external kinks and resistive wall modes — external kinks which are partially stabilised by the presence of a resistive wall — were identified as potentially threatening MHD instabilities for steady state fusion devices [20]. This is because steady state devices typically make use of a large bootstrap current, which leads to broad toroidal plasma current density profiles with steep edge gradients that enhance the external mode. At high pressure, the pressure drive can also become significant in regions of low magnetic shear.

In addition to external kink modes, axisymmetric kinks, called vertical displacement events are a typical feature of disruptions in high performance tokamaks [21]. This is because a significant amount of shaping is necessary to improve the performance of such devices. Poloidal field coils are used to effectively stretch the plasma in the vertical direction, which has the beneficial effect of pushing up the edge safety factor for the same total toroidal plasma current, improving confinement, and extending the operational limits. However, it can be shown that the vertical force this shaping applies on the plasma column is destabilising [19]. The vertical field coils used to stretch the plasma are intrinsically unstable for the tokamak case, as they produce an unfavourable vertical gradient in the magnetic field. If the plasma moves upwards or downwards towards one of the coils, a destabilising force will be reinforced, resulting in an exponential growth of the plasma displacement from its original axis location. Such effects often occur during disruptions, when the plasma temperature begins to drop in the outer region, causing a higher resistivity, and a sharper current profile with lower inductance, such that the stabilising effect of the wall is mitigated. The fast motion of the plasma into the containment vessel can lead to large thermal and mechanical loads that cannot be tolerated in a viable reactor concept.

With respect to stellarators, external kinks pose a similar problem for QA stellarators, as they do for advanced tokamak scenarios. These current carrying configurations have a plasma current that is also generated mainly by bootstrap currents, leading to broad profiles that suffer from the same problems as advanced tokamak scenarios. In the optimisation of previous QA configurations, external kinks were the main instability observed that limited the operational space, even at relatively small toroidal plasma currents, 4 to 6 MA, for a reactor scale device [22, 23]. These studies only considered the stability of the target equilibrium. In addition, during the ramp-up of the bootstrap current profile at the start of a discharge, the finite current could also make it difficult to find a trajectory that avoids MHD instabilities [24]. As such, these instabilities seem to be important in determining potential mechanisms for confinement to degrade in such QA stellarators, and their presence has ruled out many otherwise attractive device candidates. This is because it is unclear when the nonlinear dynamics of the observed external kink modes will lead

to a disruption [11].

Ideal kinks have been studied extensively for tokamak geometries, and play an important role in defining their performance limits [25]. Early work modeling vacuum Kadomstev bubbles has shown that the deformation of the plasma is largest for low (m, n) pairs [26, 27]. The saturation of the external mode alone leads to a significant degradation in confinement, but can also trigger further MHD activity [28]. Past studies have shown how internal ideal kink instabilities can lead to disruptions, by driving locked tearing modes in the plasma core [29]. Even after the inclusion of a resistive wall to stabilise ideal kinks, resistive wall modes remain an important instability that needs to be controlled in tokamak devices, by plasma rotation or active magnetic feedback.

Compared to tokamaks, external kinks in stellarators have not been studied so extensively. Most existing analysis has only considered the linear stability of such modes. In the design of the National Compact Stellarator Experiment (NCSX), it has been shown that the pressure drive for finite pressure kink modes can be stabilised by the external magnetic field through toroidally localised magnetic shear [22]. It is still unclear how the nonlinear dynamics of such instabilities evolve, however. There are two physics questions of interest for QA stellarators. In proposed QA devices where external kinks are predicted to threaten performance, can they lead to disruptive instabilites? If they saturate, how significant is the degradation of confinement?

It should also be noted that equivalent instabilities to vertical displacement events can occur in stellarator plasmas, if the helical field coils are used to shape the plasma, in addition to providing the external rotational transform. A simple axisymmetric criterion for such $n = 0$ positional stability has been developed for plasmas with a flat current profile, and validated against numerical models [30]. This approximation has been compared against experiments on the Compact Toroidal Hybrid device, with reasonable agreement between the experimental and theoretical stability boundary found by the axisymmetric criterion [31]. As such it is relatively clear when vertical modes will be stabilised. In the stellarator case, once the vertical mode is shown to be linearly stable, it is not clear what nonlinear perturbation to apply in order to make it unstable. The amount of external rotational transform required to stabilise this mode is typically relatively small, such that it does not significantly limit the operational space of stellarators to enforce that they are vertically stable. For this reason, vertical stability is not considered in detail in this thesis.

1.3.2 Resistive and non-ideal instabilities observed in Wendelstein stellarators

The resistive analogue to the ideal kink mode is the current driven tearing mode, so called because of how the instability tears the magnetic field topology. While ideal instabilities deform the magnetic field structure, preserving nested flux surfaces wherever they exist, resistive modes can modify the topology, ripping the

surfaces apart. Poincaré plots can be used to assess the magnetic field structure, and illustrate this difference. Field lines are traced around the torus, plotting their intersection points with a particular poloidal plane, as shown in Figure 1.5 (a), which shows a simple tokamak equilibrium. As discussed in Section 1.1, the nested toroidal flux surfaces in this equilibrium lead to good confinement properties by minimising parallel thermal transport along field lines.

Using an appropriate radial coordinate, such as the normalised poloidal flux, $\hat{\Psi}$, discussed in more detail in Section 2.3, the magnetic topology can be shown more clearly. Figure 1.5 (b-c) show examples of ideal and resistive nonlinear perturbations of a tokamak equilibrium. The ideal instability has kinked the flux surfaces such that the lines traced by the magnetic field in Figure 1.5 (b) are no longer vertical, with constant $\hat{\Psi}$, as they would be in the unperturbed equilibrium. On the other hand, the resistive dynamics in Figure 1.5 (c) have torn the initial flux surfaces apart, leading to magnetic islands — a region of the magnetic topology, which forms closed magnetic flux surfaces and is partitioned from the rest of the field structure by a separatrix. In such a way, resistive instabilities modify the magnetic topology of the domain, such that two separate regions form, which are divided by a magnetic island chain.

Tearing modes occur when the ideal kink mode is stable, over longer timescales where resistive diffusion can dominate. Similar to the external kink, it is possible for tearing modes to lead to disruptions in tokamaks [19]. Low order rational surfaces can become tearing mode unstable during a discharge, leading to large islands forming across the plasma region. Island structures create shortcuts in the poloidal direction, such that thermal energy can be transported radially through parallel transport. This leads to a reduction in the temperature, which increases the resistivity, exacerbating the instability further. If secondary magnetic islands are triggered by this process, and overlap, ergodic regions can form, as shown in Figure 1.5 (d). These stochastic regions can degrade confinement to the point where a significant amount of thermal energy is lost. At this point, the total plasma current will typically spike as a result of current redistribution, before also collapsing such that confinement is completely lost, terminating the discharge.

In the classical stellarator Wendelstein 7-A (W7-A), similar tearing mode driven disruptions were observed [32]. These disruptions could be avoided in the device, once a sufficient external rotational transform was applied to the experiment. It was argued that the mechanism for stabilising the mode was the flattening of the q profile, which shifts the unstable region of the plasma out towards the plasma boundary. Linear analysis of the tearing mode stability showed that this effect reduces the growth rate, as a result of the combination of smaller current density gradients in the plasma periphery, and the influence of the conducting wall outside the plasma, which helps to stabilise the mode. This stabilisation mechanism will be shown explicitly in the linear analysis in Chapter 7.

Classical stellarators are much simpler than the advanced stellarators that are the focus of the fusion community currently. Subsequently, experimental campaigns

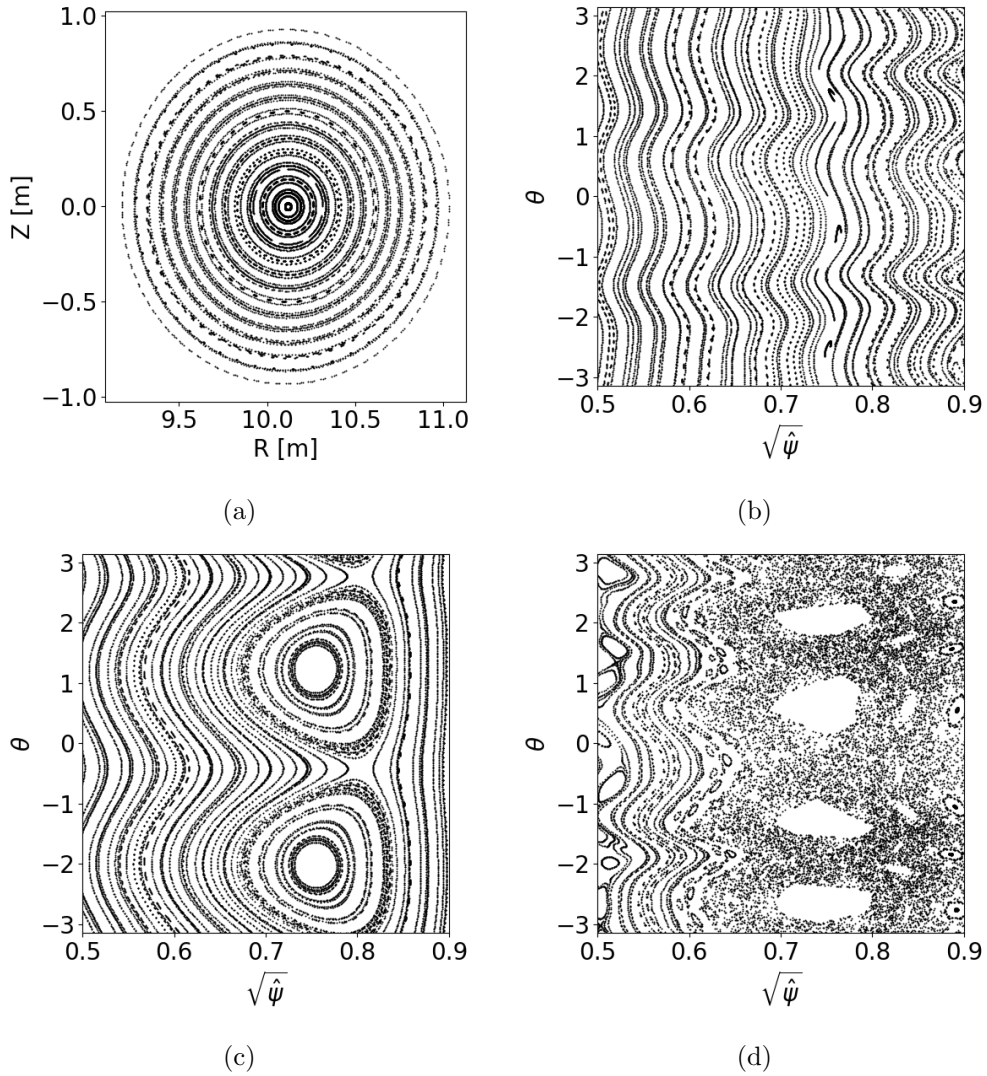

Figure 1.5: Poincaré plots of a tokamak equilibrium (a), compared with ideal (b) and resistive (c) MHD perturbations, which modify the initially nested flux surfaces by kinking or tearing them, respectively. The magnetic topology has changed in the resistive perturbation, such that the original nested flux surfaces are divided into two regions, separated by a magnetic island chain. An example of an ergodic field produced by overlapping islands (d) is also shown. Note that the Poincaré plots are not generated from the same tokamak.

have been attempted on W7-AS to inform the MHD stability of advanced devices. W7-AS was designed in such a way as to minimise the toroidal plasma current. When operated in this way, it was shown that the device had generally benign MHD activity. In general, the reversed shear profiles of stellarators are expected to be benign compared to those of tokamaks, because neoclassical tearing modes

— tearing modes which are reinforced by the perturbed bootstrap current — are expected to be stabilised in these configurations [2]. Several experimental campaigns were carried out to intentionally increase the plasma current, in order to understand the MHD activity this induces. Similar resistively driven disruptions were observed in these campaigns as have been observed in W7-A [33]. The results were not able to inform the design of QA stellarators conclusively, as similar large bootstrap current profiles were not achievable in W7-AS [34].

More recently, an experimental campaign was carried out on the Wendelstein 7-X (W7-X) stellarator, where a modest amount of Electron Cyclotron Current Drive (ECCD) induced plasma current, on the order of kiloamps, was used to destabilise modes at low order rational surfaces within the plasma. The induced plasma current was shown to lead to oscillations in the core plasma temperature, similar in form to sawteeth instabilities in tokamaks, and, in the worst case, plasma terminating events [35]. The ECCD currents modify the q profile of the device in the plasma core, introducing multiple $q = 1$ rational surfaces. MHD activity around these surfaces is one potential cause for the observed periodic relaxations and plasma terminations. These plasma terminating events are currently one of the central research concerns for MHD activity in W7-X.

1.4 Computational methods in MHD analysis

Nonlinear MHD models are a valuable tool in helping to answer the research questions posed regarding the stability limits of stellarators. The highest fidelity model would be to actually solve the *initial value problem* for a magnetic confinement system, meaning that the physical system of equations governing the dynamics are evolved in time. At the time this thesis began, only a few nonlinear codes could be applied to solve initial value problems in stellarator geometry, such as MEGA [36] and FLUXO [37]. The main workhorse codes used by US research communities, M3D-C^1 [38] and NIMROD [39], which were originally designed to model tokamaks, had begun the process of being extended to model strongly shaped non-axisymmetric devices, but were not yet ready for extensive nonlinear MHD studies of optimised stellarators. M3D-C^1 has recently been extended such that it can be used to model optimised stellarators [40].

The main code used throughout this thesis is the nonlinear code JOREK [41, 42]. JOREK is a fully implicit, 3D, nonlinear extended MHD and kinetics code, capable of being run with reduced and full MHD models of varying complexity. In cylindrical coordinates, the poloidal planes are discretised using bi-cubic G^1 Bezier finite elements, with a real Fourier series in the toroidal direction [43]. The option for higher order continuity in the finite element basis has recently been added to the code [44]. The numerical details of the code will be described in more detail in Chapter 2.

JOREK was originally written to model tokamaks. In parallel to the main developments of this thesis work, which is based around the tokamak version of the

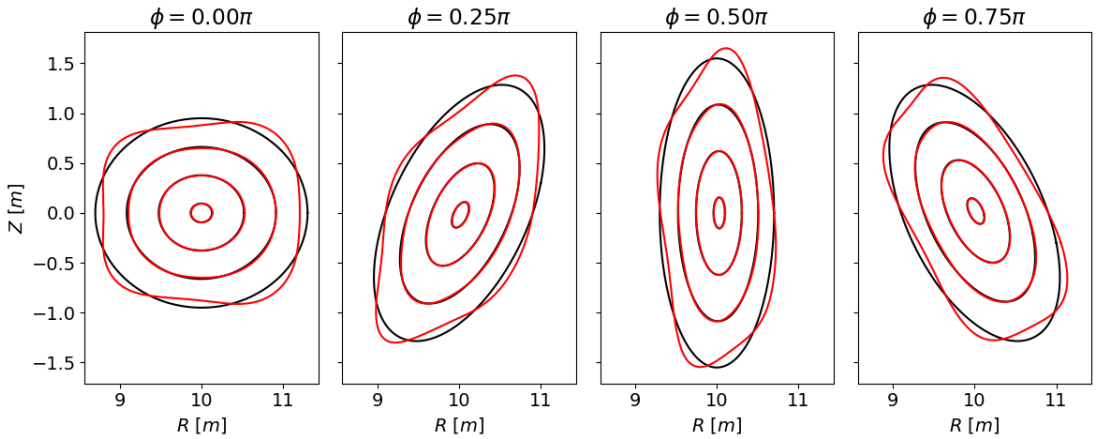

Figure 1.6: Poloidal cuts at different toroidal angles, ϕ, of an example computation of a saturated $m = 4$, $n = 1$ external kink instability (red) in a $l = 2$ classical stellarator using an equilibrium approach. The perturbed equilibrium is compared with the initial state (black). Note that the poloidal cross section of the $l = 2$ stellarator varies toroidally because the axisymmetric plasma cross section is elongated.

code, this PhD project also contributed towards the extension of JOREK to model stellarators in full non-axisymmetric geometry. A hierarchy of stellarator capable models of varying complexity were derived as part of a separate thesis project [45, 46], and validated in JOREK for linear resistive MHD instabilities in a classical stellarator [47–49]. In principle, this extension can be used to model optimised stellarators, where the linear MHD dynamics begins to deviate qualitatively from tokamaks, however the code has yet to be validated for and applied to these more complicated equilibria.

Assessments of the nonlinear dynamics of global current driven instabilities requires an evolution of the full magnetic field in time. For advanced stellarators, where an accurate description of the magnetic field requires many toroidal harmonics, simulations are expected to be computationally demanding. As such, it follows to consider supplementing the high fidelity approaches being developed in nonlinear codes with simplified simulations of the nonlinear dynamics of stellarators.

Two simplified modelling approaches were considered in this thesis project. The first is to use ideal MHD equilibrium codes to model saturated MHD instabilities in stellarators. As outlined in Section 2.3, equilibrium codes solve for a stationary plasma configuration, which is in force balance. These methods can therefore not resolve the time evolution of an instability. However, in Section 2.3.1, past work that has used equilibrium codes to resolve the final, saturated state of an instability is reviewed. An example of such a nonlinear study is shown in Figure 1.6. In this figure, the initial shape of a two field period, $l = 2$ stellarator is shown in black, overlaid with a perturbed ideal MHD state which corresponds to the $m = 4$, $n = 1$

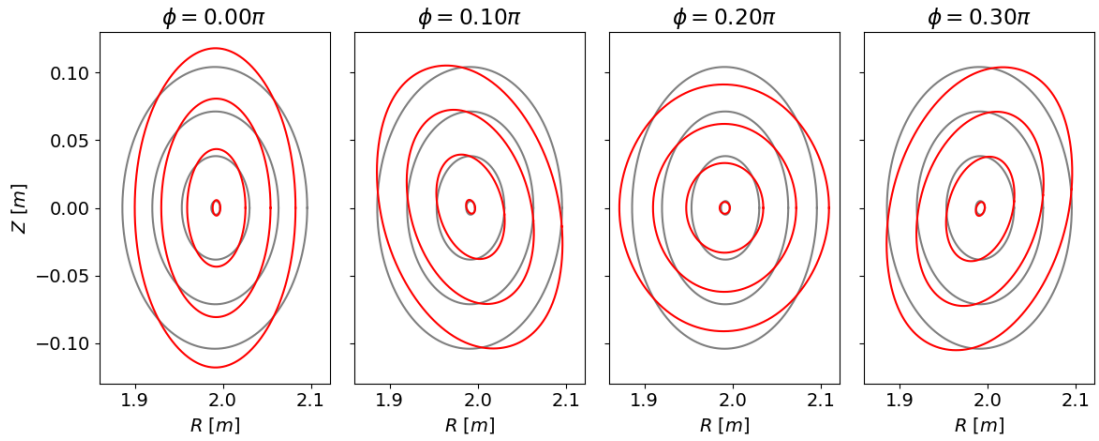

Figure 1.7: Poloidal cuts at different toroidal angles, ϕ, of the equilibrium flux surfaces of the classical stellarator Wendelstein 7-A (red) and its axisymmetric approximation (grey).

deformation produced by an external kink instability. The final saturated state of an instability can be characterised, helping to give a general impression of the nonlinear dynamics, based on the size and structure of the perturbation that is introduced.

This equilibrium approach is of interest to the research community because, although it is an ideal MHD approach that can only be used to model the final state of an instability, it is a free boundary, full MHD equilibrium model, meaning that it makes no approximations about the structure of the magnetic field, and can be used to model free boundary external modes, such as external kinks. The main 3D stellarator capable model implemented in JOREK is currently a fixed boundary reduced model. This means that the system of equations that need to be solved are simplified by neglecting parts of the description that are considered to not be important in the dynamics, and that free boundary external modes cannot be simulated, due to the ideal wall boundary condition. As a result, the equilibrium approach could offer a computationally efficient approach to exploring full MHD free boundary dynamics that would not be possible in the short term using JOREK's stellarator model.

The second approach is to modify configurations such that they can be modeled axisymmetrically, as outlined in Section 2.6. Historically, this approach is known as the stellarator expansion [50], but is referred to in the JOREK community as the virtual current model, because the model is implemented using an artificial toroidal current, rather than an externally imposed field. The approach allows for the physical effects of a loosely wound, external helical field to be included in nonlinear MHD models using an axisymmetric geometry. An example of the flux surfaces of such an approximation of a classical stellarator is shown in Figure 1.7. The figure shows the classical stellarator, Wendelstein 7-A, and an axisymmetric

domain, which is used in JOREK to model the stellarator approximately. While unable to capture features of strongly shaped optimised stellarators, the approach can provide a first order understanding of how an external helical field influences the MHD dynamics. This method is used to provide an initial understanding of the nonlinear dynamics in optimised stellarators, before the stellarator capable model is used to study the dynamics in detail.

1.5 Outline of the thesis

The remainder of this thesis is organised as follows. In Chapter 2, the background regarding the physics concepts and numerical methods used herein will be provided. Chapters 3 and 4 are devoted to the use of the VMEC code to model nonlinearly saturated MHD states in tokamaks and stellarators. The method is validated, comparing previous results generated for tokamak equilibria with JOREK simulations, and then applied to model external kinks in classical stellarators. The virtual current model is then validated in Chapter 5, verifying the implementation against linear ideal and resistive MHD stability problems. In Chapter 6 the virtual current model is used to study the nonlinear MHD dynamics of a QAS device that is unstable to external kink modes, showing the influence that an externally applied helical field can have on such an instability. Finally, in Chapter 7, contributions towards the development of fully non-axisymmetric simulations of stellarators are discussed. Conclusions and future work are summarised in Chapter 8.

2 Magnetohydrodynamics and Numerical Modelling

In this section, an outline of magnetohydrodynamics in the context of plasma theory is given, as well as an introduction to the main numerical methods and codes that have been used in this thesis. The derivation of the MHD equations from the Boltzmann equation, and their value in the context of numerical modelling, is explained in Section 2.1. In Section 2.2, the different coordinate systems used in magnetic confinement modelling are discussed. The importance of MHD equilibria is then outlined in Section 2.3, as well as numerical approaches to calculating them in axisymmetric and non-axisymmetric systems using the VMEC code. The application of such codes to model nonlinearly saturated MHD instabilities is then reviewed. The linear stability of such MHD equilibria to macroscopic instabilities is considered using perturbation theory in Section 2.4, introducing a numerical approach to solving such problems using the CASTOR3D code. In Section 2.5, the limitations of linear analysis motivate a discussion of nonlinear MHD dynamics and solutions to the initial value problem, using the numerical approach in the JOREK code. The implementation of an axisymmetric approximation of stellarators within the JOREK code is finally outlined in Section 2.6.

2.1 Context of magnetohydrodynamics

2.1.1 Plasma physics and the value of the fluid description

The modelling work performed in this thesis requires a description of a *magnetised plasma* which is tractable for long timescale simulations on the order of milliseconds. A plasma is an ionised gas that exhibits collective behaviour through a response to external and self-generated electric and magnetic fields. A magnetised plasma is a plasma which is embedded in a strong magnetic guide field, such that the parallel and perpendicular dynamics can be distinguished.

Plasma dynamics spreads over a wide range of length and time scales depending on the properties of the system being studied. For fusion plasmas, the timescales can range from the electron gyroperiod, on the order of a picosecond for a 1 T magnetic field, to the resistive diffusion time, on the order of milliseconds at 10 keV fusion relevant temperatures. Length scales vary from the electron gyroradius, on the order of 10^{-5} m, to the ion mean free path, on the order of 10^{3} m. One of the central problems in modelling plasmas is finding an appropriate means of reconciling these vastly different spatial and temporal scales.

The timescale relevant for the macroscopic instabilities in the toroidally confined plasmas considered here lies in the range of microseconds to milliseconds. To resolve this timescale, a fluid, or magnetohydrodynamic description of the plasma can be derived. In this section, the derivation of the MHD equations will be outlined, following loosely the derivations in [12, 51]. To begin with, in Section 2.1.2, the MHD equations are derived by applying a series of approximations on the more general Boltzmann equation.

2.1.2 Derivation of the MHD equations

The Boltzmann equation provides a generalised governing equation for plasma dynamics, using a distribution function $f_\alpha(t, \mathbf{x}, \mathbf{v})$ for the particles of each species, α, in a given system. $\mathbf{x}$ and $\mathbf{v}$ are independent variables defining position and velocity space.

$$\frac{\partial f_\alpha}{\partial t} + \mathbf{v} \cdot \nabla_{\mathrm{x}} f_\alpha + \frac{\mathbf{F}}{m_\alpha} \cdot \nabla_{\mathrm{v}} f_\alpha = \left(\frac{\partial f_\alpha}{\partial t} \right)_{\mathrm{coll}} . \tag{2.1}$$

For a typical plasma in the absence of gravitational forces, $\mathbf{F} = eZ_\alpha \left(\mathbf{v} \times \mathbf{B} + \mathbf{E} \right)$, where $\mathbf{B}$ is the magnetic field, and $\mathbf{E}$ is the electric field. The right hand side operator corresponds to changes in the distribution function as a result of particle collisions. The evolution of this equation provides a general description of plasma dynamics, however it captures an unnecessary amount of detail for the problems of interest herein, such that the equation becomes too expensive to solve numerically. As a result, within the context of macroscopic dynamics, the equation is normally simplified under a series of assumptions, leading to the *fluid description* of a magnetised plasma. By neglecting certain microphysical aspects, the fluid, or magnetohydrodynamic, description of a plasma provides a computationally tractable approach to modelling a plasma globally, and understanding its macroscopic stability.

First, the fluid moments of the Boltzmann equation need to be taken for each particle species. As shown in [52], this leads to the system of equations below

$$\begin{aligned}
\frac{\partial n_\alpha}{\partial t} + \nabla \cdot \left(n_\alpha \mathbf{u}_\alpha \right) &= 0, \\
m_\alpha n_\alpha \left(\frac{d\mathbf{u}_\alpha}{dt} \right) - Z_\alpha e n_\alpha \left(\mathbf{E} + \mathbf{u}_\alpha \times \mathbf{B} \right) + \nabla \cdot \mathbf{P}_\alpha &= \mathbf{R}_\alpha, \\
\frac{3}{2} n_\alpha \left(\frac{dT}{dt} \right) + \mathbf{P}_\alpha : \nabla \mathbf{u}_\alpha + \nabla \cdot \mathbf{q}_\alpha &= Q_\alpha, \\
\nabla \times \mathbf{B} &= \mu_0 e \left(n_{\mathrm{i}} \mathbf{u}_{\mathrm{i}} - n_{\mathrm{e}} \mathbf{u}_{\mathrm{e}} \right) + \frac{1}{c^2} \frac{\partial \mathbf{E}}{\partial t}, \\
\nabla \cdot \mathbf{E} &= \frac{e}{\epsilon_0} \left(n_{\mathrm{i}} - n_{\mathrm{e}} \right), \\
\nabla \cdot \mathbf{B} &= 0
\end{aligned} \tag{2.2}$$

where the three lowest order moments of the distribution function - the particle number density, fluid momentum and pressure tensor - are given by

$$\begin{aligned} n_\alpha &= \int f_\alpha d\mathbf{v}, \\ n_\alpha \mathbf{u}_\alpha &= \int \mathbf{v} f_\alpha d\mathbf{v}, \\ P_\alpha &= \int m_\alpha f_\alpha \left(\mathbf{v}-\mathbf{u}_\alpha\right) \otimes \left(\mathbf{v}-\mathbf{u}_\alpha\right) d\mathbf{v} \end{aligned} \tag{2.3}$$

$\mathbf{R}_\alpha$ in the momentum equation refers to the friction force produced by the collisional operator. Q_α and $\mathbf{q}_\alpha$ are the heat source and flux, respectively. It can be seen that the evolution of the magnetic and electric fields follows Maxwell's equations. When only two species for electrons and ions are assumed, this model is called the two fluid model. Typically, in fusion plasmas, the two fluid model is a reasonable assumption, as other species have such low relative densities that they can often be included as perturbations to the two fluid model, instead of being modelled explicitly as a third species in the system of interest. This model is still exact, as long as the integrals for the fluid moments, n_α, $\mathbf{u}_\alpha$, $\mathbf{R}_\alpha$, $\mathbf{q}_\alpha$ and Q_α are carried out explicitly.

In order to obtain a system that is more amenable to analysis, more assumptions need to be made. First, the high frequency content of the system is eliminated. This can be done by assuming that electron inertia is negligible, such that the response of the electrons to the dynamics of interest is effectively instantaneous, and that ϵ_0 is set to zero. This eliminates high frequency electromagnetic waves, which would otherwise stiffen the system of equations. With these assumptions, the two fluid model can be simplified further, obtaining a single fluid model.

The elimination of electron inertia leads to the derivation of Ohm's law from the electron momentum equation. If the electron inertia can be neglected, the momentum equation for the electrons simplifies to

$$\mathbf{E}+\mathbf{v}\times\mathbf{B} = \frac{1}{n_\mathrm{e} e}\left[\mathbf{J}\times\mathbf{B} - \nabla p_\mathrm{e} - \nabla\cdot\mathbf{\Pi}_\mathrm{e} - \mathbf{R}_\mathrm{e}\right]. \tag{2.4}$$

If the terms on the right hand side are neglected, the ideal Ohm's law is recovered. Typically the first effect to be included is the resistive friction term $\mathbf{R}_\mathrm{e}/n_\mathrm{e}e \approx \eta\mathbf{J}$, leading to the resistive Ohm's law. The other terms, corresponding to the Hall effect, diamagnetic drift and electron viscosity, respectively, are included depending on the physical system of interest. In particular for fusion plasmas, the diamagnetic term can become important.

The final step is to eliminate the higher order moments that are found in the single fluid equations by applying a closure relation, which can be used to write these terms as functions of the lower moments. The type of closure, and the ordering

assumptions used to eliminate terms define the complexity of the MHD equations that are obtained. The single fluid viscoresistive MHD equations can be derived as

$$\begin{aligned}
\frac{\partial \rho}{\partial t} + \nabla \cdot (\rho \mathbf{v}) &= S_\rho + \nabla \cdot \left(D_\perp \nabla_\perp \rho + D_\parallel \nabla_\parallel \rho \right), \\
\rho \frac{d\mathbf{v}}{dt} &= \mathbf{J} \times \mathbf{B} - \nabla p - \nabla \cdot \bar{\mathbf{\Pi}}, \\
\frac{d}{dt}\left(\frac{p}{\rho^\gamma} \right) &= S_\mathrm{e} + \nabla \cdot \left(\kappa_\perp \nabla_\perp T + \kappa_\parallel \nabla_\parallel T \right), \\
\mathbf{E} &= \eta \mathbf{J} + \mathbf{v} \times \mathbf{B}, \\
\nabla \times \mathbf{E} &= \frac{\partial \mathbf{B}}{\partial t}, \\
\nabla \times \mathbf{B} &= \mu_0 \mathbf{J}, \\
\nabla \cdot \mathbf{B} &= 0
\end{aligned} \tag{2.5}$$

The viscous term in the above set of equations corresponds to $\nabla \cdot \bar{\mathbf{\Pi}}$ and the resistive term is $\eta \mathbf{J}$. If these terms are removed, the ideal MHD equations are obtained.

Physical processes that occur on faster timescales than MHD processes are termed microphysical processes. These effects are important for defining several terms in the above equations. S_ρ and S_e refer to such coupling terms between microphysical models and the MHD equations, defining the external particle and heat sources, respectively. Rigorously, these terms, in addition to the diffusion operators, D and κ, would be defined from models of the microphysics in the particular system of interest. Because these numerical models are too computationally expensive to run over the MHD timescale, the coefficients for sources and diffusion coefficients are typically prescribed on an ad-hoc basis.

2.2 Coordinate systems

Before turning to the problems that the system of equations 2.5 can be applied to, it is important to understand the different coordinate systems that are available to model these problems. Intuitively, it might be thought that the analysis of a toroidal geometry is most suited to the cylindrical coordinate system, (R, Z, ϕ), as shown in Figure 2.1. This simple orthogonal coordinate system is conventionally much more amenable to analysis. For a righthand coordinate system, where the toroidal angle, ϕ, increases clockwise around the Z axis, the relationship between Cartesian and cylindrical coordinates is given by

$$\mathbf{x} = \begin{pmatrix} \mathrm{R}\,\cos(\phi) \\ -\mathrm{R}\,\sin(\phi) \\ \mathrm{Z} \end{pmatrix} \tag{2.6}$$

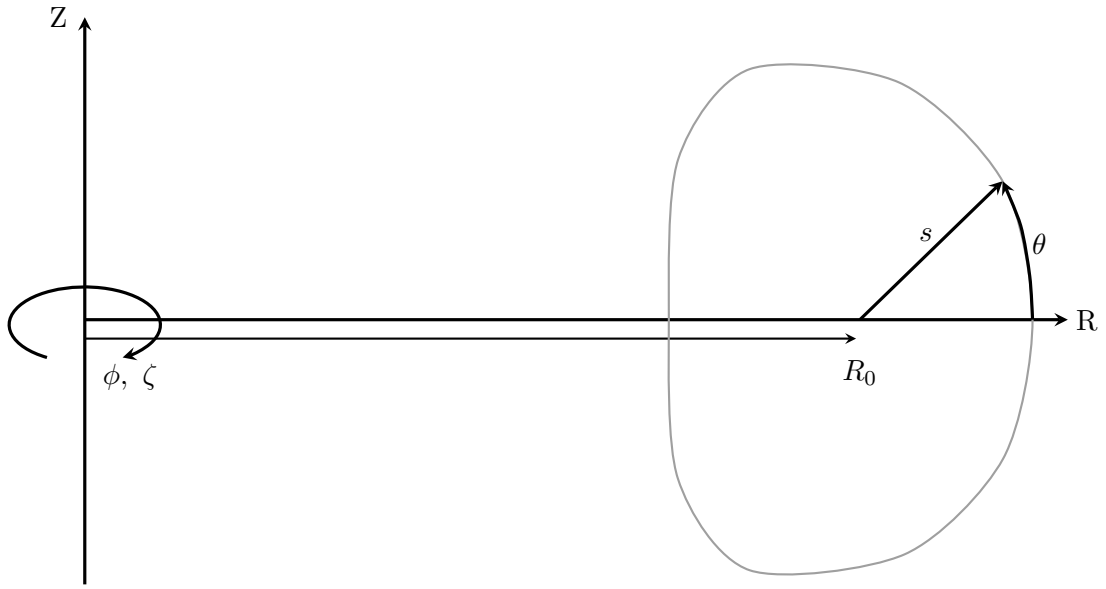

Figure 2.1: Sketch of coordinate systems used in magnetic confinement theory. The major radius R, vertical position, Z, and toroidal angle, ϕ make up the righthanded toroidal coordinate system. The gray line sketches a typical flux surface, s, which together with the poloidal coordinate, θ, and toroidal angle, ζ, make up a flux surface coordinate system.

such that the covariant basis vectors are given by

$$\mathbf{e}_{\mathrm{R}} = \begin{pmatrix} \cos(\phi) \\ -\sin(\phi) \\ 0 \end{pmatrix} \qquad \mathbf{e}_{\phi} = \begin{pmatrix} -\mathrm{R}\sin(\phi) \\ -\mathrm{R}\cos(\phi) \\ 0 \end{pmatrix} \qquad \mathbf{e}_{\mathrm{Z}} = \begin{pmatrix} 0 \\ 0 \\ 1 \end{pmatrix} \tag{2.7}$$

While such coordinate systems are often used in magnetic confinement theory, they do not make use of any knowledge about the particular toroidal system of interest that may simplify analysis further. A particularly important observation is that the good magnetic confinement systems that we build towards comprise of a series of nested toroidal flux surfaces, as shown in Figure 1.5 (a), or at least approach this limit. This leads naturally onto the concept of a generalised flux surface coordinate system (s, θ, ζ), as shown in Figure 2.1. In these typically non-orthogonal coordinate systems, s is a radial coordinate which denotes a particular flux surface in the system of interest. θ and ζ are poloidal and toroidal angular coordinates respectively, that need not be related directly to their corresponding geometric angles. Generalised flux surface coordinate systems can simplify the analysis of certain problems, as some physical quantities are constant on flux surfaces. The plasma pressure for example can be written as $p(s)$, rather than as a function of R, Z and ϕ. Typically, the square root of the normalised toroidal flux, Φ — a measure of the magnetic flux through a region inside a given flux surface of the

plasma — is used to define s, as this term is approximately linearly proportional to the plasma radius. However, the poloidal flux, Ψ — a measure of the magnetic flux through the circular area extending from $R = 0$ to a given radius in the $Z = 0$ plane — is also commonly used in the tokamak community.

Lastly, in certain problems it is beneficial to make use of straight field line (SFL) coordinate systems. SFL coordinate systems are a particular type of generalised flux coordinate system, designed in such a way that the magnetic field traces straight lines in the $\theta - \zeta$ plane. Two commonly used SFL coordinate systems are PEST and Boozer coordinates. In PEST coordinates, the geometric toroidal angle, ϕ, is used for the toroidal coordinate, ζ. The poloidal angle, θ^*, is then constructed in such a way that the field lines are straight in the $\theta^* - \phi$ plane. Boozer coordinates are defined in such a way as to eliminate some of the variables used in the representation of a magnetic field in general flux surface coordinate systems [14]. The transformation leads to non-trivial poloidal and toroidal coordinates. In the context of this thesis, straight field line coordinates are especially useful for characterising linear MHD instabilities, as the structure of the instability is often simplified by the transformation to SFL coordinate systems when compared with generalised flux surface coordinate systems. As described in the next section, the equilibrium code, VMEC, uses both a generalised and straight field line coordinate system to solve the ideal MHD equilibrium problem.

2.3 MHD equilibra and the VMEC code

Now that the main coordinate systems have been outlined, they can be applied to the MHD problems of interest. To begin with, stationary solutions to the MHD equations - MHD equilibria - are considered. An MHD equilibrium is a state in which the force operator of the MHD equations is set to zero, such that the system of interest is in some sense stationary. Strictly speaking, an equilibrium does not necessarily mean that there are no flows, or transport in the system of interest. A real equilibrium needs to be driven by heat and particle sources which are in turn constantly also leaking out of the device. In toroidally confined systems, there may also be flows along flux surfaces that do not lead to transport, but may change the equilibrium force balance. These flows of particles and energy, as well as viscoresistive dissipation, are typically small enough to be ignored in the equilibrium description. The remaining ideal MHD equilibrium equation is then given by

$$\mathbf{J} \times \mathbf{B} = \nabla p, \tag{2.8}$$

which is determined from the viscoresistive momentum equation in 2.5, eliminating viscoresistive terms, and assuming that $\mathbf{v}$ and time derivatives are zero. This approximation is often used in the fusion community to describe magnetically confined plasmas.

Equation 2.8 cannot be solved analytically in arbitrary 3D geometry, and requires some assumptions regarding either the geometry, or the imposed magnetic field in order to make progress. If axisymmetry is assumed, it can be shown, as in [12], that equation 2.8 can be simplified to an equation for the poloidal flux, Ψ, called the Grad-Shafranov equation

$$\Delta^* \Psi = -\mu_0 R^2 p'(s) - FF'(s), \tag{2.9}$$

where the Δ^* operator is defined in cylindrical coordinates by

$$\Delta^* \Psi = R^2 \nabla \cdot \left(\frac{\nabla \Psi}{R^2} \right) = R \frac{\partial}{\partial R} \left(\frac{1}{R} \frac{\partial \Psi}{\partial R} \right) + \frac{\partial^2 \Psi}{\partial Z^2}. \tag{2.10}$$

The two equilibrium functions for the pressure and the function FF' are functions of the radial coordinate in flux surface coordinates. These profiles are normally given as inputs to the Grad Shafranov solver. The righthand side is dependent on Ψ, because it is a flux surface quantity, and so can be used to define $s = \hat{\Psi} = (\Psi - \Psi_{\text{axis}}) / (\Psi_{\text{bnd}} - \Psi_{\text{axis}})$, where Ψ_{axis} and Ψ_{bnd} refer to the value of Ψ at the plasma axis, and plasma edge, respectively. Even with this simplification, the solution for Ψ, can only be solved analytically for simple Soloviev equilibria, where the dependence of the righthand side on Ψ is eliminated, or using an ordering approach [12]. Otherwise, Ψ has to be solved for numerically.

To consider 3D stellarator configurations, a numerical approach is required from the outset. The main code used for this purpose is the Variational Moments Equilibrium Code (VMEC) [53]. This equilibrium approach solves equation 2.8, assuming an ansatz for the vector potential, $\mathbf{A}$, given by

$$\mathbf{A} = \Phi(s) \nabla \theta^* + \Psi(s) \nabla \zeta, \tag{2.11}$$

where Φ is the toroidal flux, ζ is the toroidal angle, and $\theta^* = \theta + \lambda(s, \theta, \zeta)$ is the straight field line angle using PEST coordinates. λ is a transform from the poloidal angle θ used for the representation of $R(s, \theta, \zeta)$ and $Z(s, \theta, \zeta)$ describing a flux surface, and the straight field line angle. These quantities are represented using radial splines, and a Fourier series in the poloidal and toroidal directions

$$\begin{aligned}
R(s, \theta, \zeta) &= \sum R^{\text{C}}_{\text{mn}}(s) \cos(m\theta - nN_{\text{p}}\zeta) + \sum R^{\text{S}}_{\text{mn}}(s) \sin(m\theta - nN_{\text{p}}\zeta), \\
Z(s, \theta, \zeta) &= \sum Z^{\text{C}}_{\text{mn}}(s) \cos(m\theta - nN_{\text{p}}\zeta) + \sum Z^{\text{S}}_{\text{mn}}(s) \sin(m\theta - nN_{\text{p}}\zeta), \\
\lambda(s, \theta, \zeta) &= \sum \lambda^{\text{C}}_{\text{mn}}(s) \cos(m\theta - nN_{\text{p}}\zeta) + \sum \lambda^{\text{S}}_{\text{mn}}(s) \sin(m\theta - nN_{\text{p}}\zeta)
\end{aligned} \tag{2.12}$$

The use of a separate poloidal angle, θ, for the description of the flux surfaces, rather than using θ^*, is useful as it allows the spectral representation of R and Z to be condensed by choosing θ carefully [54]. m and n are integer values corresponding

to the poloidal and toroidal mode number of the Fourier series respectively, and N_p is an integer used to define the field periodicity of the device. Normally, the representation is simplified so that R is purely cosinusoidal, and Z, and λ are sinusoidal, such that the device represented is up-down, or stellarator symmetric [55].

The ansatz for the vector potential in equation 2.11, assumes closed, nested magnetic flux surfaces, simplifying the computation. In order to actually find the MHD equilibrium, the potential energy

$$W_\mathrm{mag} = \int \left(\frac{p}{\gamma - 1} + \frac{B^2}{2\mu_0} \right) dV, \tag{2.13}$$

is minimised using a variational approach up to a prescribed tolerance in the MHD force balance $\mathbf{F} = \mathbf{j} \times \mathbf{B} - \nabla p$. The force operator acting on each flux surface is calculated and used to modify the flux surfaces on each iteration. Moving along the path of the MHD force operator should minimise the potential energy, thus reaching an acceptable equilibrium.

There are other approaches to solving the MHD equilibrium equation that are worth mentioning here. A similar approach using an improved numerical representation of the equilibrium has been developed in the Galerkin Variational Equilibrium Code (GVEC) [56]. This code is used later in Chapter 7 to generate equilibria for the stellarator extension of the JOREK code. Another such example is the Stepped Pressure Equilibrium Code [57], which relaxes the assumption of nested flux surfaces by instead solving the Beltrami equation across segments of the plasma volume. This approach has gained increased attention in recent years, but has not been used as part of this thesis, and so is mentioned here only as an aside.

2.3.1 Nonlinear MHD modelling using equilibrium codes

While VMEC is an equilibrium code, it will be used in Chapter 3 and 4 to gain an initial understanding of nonlinear MHD problems. In this section, the equilibrium approach to solving nonlinear MHD problems is outlined by reviewing previous efforts to use equilibrium codes to model perturbed tokamak and stellarator equilibria. Over the past decade, there have been considerable efforts to model nonlinearly perturbed tokamak equilibria modified by resonant magnetic perturbations (RMPs), using VMEC [58, 59]. Such a perturbed configuration can for instance be attractive for preventing the onset of large edge localised modes (ELMs), while maintaining good confinement across the edge region. While initial studies on the DIII-D tokamak suggest differences between VMEC results and other modeling approaches [60], more recent studies have successfully applied VMEC to study the effect of RMPs on the ASDEX Upgrade tokamak [61–63], suggesting that the approach can be useful as an initial approach to studying nonlinear MHD problems.

It is also possible to use an equilibrium solver to find nonlinearly saturated equilibrium states, corresponding to internal and external MHD instabilities [64, 65].

VMEC computations have been successful in identifying saturated core (1, 1) ideal MHD instabilities, which have been linked to the experimentally observed 'snakes' in JET [66], and stationary states near the MHD stability threshold of sawtooth crashes [67]. The latter stationary states have also been observed in nonlinear MHD simulations [68], and compared with experimental findings on the TCV tokamak [69]. More recently, external instabilities have been identified with the application of exploring edge harmonic oscillations (EHOs) [70]. These computations have been tested against ideal MHD stability codes, showing good agreement between the initial eigenfunctions of the MHD instability and the final nonlinear perturbation of the flux surfaces observed in VMEC [65, 71]. Prior to this thesis work, these calculations of external modes from VMEC had yet to be validated against a nonlinear MHD code, as performed in Chapter 3.

There are a few studies which have applied the equilibrium approach to MHD stability problems in stellarators [72, 73], motivating discussion regarding the validity of this approach to approximating stellarator MHD phenomena. With respect to the non-ideal plasma terminating events that have been induced in W7-X, the VMEC computations could be a useful starting point for more detailed SPEC calculations of the phenomena. For external modes in QA configurations, saturated equilibria in VMEC would be a valuable starting point for transport calculations to see the negative influence they could have on confinement, and further validate the nonlinear approaches being developed to model stellarators in JOREK. Given the limited number of studies using this approach for stellarators, it is not clear what MHD activity the VMEC approach will be amenable to study. For this reason, an initial study of classical stellarators, as described in Chapter 4, was chosen as a starting point towards these longer term goals such that the performance of this approach when applied to stellarators could be assessed in a simpler geometry.

2.3.2 Convergence behaviours in VMEC

Before VMEC can be applied in this thesis to consider nonlinear MHD problems, the behaviour of the code needs to be better understood, such that it can be used appropriately. In this section, the correct convergence of the force residuals in nonlinear MHD studies is described. Several different convergence behaviours of the force residual, F_{R} are shown in Figure 2.2 for unperturbed and perturbed VMEC computations, which converge successfully, and a perturbed case, which fails to converge. In the unperturbed case, the force residual decreases monotonically, as is expected with the minimisation of the W_{MHD} energy. For the perturbed cases, it can be seen that the force residuals increase, as the instability is found and the equilibrium becomes out of force balance. Note that this often occurs at a relatively low residual value, below 10^{-13}, which would normally be considered well converged in equilibrium studies. If a new perturbed state is found, the residuals must fall as the new perturbed state is reached.

In many cases however, the force residuals continue to rise, until the VMEC algorithm detects the unfavourable behaviour. The equilibrium is then reset to an

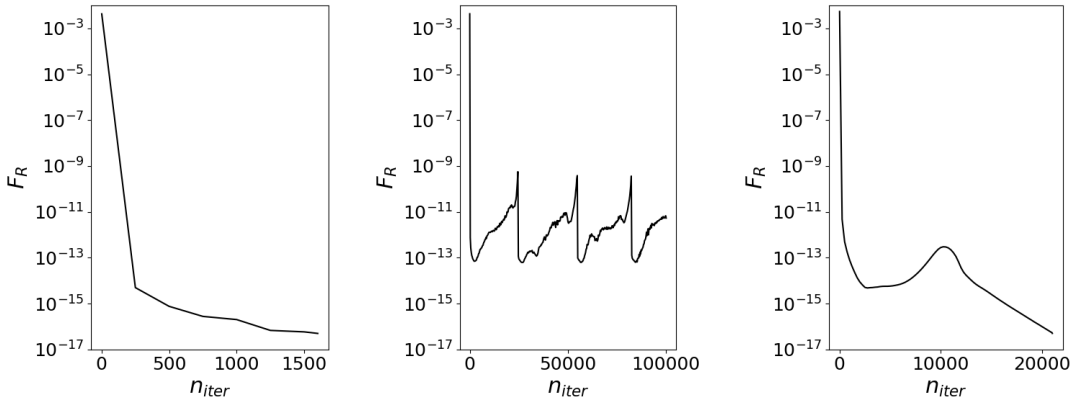

(a) (b) (c)

Figure 2.2: Plots of the force balance residuals for VMEC computations during the convergence. An unperturbed case (a) and perturbed cases with poor (b) and good (c) convergence to a nonlinear state are shown.

earlier stage, and the numerical time step parameter is decreased in an attempt to improve convergence. Though the residuals still remain relatively low compared to normal equilibrium studies, the results produced by these cases are either considered to be numerical instabilities, or real MHD instabilities that lead to such large perturbations that they can be considered disruptive. The results reported in this paper all have the benign convergence behaviour shown in Figure 2.2 (c).

It is challenging to construct MHD equilibria that will saturate nonlinearly in VMEC. This is because perturbed states can only be found by converging the equilibrium to force residuals that are well below the tolerances necessary for normal equilibrium studies. Large scale MHD structures corresponding to low (m, n) modes can be difficult to converge. Equally, small scale, high (m, n) modes require a large number of Fourier harmonics to converge and thus are similarly challenging to find. In addition, $n > 1$ perturbed states are typically only observed for RMP cases [58, 62], where the state is externally driven, and thus easier to find. In this work, medium scale perturbations between $m = 4$ and $m = 6$ were successfully converged for $n = 1$, when considering external kink instabilities, and so this is the parameter space that has been targeted in Chapter 3 and 4.

2.3.3 Conservation of helicity in VMEC

It has been shown how to use VMEC to appropriately converge to a nonlinearly saturated state in Section 2.3.2. At the same time, it is important to justify the physical validity of VMEC computations, which model nonlinear MHD phenomena. In particular, during VMEC iterations, the equilibrium is modified by a minimisation of the ideal MHD equilibrium energy, without use of the full ideal MHD time evolution equations. In such a way, the dynamics associated with the momen-

tum of the plasma, and the evolution of its kinetic energy are neglected. For this reason, it is difficult to justify that the trajectory of subsequent iterations follows a physical path. It has been argued in past studies that in order to use this approach for nonlinear MHD studies, physical links need to be enforced between the unperturbed axisymmetric equilibrium, and the final perturbed state of the free boundary computation [74].

As VMEC assumes the ideal MHD force balance, a reasonable choice for this constraint is to assume the conservation of helicity during the computation, because this quantity is conserved during the evolution of ideal MHD instabilities. This can be achieved by fixing ι during the computations, as shown by the following analysis. The global helicity, K, of an equilibrium is

$$K = \int \mathbf{A} \cdot \mathbf{B} \, dV, \tag{2.14}$$

where, in VMEC, the magnetic field, $\mathbf{B}$, is defined by the vector potential, $\mathbf{A}$, such that

$$\begin{aligned} \mathbf{B} &= \nabla \times \mathbf{A} \\ &= \nabla \times (\Phi(s)\nabla\theta^* - \Psi(s)\nabla\phi) \\ &= \Phi'(s)\nabla s \times \nabla\theta^* - \Psi'(s)\nabla s \times \nabla\phi, \end{aligned}$$

where Φ and Ψ are the toroidal and poloidal flux respectively, and s, θ, and ζ have their usual meanings as the radial, poloidal, and toroidal coordinates. θ^* is the transformed poloidal angle in straight field line coordinates. The local helicity can therefore be written as

$$\begin{aligned} \mathbf{A} \cdot \mathbf{B} &= (\Psi'\Phi - \Phi'\Psi) \left[\nabla s \cdot (\nabla\theta^* \times \nabla\phi)\right] \\ &= (\Psi'\Phi - \Phi'\Psi) \frac{1}{J^*}, \end{aligned}$$

where J^* is the Jacobian of the transformation from laboratory to plasma coordinates. Finally, it can be shown that equation 2.14 can be simplified to

$$K = 4\pi^2 \int_0^1 (\Psi'\Phi - \Phi'\Psi) \, ds. \tag{2.15}$$

As the ι profile, toroidal flux profile, $\Phi(s)$, and total toroidal flux are fixed during VMEC computations, the profile for the poloidal flux is also fixed, because

$$\Psi(s) = \Phi(s = 1) \int_0^s \iota(s) ds. \tag{2.16}$$

As such, the profiles in equation 2.15 are all fixed, such that the helicity is kept constant during the VMEC computation. Thus, constraining ι enforces a physically

meaningful link between the initial and final states, justifying the use of the method for studying nonlinear MHD. It should be noted that there is no reason to assume conservation of helicity is sufficient to guarantee a physically meaningful solution is obtained. As discussed further in Chapter 4, it is possible for multiple solutions to be obtained if only this constraint is enforced. This leads to the need to impose further physical constraints on the solution, as discussed in Section 4.2.

2.4 Linear MHD stability and the CASTOR3D code

Turning now to the explicit solution of the dynamical MHD problem, once an equilibrium point has been found, the question still remains - is the equilibrium stable to perturbations, which may naturally send the confined plasma into an unfavourable state where confinement is either partially, or fully lost? This question can be studied at different levels of complexity depending on how much information is desired about the stability properties. A framework for characterising MHD instabilities is constructed in Section 2.4.1. Linear perturbation theory is then outlined in Section 2.4.2, and can be used to develop models for understanding the growth rate, and structure of instabilities. Finally, the linear viscoresistive MHD code, CASTOR3D, is discussed.

2.4.1 Characterising MHD instabilities

Before turning to the linear theory of MHD instabilities, the main characteristics of MHD instabilities will be described, such that MHD perturbations can be distinguished from one another. To begin with, it is worth understanding the main stabilisation mechanisms that result from the magnetic field. The stabilising effects are magnetic field line bending, magnetic field line compression, and magnetic field line curvature, as shown in Figure 2.3. Each of these effects corresponds to a way in which the magnetic field resists a perturbation to its field structure. The first corresponds to the increase in magnetic tension produced by bending magnetic field lines. Similar to a taught wire, magnetic field lines tend to shorten when possible. And thus, a perturbation which increases the length of the field line will meet resistance from the magnetic field. The second mechanism represents the increase in magnetic pressure, as field lines are compressed by a perturbation. The last stabilising effect corresponds to the curvature of the magnetic field, and whether the perturbation acts to increase, or decrease the curvature. Increasing curvature is stabilising as once again the magnetic tension is increased.

The above stabilising effects are minimised on rational surfaces, where field lines close exactly in on themselves after a finite number of toroidal transits. This implies that the value of q will be rational, hence the name. In such a way, the mode that is resonant on the rational surface will more easily dominate over stabilising effects, such that instabilities can be characterised by the dominant poloidal and toroidal mode numbers, m and n, respectively, which contribute to the perturbation of the

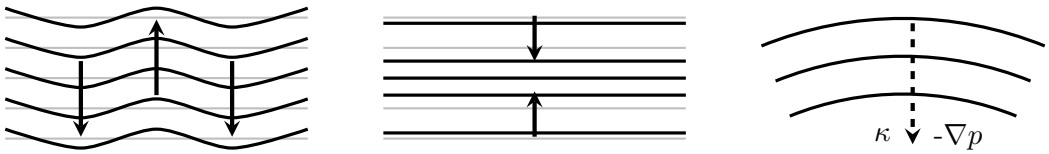

Figure 2.3: Sketch of stabilising terms in the MHD equations due to magnetic field line bending (left) and compression (centre). Grey lines show the unperturbed magnetic field. These stabilising terms can be related to the shear Alfvén and fast magnetosonic waves. Field line curvature (right) is only stabilising if the centre of curvature is in the opposite direction to the pressure gradient. Based on Figure 6.1.1 from [75].

initial equilibrium structure.

The main drive for such macroscopic MHD instabilities are the toroidal plasma current density and pressure gradient. It can be shown that a current carrying plasma always has a source of free energy to drive instabilities that push the plasma in the direction of thermodynamic equilibrium [3]. Equally, a pressure gradient must imply that the plasma can perform work. As a result, a magnetically confined plasma is always threatened by MHD instabilities, and needs to be carefully designed such that these sources of free energy cannot be released. Current driven instabilities are typically low n modes, which are global, such that the perturbation to the equilibrium extends over most of the plasma. Pressure driven modes are generally localised in regions of bad magnetic curvature. For a toroidal plasma, where the dominant magnetic field is toroidal, such that the centre of curvature is predominantly in the direction $-\hat{\mathbf{e}}_R$, pressure driven modes can be localised on the low field side of the torus, where the magnetic curvature is not favourable.

MHD instabilities can also be characterised by the assumed form of Ohm's law in equation 2.4. Ideal MHD perturbations can be analysed using the ideal Ohm's law, eliminating the viscoresistive terms from equations 2.5. Ideal instabilities are fast modes, which occur on the Alfvén timescale, on the order of microseconds. They are present even in the limit where the plasma is perfectly conducting, or ideal. This limit is generally valid in the core of hot fusion plasmas. Ideal MHD instabilities are subject to the *frozen-in flux* theorem, which implies that the magnetic field moves with the plasma, such that its topology cannot break down, and magnetic flux surfaces are maintained [76].

Over the long timescales of a plasma discharge, or close to the edge of the plasma, where the temperature decreases, resistive modes, driven by the $\eta\mathbf{J}$ term in equations 2.5, are possible. As discussed in Section 1.3.2, a finite resistivity enables magnetic reconnection and island formation — the rearrangement of a plasma's magnetic topology by non-ideal, diffusive processes. While resistivity is often the cause of the magnetic diffusion needed to drive reconnection, it should be noted that if other two fluid effects are included in equation 2.4, they can also lead to forms of non-ideal reconnection. Ideal MHD instabilities generally have a non-ideal

analogue. The resistive analogue is normally observed close to the stability boundary of the ideal MHD instability, once the ideal mode has been stabilised. Broadly speaking, the resistive stability boundary envelopes the ideal instability, as shown in Figure 5 of [77].

Lastly, MHD instabilities can be characterised by whether they are internal or external modes. Internal modes occur within the plasma volume, and do not require a motion of the plasma boundary. In such a way, such modes can occur, even when the plasma is surrounded by a perfectly conducting vessel, which holds the plasma boundary fixed. External modes on the other hand imply a motion of the plasma surface. In this case, it is necessary to take into account the interaction with the vacuum region in order to study the mode — a free boundary computation, as discussed in Section 2.4.2.

2.4.2 Linear perturbation theory

The question of stability itself can be answered by using linear perturbation theory, where the fluid variables in the MHD equations, $Q(\mathbf{x}, t)$, are treated using an ordering.

$$Q\left(\mathbf{x}, t\right) = Q_0\left(\mathbf{x}\right) + Q_1\left(\mathbf{x}, t\right) \tag{2.17}$$

The 0^{th} order quantities are used to describe the stationary equilibrium, while 1^{st} order quantities describe a perturbation to the equilibrium condition, which evolves in time. Higher order terms are considered nonlinear and neglected. Typically, the stationary equilibrium, $\mathbf{v}_0 = 0$, is given an instantaneous velocity perturbation, $\mathbf{v}_1 = \frac{\partial \boldsymbol{\xi}}{\partial t}$, where $\boldsymbol{\xi}$ is the perturbed displacement from the equilibrium condition. If this ordering is applied to the ideal MHD equations, neglecting nonlinear terms, as well as the sources, and diffusive terms, the following linearised equations are obtained

$$\begin{aligned}
\frac{\partial \rho_1}{\partial t} + \nabla \cdot \left(\rho_0 \frac{\partial \boldsymbol{\xi}}{\partial t}\right) &= 0, \\
\rho \frac{\partial^2 \boldsymbol{\xi}}{\partial t^2} &= \mathbf{J}_0 \times \mathbf{B}_1 + \mathbf{J}_1 \times \mathbf{B}_0 - \nabla p_1, \\
\frac{\partial p_1}{\partial t} + \frac{\partial \boldsymbol{\xi}}{\partial t} \cdot \nabla p_0 &= -\gamma p_0 \nabla \cdot \frac{\partial \boldsymbol{\xi}}{\partial t}, \\
\frac{\partial \mathbf{B}_1}{\partial t} &= \nabla \times \left(\frac{\partial \boldsymbol{\xi}}{\partial t} \times \mathbf{B}_0\right), \\
\mu_0 \mathbf{J}_1 &= \nabla \times \mathbf{B}_1, \\
\nabla \cdot \mathbf{B}_1 &= 0
\end{aligned} \tag{2.18}$$

Because tokamaks and stellarators are periodic in the poloidal and toroidal di-

rection, it is reasonable to assume a perturbation with the form

$$\boldsymbol{\xi}(s,\theta,\zeta,t) = \sum_{m=-\infty}^{\infty}\sum_{n=-\infty}^{\infty} \boldsymbol{\xi}_{\mathrm{m,n}}(s) e^{-i(m\theta+n\zeta)} e^{-i\omega t}, \tag{2.19}$$

where ω is the frequency of the perturbation, and m and n are the poloidal and toroidal mode numbers characterising the periodic spatial dependence of the perturbation. Using equation 2.19, the linearised momentum equation becomes

$$-\omega^2 \rho_0 \boldsymbol{\xi} = \mathbf{J}_0 \times \mathbf{B}_1 + \mathbf{J}_1 \times \mathbf{B}_0 - \nabla p_1 = \mathbf{F}(\boldsymbol{\xi}). \tag{2.20}$$

Stability can therefore be determined by the sign of ω^2. If negative, the system is unstable, corresponding to exponential growth, and if positive, the motion corresponds to an oscillation around the equilibrium state. While instructive, solving for ω, which corresponds to the growth rate or oscillation frequency, is often not trivial and provides more information than necessary. An equation for the work done on the plasma by its perturbed motion can be more instructive. The total work done on a confined plasma-vacuum system, δW, can be described by

$$\delta W = \delta W_{\mathrm{P}} + \delta W_{\mathrm{S}} + \delta W_{\mathrm{V}}, \tag{2.21}$$

where δW_{P} corresponds to the change in potential energy across the plasma volume, δW_{S} is the change in energy as a result of the deformation of the plasma boundary, and δW_{V} is the change in the magnetic energy in the vacuum surrounding the plasma. For perturbations where the plasma boundary is fixed, δW_{V} and δW_{S} can be neglected. This thesis is concerned with external modes, and so this simplifying assumption cannot be made.

Before proceeding to consider the terms in equation 2.21, it is important to understand how the change in potential energy, $\delta W = \frac{1}{2}\int \boldsymbol{\xi} \cdot \mathbf{F}(\boldsymbol{\xi}) dV$, leads to poloidal and toroidal mode coupling of MHD instabilities. It is discussed in [78] that terms in 2.21 consist of two perturbed quantities of the form in equation 2.19, and one equilibrium quantity, which can be described similar to the flux surfaces in equation 2.12, using poloidal harmonics m and toroidal harmonics nN_{p}. In the poloidal direction, this can lead to non-zero contributions from all combinations of perturbed and equilibrium harmonics, such that different poloidal modes can contribute to the same eigenvalue of system. In such a way, modes can be *poloidally coupled* in both tokamaks and stellarators when equilibria are shaped poloidally. In the toroidal direction, only particular combinations of the toroidal harmonics can be combined together in the same eigenvalue, due to the periodicity of the system. This separates instabilities in configurations with $N_{\mathrm{p}} > 0$ into *toroidal mode families*. The number of toroidal mode families, N_{f}, is defined by

$$N_{\mathrm{f}} = \lfloor \frac{N_{\mathrm{p}}}{2} \rfloor + 1, \tag{2.22}$$

where $\lfloor A \rfloor$ represents a floor function, returning the largest integer value below A.

Returning to the task of defining the individual terms in equation 2.21, δW_{P} is given by

$$\begin{aligned}\delta W_{\mathrm{P}} = \int_P \{ &\mid \mathbf{Q}_\perp \mid^2 + B^2 \mid \nabla \cdot \boldsymbol{\xi}_\perp + 2\boldsymbol{\xi}_\perp \cdot \kappa \mid^2 + \mu_0 \gamma p \mid \nabla \cdot \boldsymbol{\xi} \mid^2 \\ &- 2\mu_0 \left(\boldsymbol{\xi}_\perp \cdot \nabla p\right) \left(\boldsymbol{\xi}_\perp^* \cdot \kappa\right) \\ &- \mu_0 \mathbf{J}_\parallel \boldsymbol{\xi}_\perp^* \times \mathbf{b} \cdot \mathbf{Q}_\perp \} dV.\end{aligned} \tag{2.23}$$

The first three terms on the righthand side can be related to the shear Alfvén wave, fast magnetosonic wave, slow magnetosonic wave, respectively. The remaining two terms can be related to the driving mechanisms for instabilities, namely the pressure gradient, and parallel current density.

The surface energy is given by

$$\delta W_{\mathrm{S}} = \frac{1}{2\mu_0} \int_{S_{\mathrm{p}}} \left|\mathbf{n} \cdot \xi_\perp\right|^2 \mathbf{n} \cdot \left[\!\left[\nabla \left(\frac{B^2}{2} + \mu_0 p \right) \right]\!\right] dS, \tag{2.24}$$

where $\mathbf{n}$ is the normal to the plasma boundary, and $[\![A]\!]$ is the jump in A across the plasma-vacuum interface. This term is typically zero, unless a surface current flows on the plasma-vacuum boundary [12]. Lastly, the energy in the vacuum region can be calculated as

$$\delta W_{\mathrm{V}} = \frac{1}{2\mu_0} \int_V \left|\hat{\mathbf{B}}_\mathbf{1}\right|^2 dV. \tag{2.25}$$

Note that $\hat{\mathbf{B}}_\mathbf{1}$ is not the externally generated magnetic field, but the total perturbed magnetic field in the vacuum region as a result of external field coils and the perturbed plasma current. The modification of the energy in the vacuum region will become important in the discussion of using VMEC to model free boundary perturbations in Chapter 4.

If the total change in energy of a system is negative, the equilibrium has released some of the potential energy of the plasma, and thus must be unstable. Therefore, most early linear analytical work of MHD equilibria studied the energy equation in simplified geometry subject to an applied perturbation. The perturbation itself can be arbitrary. It only needs to be shown that a single perturbation reduces the potential energy in order to prove the equilibrium is unstable. This energy formulation can be extended to include the terms for resistive MHD, however this formulation is not considered here. Simplified forms of the work formulation exist for cylindrical plasmas. The simplest method for assessing MHD stability is Newcomb's method [79], in which a cylindrical plasma is considered, subject to incompressible, perpendicular perturbations.

2.4.3 CASTOR3D

In general, the simplified approaches described in Section 2.4.2 are not amenable to poloidally shaped, or non-axisymmetric configurations. For these more advanced geometries, numerical models are necessary to solve the problem. There are many existing numerical codes, which use different sophisticated approaches to solve for MHD perturbations, such as KINX, MARS-F, and CAS3D [78, 80, 81]. CASTOR3D [82] is one of the state of the art linear viscoresistive MHD codes, which can be applied to study both axisymmetric, and non-axisymmetric plasmas. The code is an extended, re-implementation of the original CASTOR (Complex Alfvén Spectrum in Toroidal Geometry) code [83] and solves the extended eigenvalue problem for the plasma-vacuum system, assuming the perturbed viscoresistive MHD equations, solved in the weak form, as described in [84, 85]. 1D radial finite elements are used in combination with a 2D Fourier representation of the poloidal and toroidal dependence of both equilibrium and perturbed quantities within the plasma region. To represent the response of external wall structures, the code is coupled to the resistive wall code, STARWALL [86].

One of the major advantages of this code over other approaches is its use of generalised flux surface coordinates, as described in Section 2.2. While SFL coordinates are beneficial in most situations as the description of the MHD perturbation is simplified in this coordinate system, this rule of thumb is not valid for x-point geometries [41], where the SFL coordinates become ill-defined around the x-point [77]. For such cases, generalised flux surface coordinates, such as the VMEC coordinate system, can be more effective. CASTOR3D is used throughout this thesis, to scan the linear parameter space of test cases, and to benchmark the nonlinear models that have been used to extend analysis into the nonlinear phase.

2.5 Nonlinear MHD dynamics and the JOREK code

Beyond the question of initial instability, the question still remains what nonlinear dynamics the perturbation will lead to. It is often observed that the linearly dominant perturbation does not lead the nonlinear dynamics. As the initial perturbation grows, and saturates, it can destabilise secondary instabilities which overtake the initial perturbation. Equally, a fast growing linear instability does not necessarily pose a threat to the confinement of an equilibrium if its nonlinear saturation amplitude is small enough to not significantly change the magnetic geometry. As such, linear analysis, while an essential part of the description of MHD dynamics, cannot be used to define the operational limits of toroidally confined plasmas.

A nonlinear approach to MHD in general requires a numerical solution. Analytic models exist [87], but these models can only be applied to simplified geometries. There are several state of the art nonlinear MHD codes used in the fusion community, such as M3D-C^1, NIMROD, and JOREK [38, 39, 42]. In this section, the numerical methods used in JOREK will be outlined.

2.5.1 Reduced MHD

When considering nonlinear problems, evolving the set of MHD equations of Section 2.1 remains computationally expensive. And so, when appropriate, further approximations can be made in order to achieve a reduced set of equations. A typical reduction removes the fast MHD waves from the system, which are often unnecessary in dynamics where field compression is not of interest. Removing the fast magnetosonic wave from the analysis has the advantage that it reduces the size of the system of equations that needs to be solved for, and removes the constraint resolving this wave imposes on the numerical time step used in nonlinear codes.

A hierarchy of ansatz based stellarator capable reduced MHD models was recently derived by N. Nikulsin in [45]. The ansatz used for the full MHD magnetic field and velocity are defined as

$$.\mathbf{B} = \nabla\chi + \nabla\Psi \times \nabla\chi + \nabla\Omega \times \nabla\Psi_{\mathrm{v}} \tag{2.26}$$

$$\mathbf{v} = \frac{\nabla\Phi \times \nabla\chi}{B_{\mathrm{v}}^2} + v_{\parallel}\mathbf{B} + \nabla^{\perp}\zeta, \tag{2.27}$$

where $\nabla\chi$ is used to represent the vacuum magnetic field, and B_{v} is its magnitude. It can be shown that the momentum equation associated with each of the scalar functions, Φ, $v_{\parallel}$, and ζ approximately captures the shear Alfvén, acoustic, and compressional Alfvén waves, respectively. In the MHD dynamics of interest, the compressional Alfvén wave represented by ζ and Ω can be neglected. The reduction of this ansatz sets these terms to zero. Of course, in order to solve this system of equations, projection operators need to be defined so that the number of equations is equal to the number of unknowns being solved for.

If the equations are simplified by assuming that the vacuum magnetic field is purely toroidal, as in tokamaks, the reduced MHD equations as defined in the tokamak version of the JOREK code are recovered [42, 88]

$$\frac{\partial\rho}{\partial t} = -\nabla\cdot(\rho\mathbf{v}) + \nabla\cdot(D_{\perp}\nabla_{\perp}\rho) + S_{\rho} \tag{2.28}$$

$$\hat{\mathbf{e}}_{\phi}\cdot\nabla\times\left(\rho\frac{\partial\mathbf{v}}{\partial t} = -\rho\left(\mathbf{v}\cdot\nabla\right)\mathbf{v} - \nabla\left(\rho T\right) + \mathbf{J}\times\mathbf{B} + \mu\Delta\mathbf{v} + S_{\mathrm{V}}\right) \tag{2.29}$$

$$\mathbf{B}\cdot\left(\rho\frac{\partial\mathbf{v}}{\partial t} = -\rho\left(\mathbf{v}\cdot\nabla\right)\mathbf{v} - \nabla\left(\rho T\right) + \mathbf{J}\times\mathbf{B} + \mu\Delta\mathbf{v} + S_{\mathrm{V}}\right) \tag{2.30}$$

$$\rho\frac{\partial T}{\partial t} = -\rho\mathbf{v}\cdot\nabla T - \left(\gamma-1\right)\rho T\nabla\cdot\mathbf{v} + \nabla\cdot\left(\kappa_{\perp}\nabla_{\perp} + \kappa_{\parallel}T\nabla_{\parallel}T\right) + S_{\mathrm{T}} \tag{2.31}$$

$$\frac{1}{R^2}\frac{\partial\Psi}{\partial t} = \frac{\eta}{R^2}j - \frac{1}{R}\left[u,\Psi\right] - \frac{F_0}{R^2}\frac{\partial u}{\partial\phi} \tag{2.32}$$

The Poisson bracket in equation 2.32 is defined as $[f,g] = \hat{\mathbf{e}}_{\phi}\cdot\left(\nabla f\times\nabla g\right)$. In this model, the magnetic field is defined as

$$\mathbf{B} = \frac{F_0}{R}\hat{\mathbf{e}}_{\phi} + \frac{1}{R}\nabla\Psi\times\hat{\mathbf{e}}_{\phi} \tag{2.33}$$

where $F_0 = R_0 B_{\phi 0}$ is spatially and temporally constant, and $\hat{\mathbf{e}}_{\phi}$ is the normalised toroidal basis vector in cylindrical coordinates. In such a way, the toroidal field is held constant through the simulation, while Ψ is evolved in time. In reduced MHD, the velocity is defined as

$$\mathbf{v} = -R\nabla u\times\hat{\mathbf{e}}_{\phi} + \frac{m_{\mathrm{i}}R}{eF_0\rho}\nabla p_{\mathrm{i}}\times\hat{\mathbf{e}}_{\phi} + v_{\parallel}\mathbf{B} \tag{2.34}$$

where $u = \varphi/F_0$ with φ as the electrostatic potential, such that the first term represents the $\mathbf{E}\times\mathbf{B}$ velocity. The second term is the source for diamagnetic flows, and the third describes flows along the magnetic field. Therefore, reduced MHD JOREK simulations only need to solve for a system of five unknowns (ψ, u, $v_{\parallel}$, T, and ρ) for experimentally relevant simulations of such modes. It should be noted that JOREK also uses two auxiliary equations for the toroidal plasma current

$$j = \Delta^{*}\Psi, \tag{2.35}$$

and fluid vorticity

$$\omega = \nabla\cdot\nabla_{\mathrm{pol}}u. \tag{2.36}$$

These equations are important for eliminating high order derivatives of the poloidal flux and u, such that the discrete system remains smooth using cubic finite elements, improving numerical stability. Regarding numerical stability, it should be noted that hyper-viscosity and hyper-resistivity, μ_{num} and η_{num}, terms are often added to equations 2.29, and 2.32, respectively, to improve numerical stability.

These terms act to damp fourth order derivatives of the poloidal flux and fluid vorticity, $\omega = \nabla \cdot \nabla_{\mathrm{pol}} u$, respectively, in order to prevent the development of sub-grid resolution numerical structures.

This reduced tokamak version of the MHD equations is used for most of the nonlinear simulations carried out in this thesis. It should be noted that JOREK has both reduced and full MHD models. The full MHD model is particularly useful for the study of high β internal modes [89]. For the external modes considered in this thesis, the reduced MHD model is fully sufficient for capturing the relevant physics. In Section 2.6, the model is modified to include an axisymmetric representation of the stellarator field, which is used for preliminary nonlinear studies of such devices.

2.5.2 Spatial discretisation

In JOREK, the poloidal planes are described by a 2D isoparametric Bézier finite element grid. The finite elements are quadrilateral, such that the coordinates and physics variables can then be written as

$$\mathbf{X}(s,t) = \sum_{\mathrm{i,j}} \mathbf{P}_{\mathrm{i,j}} B^3_{\mathrm{i,j}}(s,t) = \sum_{\mathrm{i,j}} \mathbf{P}_{\mathrm{i,j}} B^3_{\mathrm{i}}(s) B^3_{\mathrm{j}}(t), \tag{2.37}$$

where

$$B^3_{\mathrm{i}}(s) = \frac{3!}{i!(3-i!)} s^i (1-s)^{3-i}. \tag{2.38}$$

s and t are the local element coordinates, and $\mathbf{P}_{i,j}$ are the control points of the finite element. G^1 continuity across elements is ensured by enforcing additional constraints on these control points [43]. The above poloidal representation is combined with a toroidal Fourier representation for the physics variables.

The basis outlined above is versatile, and can be used to construct flux aligned grids, which are typically used in nonlinear MHD simulations to minimise numerical errors in parallel transport. Mesh refinement is in theory possible [43], however in practise is not used.

2.5.3 Time stepping

A Crank-Nicolson or Gears implicit time stepping scheme is typically used to advance the physics variables. Defining the system of equations to be solved as $\partial \mathbf{A}(\mathbf{u}) / \partial t = \mathbf{B}(\mathbf{u}, t)$, where $\mathbf{u}$ represents a vector of the physics variables to be solved, a general form of the discretised time evolution can be written as

$$\left[(1+\xi) \left(\frac{\partial \mathbf{A}}{\partial \mathbf{u}} \right)^{\mathrm{n}} - \Delta t \theta \left(\frac{\partial \mathbf{B}}{\partial \mathbf{u}} \right)^{\mathrm{n}} \right] \delta \mathbf{u}^{\mathrm{n}} = \Delta t \mathbf{B}^{\mathrm{n}} + \xi \left(\frac{\partial \mathbf{A}}{\partial \mathbf{u}} \right)^{\mathrm{n}} \delta \mathbf{u}^{\mathrm{n-1}}, \tag{2.39}$$

where n represents the time step, and $\delta \mathbf{u}^{\mathrm{n}} = \mathbf{u}^{\mathrm{n+1}} - \mathbf{u}^{\mathrm{n}}$. ξ and θ are constants used to change between Crank-Nicolson ($\theta = 0.5, \xi = 0.0$) and BDF5/Gears ($\theta =$

$1.0, \xi = 0.5$) time stepping. Equation 2.39 leads to a large sparse matrix that is iteratively solved using GMRES [90]. The solution to the block diagonal matrices formed by individual toroidal harmonics is typically solved using PASTIX [91], or STRUMPACK [92], and used as a pre-conditioner for the solution to the full system of equations.

2.6 Axisymmetric approximations of stellarators

As described in Section 1.4, JOREK was written for the simulation of tokamaks, and has only recently been extended to model stellarators during the period in which this thesis was carried out. In this section, the simplest nonlinear model implemented in the JOREK code for simulating stellarators will be considered. This model "averages out" toroidal effects, such that the stellarator can be modelled axisymmetrically. In Section 2.6.1, the original axisymmetric model of a stellarator is outlined, and its previous applications are discussed. This original ordering approach makes use of an analytic representation of the externally generated magnetic field. The implementation of a similar model in the JOREK code is then outlined in Section 2.6.2, where this analytic magnetic field representation is replaced with a numerically computed *virtual current*, which generates an equivalent toroidally averaged external poloidal field. A method for numerically constructing equilibria with this method, and the necessary modification of the reduced MHD model in JOREK used for the time evolution is outlined.

2.6.1 Stellarator expansion

Stellarator theory has always lagged behind tokamak theory, because of the higher complexity of modeling 3D configurations. Early stellarator theory was devoted to developing an approximation to the stellarator equilibrium based on an ordering approach. The most successful early model was the stellarator expansion laid out by Greene and Johnson [50]. This approximation assumes that the externally generated poloidal field, δ, is one order smaller than the dominant toroidal field. The inverse aspect ratio of the stellarator, ε, is in turn one order smaller than δ, such that a large aspect ratio is assumed. In addition, the expansion assumes a planar magnetic axis, which does not vary toroidally around the device. This leads to the following ordering of terms in the equilibrium

$$\varepsilon = \frac{r}{R} \qquad \delta = \varepsilon^{\frac{1}{2}} \qquad \beta = \varepsilon \qquad N_\mathrm{p} = \frac{1}{\varepsilon} \qquad l = 1, \tag{2.40}$$

where N_p is the number of field periods, and l refers to the poloidal periodicity number of the helical field coils. The above ordering is similar to the high beta tokamak expansion, with the inclusion of a large helical field, δ, to represent the

external rotational transform, leading to a modified Grad Shafranov equation for the equilibrium [52]

$$\nabla_\perp^2 \psi = -G(\psi) - \frac{\partial \beta}{\partial \psi}\left(\frac{r}{R_0}\cos(\theta) + |\nabla_\perp V|^2 + h^2|V|^2\right) - \frac{i}{h}\nabla_\perp^2\left(\hat{\mathbf{e}}_\phi.\nabla_\perp V^* \times \nabla_\perp V\right), \tag{2.41}$$

where $G(\psi)$ plays the role of $FF'(\psi)$ and $\partial\beta/\partial\psi$ is a normalised pressure gradient, similar to p' in equation 2.9. Equation 2.41 includes an additional term, $V(r,\theta)$, representing the external field coils

$$V(r,\theta) = \sum_i V_{\mathrm{l}} I_{\mathrm{l}}(hr) e^{il\theta}, \tag{2.42}$$

where $h = N_{\mathrm{p}}/R_0$, V_{l} are coefficients defining the magnitude of the externally applied helical field, and $I_{\mathrm{l}}(hr)$ are modified Bessel functions. Typically, the potential for the external field is an input to the equilibrium calculation. The potential coefficients are computed by fitting the representation to the vacuum magnetic field produced by the equilibrium's coil set [93]. As such, the expansion acts effectively as an axisymmetric approximation, where the effect of the stellarator fields are included in a toroidally averaged sense. This approach to calculating three dimensional equilibria was used in the first theoretical studies of stellarator MHD stability [94].

Later this expansion was used to generate a modified form of Newcomb's stability criterion, and the tearing mode equation, which included the effect of a toroidally averaged rotational transform [95]. This was used to assess tearing modes and kink instabilities in current carrying stellarators, later being applied to explain disruptions observed in W7-A experimental campaigns [32]. A nonlinear model similar to that developed in this thesis was previously developed by Wakatani and Strauss [96, 97]. Wakatani used the model to look at (1, 1) internal kink modes and disruptions in current carrying stellarators [98]. Using a similar approach, a simple model for stability against VDEs was developed to understand the fraction of rotational transform necessary to stabilise such modes in stellarators, using an axisymmetric approximation [30]. This model was later used to understand VDEs occurring on the Compact Toroidal Hybrid [31]. Such models have provided insight into MHD phenomena experimentally observed on W7-A and W7-AS, as well as being applied to predict the stability properties for NCSX [24, 32, 34]. More recently, the model has been used to understand plasma terminating events in W7-X [99]

In such a way, it can be said that axisymmetric approximations of stellarators have been used effectively to gain insights into the behaviour of such devices. A significant part of this thesis is the development of similar axisymmetric approximations within the JOREK code, to model the nonlinear dynamics of modern stellarators. The model in JOREK differs from others in the sense that the external rotational transform is modeled using axisymmetric virtual currents that can be calculated from modern equilibrium codes. Such currents are attributed to rigid

coils that are assumed to be immersed inside the confined plasma, but physically shielded from it, such that the two do not interact. The virtual currents effectively play the role of the external field represented by $V(r, \theta)$ in equation 2.41.

This method allows for an easier representation of vacuum fields that are more complicated than the helically symmetric fields used in early studies, without requiring any knowledge of the vacuum field itself, which would normally be necessary in order to compute the coefficients of $V(r, \theta)$. In the next section, it is shown how fixed boundary VMEC computations can be used to obtain an appropriate description of the virtual current to approximate the vacuum field of the modelled stellarator.

2.6.2 Virtual current model

This section will outline the procedure for calculating the virtual currents used in JOREK, and including them in the time evolution equations. It will be shown that the implementation requires minimal changes to the equilibrium solver, and time stepping, such that the model enables a fast track to a simplified, nonlinear model for assessing nonlinear MHD in stellarators.

VMEC workflow for constructing equilibria

In order to make use of the axisymmetric approximation of a stellarator, an axisymmetric equilibrium first needs to be constructed, which appropriately captures the physics of the non-axisymmetric device. As described in detail in [85], a stellarator equilibrium can be mapped onto an axisymmetric domain, using VMEC. The main steps in constructing such approximations for simulating internal modes is shown in Figure 2.4 (a). The $n = 0$ Fourier components of the stellarator boundary are normally used as the axisymmetric equilibrium boundary, in order to preserve the same toroidally averaged shaping of the plasma. The same pressure, p_{stel}, and rotational transform, ι_{stel}, profiles are used as in the original stellarator. For the axisymmetric equilibrium to have the same ι profile, the poloidal field generated externally must be replaced by increasing the toroidal current in the new axisymmetric device, I_{tok}, when compared with the original stellarator, I_{stel}.

This type of axisymmetric approximation is referred to as the *equivalent tokamak approximation*. The increase in the toroidal current is typically expected to make the equilibrium more unstable than the stellarator it is intended to represent, although it is shown in Section 5.3 that this is not always the case. In order to produce a better axisymmetric approximation, the physics of an external rotational transform must be replicated. This is possible by removing the additional current in the equivalent tokamak from the plasma, instead attributing it to virtual currents within the torus. This leads to a model referred to as the *virtual current approximation*, where

$$I_{\mathrm{vc}}(s) = I_{\mathrm{p}}(s) + I_{\mathrm{v}}(s), \tag{2.43}$$

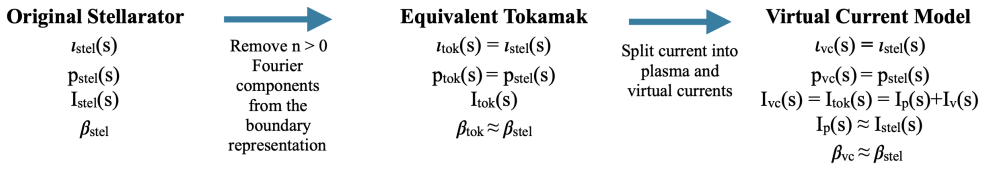

(a) Equivalent tokamak and virtual current model construction for internal modes

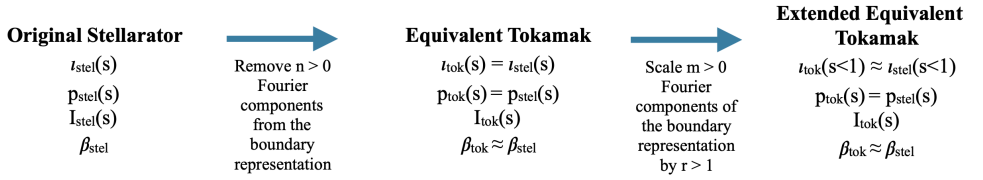

(b) Equivalent tokamak construction for external modes in JOREK

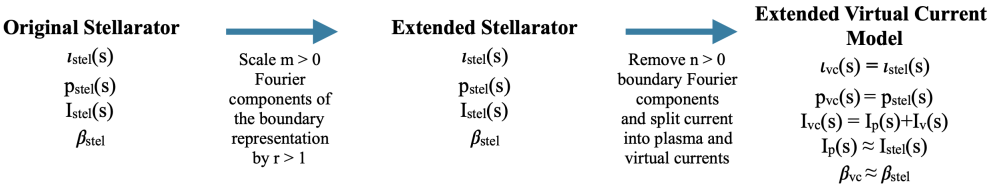

(c) Virtual current model construction for external modes in JOREK

Figure 2.4: Workflow for constructing the equivalent tokamak and virtual current model of a stellarator using VMEC for internal (a) and external (b-c) mode studies in JOREK. There are two main steps in the approach. The first is to modify the definition of the plasma boundary to be axisymmetric, preserving the pressure, and ι profiles of the original stellarator. This leads to an equivalent tokamak approximation. The virtual current model is constructed by splitting the toroidal current in the new axisymmetric equilibrium into plasma and virtual current components. For external modes, an additional step is necessary to extend the equilibrium into the vacuum region. This is necessary because of the JOREK boundary conditions, and to capture the correct rotational transform outside the plasma in the virtual current model.

defining I_p and I_v as the plasma and virtual current within a given toroidal configuration, respectively. s has its usual meaning as the radial flux surface coordinate. An example of these modified equilibrium profiles is given in Section 5.4, where external kink modes in a $l = 2$ and QA stellarator are studied.

Grad Shafranov Solution with Virtual Currents

In order to include I_v in the equilibrium description, the in-built Grad Shafranov solver in JOREK that initialises equilibria for nonlinear studies needs to be modified. The total current I_{vc} needs to be split between I_p and I_v in the solution of the

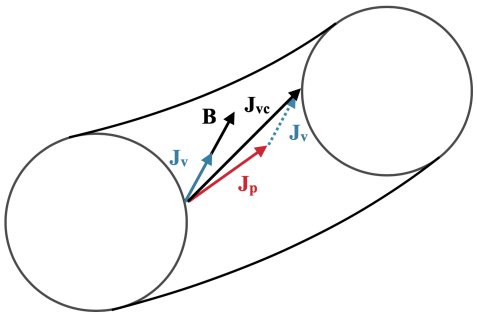

Figure 2.5: Sketch of virtual currents in a circular axisymmetric approximation of a stellarator. The total current density, $\mathbf{J}_{\mathrm{vc}}$, has contributions from virtual, $\mathbf{J}_{\mathrm{v}}$, and plasma, $\mathbf{J}_{\mathrm{p}}$, currents. The virtual current is along the total equilibrium magnetic field, $\mathbf{B}$, and as such does not modify the solution to the Grad Shafranov equation.

equilibrium equation. To do this, the equilibrium equation is modified such that

$$\begin{aligned}\Delta^{*}\Psi = j_{\mathrm{vc}}(\Psi, R) &= -\mu_0 R^2 p'(\Psi) - FF'(\Psi) \\ &= -\mu_0 R^2 p'(\Psi) - \left[F_{\mathrm{p}}F_{\mathrm{p}}'(\Psi) + F_{\mathrm{v}}F_{\mathrm{v}}'(\Psi)\right],\end{aligned} \tag{2.44}$$

where $j_{\mathrm{vc}}(\Psi, R)$ describes the total current density in the torus. The plasma and virtual current densities are then defined by

$$\mu_0 R\mathbf{J}_{\mathrm{p}} \cdot \hat{\mathbf{e}}_{\phi} = j_{\mathrm{p}} = -\mu_0 R^2 p'(\Psi) - F_{\mathrm{p}}F_{\mathrm{p}}'(\Psi) \tag{2.45}$$

$$\mu_0 R\mathbf{J}_{\mathrm{v}} \cdot \hat{\mathbf{e}}_{\phi} = j_{\mathrm{v}} = -F_{\mathrm{v}}F_{\mathrm{v}}'(\Psi). \tag{2.46}$$

As long as the virtual current introduced is along the magnetic field lines, as shown in Figure 2.5, this should not introduce an inconsistency into the force balance of the solution to the Grad Shafranov equation. As shown in Figure 2.5, the diamagnetic current represented by FF' is parallel to the total equilibrium magnetic field, and as such the virtual current removed from this term can be considered force free. In such a way, the virtual currents can be removed from the equilibrium without influencing the force balance. The modified solution to the Grad Shafranov equation therefore remains in equilibrium.

In order to be a meaningful approximation of the stellarator, the plasma current density of the virtual current model should approximate the plasma current density of the original stellarator as closely as possible. For this reason, j_{v} is chosen such that

$$j_{\mathrm{v}} = \mu_0\langle R\rangle\left[\langle\frac{j_{\mathrm{vc}}(\Psi, R)}{R}\rangle - \frac{dI_{\mathrm{stel}}}{dA_{\mathrm{vc}}}(\Psi)\right], \tag{2.47}$$

where $\langle\ \rangle$ refers to a flux surface averaged quantity, and A_{vc} is the toroidally averaged cross sectional area of a given flux surface in the axisymmetric approximation. To first order in the aspect ratio, this ensures that the stellarator and the virtual current model correspond to the same plasma current distribution, $I_{\mathrm{p}}(s) = I_{\mathrm{stel}}(s)\,(1 + O\,(\epsilon^2))$. The righthand side of the above equation is computed numerically from VMEC and JOREK. Equation 2.47 can then be used to define $I_{\mathrm{v}}(s)$ in equation 2.43, using

$$I_{\mathrm{v}}(s) = \int_0^{A_{\mathrm{vc}}(s)} \frac{j_{\mathrm{v}}}{R} dA_{\mathrm{vc}}. \tag{2.48}$$

When the toroidally averaged flux surfaces of the stellarator and axisymmetric approximation align, $I_{\mathrm{p}}(s) = I_{\mathrm{stel}}(s)$. This is normally true for low beta cases, as will be shown in Section 5.4.

For the simulation of external modes, the equilibrium construction becomes more complicated because of the representation of the vacuum region. The workflow for external modes is shown in Figure 2.4 (b) and (c). In JOREK simulations of external modes, the vacuum region needs to be included in the simulation domain, because the JOREK model used here applies a Dirichlet boundary condition on the poloidal velocity at the boundary. As such, this boundary condition needs to be sufficiently far from the plasma-vacuum interface so as not to interfere with the growth of external modes.

In addition to this, the vacuum magnetic shear of a tokamak and stellarator are different, due to the contribution to the magnetic field in the vacuum region from external helical coils. For this reason, to capture the correct rotational transform of the stellarator axisymmetrically in the virtual current approximation, virtual currents need to flow in the vacuum region to approximate the effect of these helical coils. This is important as the magnetic shear of the vacuum region has a stabilising effect on external modes.

For the studies of external modes in this thesis, the original fixed boundary stellarator equilibria are extended smoothly into the vacuum region, linearly scaling the edge toroidal flux with the new cross sectional area of the equilibrium. This extended domain is then transformed to a new axisymmetric approximation in the same way as has been previously described, preserving the correct magnetic shear of the stellarator in the vacuum region.

Time evolution

During the time evolution, the virtual current remains fixed in space and time. Equations 2.28 to 2.32 are modified for studies with the virtual current model, removing the parallel momentum equation to improve numerical stability. This is an acceptable simplification because perpendicular convection and parallel heat transport should dominate over parallel convection, as has been observed in comparable edge localized mode studies [100]. The momentum, pressure, induction,

and current equations require the following minor modifications to include virtual currents

$$\begin{aligned} R\nabla\cdot\left(R^2\rho\nabla_\perp\frac{\partial u}{\partial t}\right) = &\frac{1}{2}\left[R^2\left|\nabla_\perp u\right|^2, R^2\rho\right] \\ &+\left[R^4\rho\omega, u\right]+\left[\Psi, j_{\mathrm{vc}}-j_{\mathrm{v}}\right] \\ &-\frac{F_0}{R}\frac{\partial j_{\mathrm{vc}}}{\partial\phi}+\left[\rho T, R^2\right] \\ &+R\mu\left(T\right)\nabla^2\omega \end{aligned} \tag{2.49}$$

$$\begin{aligned} \frac{\partial\left(\rho T\right)}{\partial t} = &-\mathbf{v}\cdot\nabla\left(\rho T\right)-\gamma\rho T\nabla\cdot\mathbf{v} \\ &+\nabla\cdot\left(\kappa_\perp\nabla_\perp T+\kappa_\parallel\nabla_\parallel T\right) \\ &+\frac{2}{3R^2}\eta\left(T\right)\left(j_{\mathrm{vc}}-j_{\mathrm{v}}\right)^2+S_{\mathrm{p}} \end{aligned} \tag{2.50}$$

$$\frac{\partial\Psi}{\partial t} = R[\Psi, u]+\eta\left(j_{\mathrm{vc}}-j_{\mathrm{v}}\right)-F_0\frac{\partial u}{\partial\phi} \tag{2.51}$$

$$j_{\mathrm{vc}} = \Delta^*\Psi = j_{\mathrm{p}}+j_{\mathrm{v}} \tag{2.52}$$

.

The necessary modifications for the virtual current model are marked in blue, and amount to the inclusion of a virtual current, which is subtracted from the terms responsible for releasing free magnetic energy through ideal and resistive effects. The change made in equation 2.51 is equivalent to the addition of a current source, fixing the background virtual current. In equations 2.49 and 2.50, the virtual current is removed from the Ohmic heating term and Lorentz force, as the plasma should only experience the influence of its own current. The changes outlined above are easily implemented, allowing a fast, albeit qualitative assessment of stellarator nonlinear dynamics.

External kinks are modeled in this study in the no wall limit, keeping the $n = 0$ component fixed. The influence of virtual currents on the boundary conditions therefore also needs to be considered. The free boundary condition for $n > 0$ toroidal harmonics is included by coupling JOREK to the STARWALL code [86, 101]. This coupling enforces that

$$\mathbf{n}\cdot\mathbf{B}_{\mathrm{JOREK}} = \mathbf{n}\cdot\mathbf{B}_{\mathrm{STARWALL}} \tag{2.53}$$

$$\mathbf{n} \times \mathbf{B}_{\text{JOREK}} = \mathbf{n} \times \mathbf{B}_{\text{STARWALL}} \tag{2.54}$$

$$\mathbf{n} \cdot \mathbf{J}_{\text{JOREK}} = \mathbf{n} \cdot \mathbf{J}_{\text{STARWALL}} \tag{2.55}$$

where $\mathbf{n}$ refers to the normal vector on the JOREK simulation boundary. As the virtual current in the domain is parallel to the equilibrium magnetic field, there is no component normal to the plasma boundary. Equation (2.55) is therefore independent of the virtual currents in the domain. Equation 2.53 and 2.54 are implemented in terms of the total magnetic field [21]. The representation of the total magnetic field is unchanged in the virtual current model, and so there is no need to change the coupling between the two codes.

2.7 Discussion

In this section, the viscoresistive MHD equations have been derived and a framework for understanding MHD equilibrium, linear and nonlinear stability problems has been developed. Each part of this framework is necessary in the characterisation of the MHD properties of a fusion plasma.

Three codes that are used extensively in this thesis — VMEC, CASTOR3D and JOREK — have been briefly described. VMEC is used in most of the studies which follow in order to generate the starting equilibrium point for stability calculations. The methods described in Section 2.3 are used to study saturated nonlinear MHD perturbations. The reduced MHD models in JOREK are applied for more comprehensive nonlinear simulations, such that the viscoresistive time evolving dynamics can be studied. CASTOR3D is used mostly to linearly benchmark the nonlinear approaches used in this thesis, to demonstrate their fidelity.

3 Comparison of nonlinearly saturated external MHD modes in tokamaks with JOREK and VMEC

In this chapter, the use of VMEC as a method for studying nonlinearly saturated external MHD modes observed in JET-like tokamak equilibria is compared with nonlinear simulations using JOREK. In the context of this thesis, the purpose of this study was to test the validity of the equilibrium approach and identify the physical effects which can lead to deviations in the dynamics, such that the equilibrium approach can be used appropriately to model stellarators in Chapter 4. In Section 3.1, the saturated states found in VMEC that are used in the comparison — a (5, 1) external kink mode, and Edge Harmonic Oscillation (EHO) — are outlined. The set up of the JOREK simulations for the comparison with VMEC follows in Section 3.2. In Section 3.3, it is shown that for the external kink mode, there is good agreement between the two modelling approaches. This is likely because the simulated kink is dominated by a single toroidal harmonic. A more complicated test case representing an EHO is modelled in Section 3.4. The dynamics of the test case are more complex, because multiple toroidal harmonics are linearly unstable. In JOREK simulations, the different linearly unstable modes are shown to compete for nonlinear dominance, such that the saturated state found on the ideal MHD timescale differs from the VMEC result. Extending simulations into timescales where resistive effects can play a role, similar $n = 1$ perturbations can be found as observed using the equilibrium approach. The nonlinear dynamics that lead to this mode, and the similarities with the VMEC solution are studied. In Section 3.5, the implications of these results for future work considering stellarators with the equilibrium approach is discussed. The results of this thesis chapter have been published in [102].

3.1 VMEC results for saturated external modes in tokamaks

The test cases used in this study are based on modified versions of previously published results considering edge MHD instabilities in JET-like tokamaks [65]. The computations have assumed up-down symmetry, and used $N_s = 311$ radial grid points, and $m = 15$ poloidal harmonics. The modelling approach outlined in Section 2.3 is applied. For these tokamak cases, the unperturbed equilibria are converged axisymmetrically, such that the MHD instability is artificially suppressed. When searching for the perturbed state, $n = 6$ toroidal harmonics are used. In both

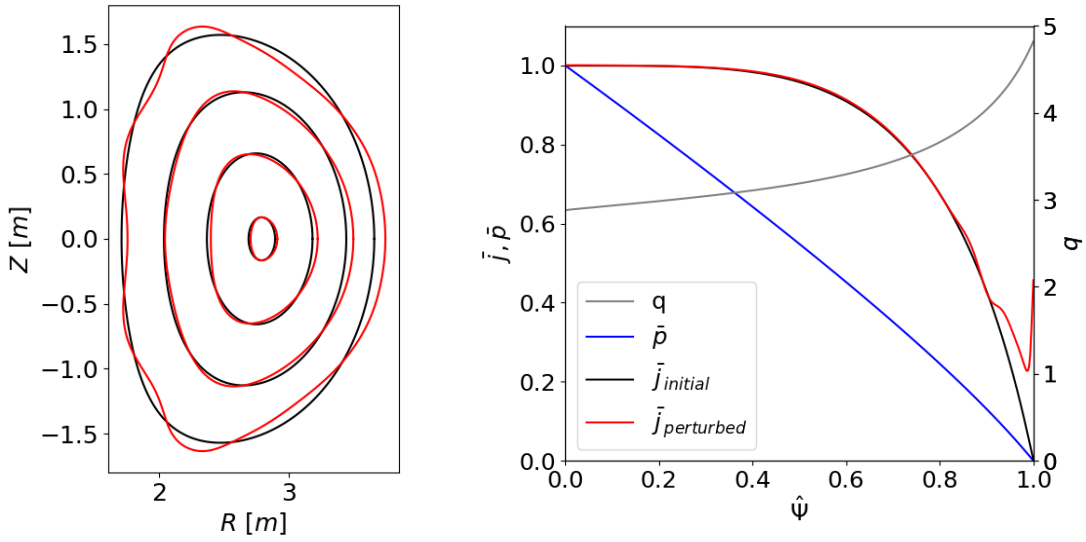

(a) (b)

Figure 3.1: Unperturbed (black) and perturbed (red) equilibrium flux surfaces at $\sqrt{\hat{\Phi}} = 0.1$, 0.3, 0.7 and 1.0 (a), and radial profiles (b) from VMEC for the external kink case.

cases, the equilibria are considered converged when the force residuals in VMEC fall below $f_{\text{tol}} = 5 \times 10^{-17}$. As discussed in Section 2.3.3, the VMEC computations are carried out constraining the q profile, to provide a physical link through helicity conservation between the axisymmetric and final perturbed state.

3.1.1 External kink observed in VMEC

The unperturbed equilibrium used in the external kink case is shown in Figure 3.1 (a). It has been shown previously that this case is a current driven external kink mode [65]. A quartic current profile and approximately linear pressure profile are assumed for the unperturbed equilibrium with respect to the normalised toroidal flux, as shown in Figure 3.1 (b). This leads to an edge safety factor that is just below 5, such that a (5, 1) ideal external kink mode can be found using VMEC. The saturated (5, 1) mode is shown in Figure 3.1 (a).

It can be seen in Figure 3.1 (b) that the modified toroidal current profile has a sharp increase in current near the plasma edge. This effect is similar to the surface currents that were observed in past calculations of fast major radius compression in tokamaks [103], and can be understood qualitatively in the following way; as the q profile is fixed during the development of the 3D perturbed state, the ratio of the poloidal and toroidal pitch angles of magnetic field lines must remain effectively constant. With the major and minor radius, and the toroidal field approximately

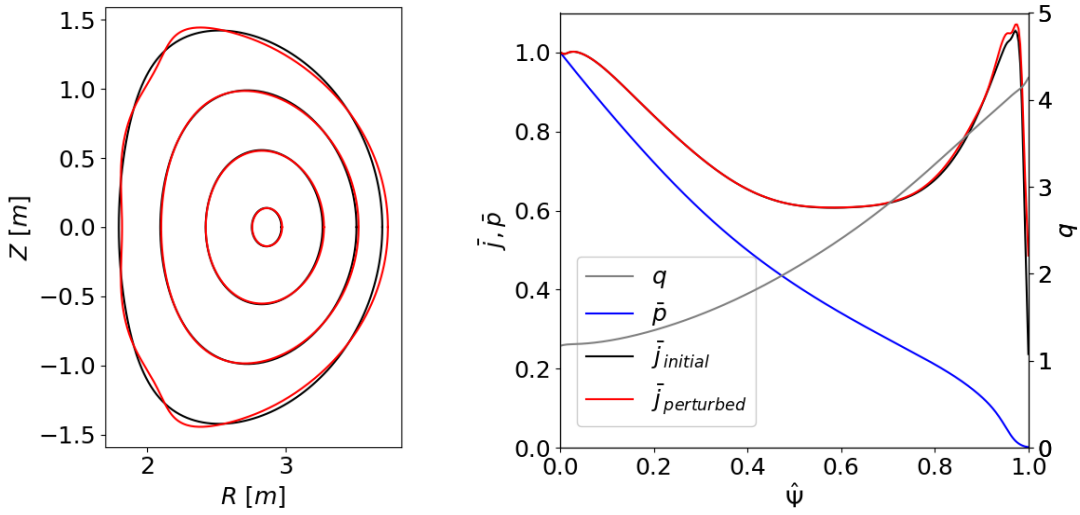

(a) (b)

Figure 3.2: Unperturbed and perturbed equilibrium flux surfaces at $\sqrt{\hat{\Phi}} = 0.1$, 0.3, 0.7 and 1.0
(a), and radial profiles (b) from VMEC for the edge harmonic oscillation case.

held constant, the poloidal field will vary according to

$$\mu_0 \int \mathbf{j} \cdot \mathbf{dS} = \oint \mathbf{B} \cdot \mathbf{dl}. \tag{3.1}$$

Considering Figure 3.1 (a), the total surface area is also approximately constant, while the line integral of the equilibrium flux surfaces has visibly increased. In such a way, the total plasma current should also increase to preserve the q profile. The current spike can be interpreted as the typical plasma current spike observed experimentally during fast MHD dynamics. This interpretation makes sense, given that the perturbed equilibrium is thought to be the saturated state obtained on the ideal timescale, just after the current spike observed in the time evolving dynamics.

3.1.2 Edge harmonic oscillation observed in VMEC

The EHO considered in Section 3.4 is based on the external-infernal (exfernal) mode [104] calculated using VMEC in [65]. These instabilities are typically observed in plasmas with a large edge bootstrap current generated by strong pressure gradients. The bootstrap current flattens the q profile near the plasma edge, allowing the large pressure drive in the edge region to strongly couple internal and external MHD perturbations.

The deformation of the last closed flux surface, and corresponding current spike is smaller in Figure 3.2 when compared to Figure 3.1. This is expected, as EHOs have

been referred to as kink-peeling modes in the literature [105, 106], which are more radially localised than global external kink modes. It should be noted that during the parameter scans carried out in this study, only the $n = 1$ dominant saturated mode was found in VMEC, even though the simulated test case is unstable to multiple low n toroidal harmonics, as shown in Section 3.4.

3.2 Set up of JOREK simulations for comparison

To model comparable instabilities to those computed in VMEC using JOREK, the same unperturbed equilibria can be obtained using its built-in Grad-Shafranov solver, preserving the pressure profile, q profile and plasma boundary from VMEC. This is, however, not sufficient for an accurate comparison, because ad-hoc diffusion parameters in JOREK can modify the equilibrium condition during the time evolution. This may influence the MHD dynamics in turn. In order to avoid this problem, an initial VMEC equilibrium is imported and run in JOREK axisymmetrically, such that the MHD instability is suppressed. Once the equilibrium profiles are approximately stationary over the simulated timescale, the new equilibrium profiles and plasma boundary are used to construct updated VMEC equilibria. These equilibria have been shown in Section 3.1, and are used in the comparison, such that the initial state used in the two approaches is consistent.

In Section 3.3 and 3.4, the assumed simulation conditions have tried to approximate the ideal MHD conditions assumed in VMEC. Parameter scans are then carried out for the EHO case with more physically meaningful parameters to understand the influence of resistivity and equilibrium flows on the nonlinear dynamics. As this study does not attempt to compare results with an experiment, the core plasma resistivity is chosen to be 1.9382×10^{-7} Ωm — higher than the experimentally relevant value — as a compromise between computational cost, and physical accuracy.

In VMEC, the vacuum region is assumed to be a perfect vacuum with no plasma currents flowing outside the plasma volume. To achieve similar vacuum conditions in JOREK, where the computational domain extends beyond the plasma boundary, the resistivity in the vacuum region is set to be artificially high. This prevents currents being induced by the plasma deformation, which could otherwise stabilise the plasma motion. For vacuum resistivities higher than 1.9×10^{-2} Ωm, it was found that this stabilising effect is negligible for the simulated cases. This value was therefore selected for the main comparison between the two modelling approaches.

During the nonlinear evolution, the resistivity needs to be linked to the plasma temperature in order for the vacuum region alone to remain highly resistive as the plasma boundary deforms in JOREK. In order to do this, the initial resistivity profile is converted into a function of the $n = 0$ temperature that is used in the time evolution through the nonlinear phase. This choice of resistivity is somewhat artificial, and only used in order to have a profile that approaches the ideal MHD assumptions in the VMEC result. In Section 3.4.2, simulations are also run with

Table 3.1: JOREK Parameters used in nonlinear MHD simulations of the external kink and edge harmonic oscillation discussed in Section 3.3 and 3.4, respectively. The diffusive parameters are the values defined at the plasma core.

Parameter	External Kink	EHO
T [keV]	$0.03 - 3.52$	$0.14 - 8.12$
n [$\times 10^{20}$]	$0.05 - 1.02$	$0.014 - 0.826$
$\kappa_{\parallel}$ [$\mathrm{kg \cdot m^{-1} \cdot s^{-1}}$]	4936.0	39386.0
$\kappa_{\perp}$ [$\mathrm{kg \cdot m^{-1} \cdot s^{-1}}$]	1.755	1.755
$D_{\perp}$ [$\mathrm{m^2 \cdot s^{-1}}$]	1.54	1.54
η [$\Omega \cdot \mathrm{m}$]	1.9382×10^{-7}	1.9382×10^{-7}
η_{num} [$\Omega \cdot \mathrm{m^3}$]	1.9382×10^{-12}	1.9382×10^{-12}
μ [$\mathrm{kg \cdot m^{-1} \cdot s^{-1}}$]	5.1594×10^{-7}	5.1594×10^{-7}
μ_{num} [$\mathrm{kg \cdot m \cdot s^{-1}}$]	5.1594×10^{-12}	5.1594×10^{-12}
n_{rad}	201 | 115	121
n_{pol}	121 | 151	151
n_{plane}	32	32

modified resistivity profiles, in order to determine the effect this can have on the dynamics.

The simulations in the following sections used the parameters shown in Table 3.1. Unlike in VMEC, a perfect vacuum, which has zero plasma density, is not assumed. Using the lower bound for the density and temperature shown in Table 3.1, numerical issues could be avoided sufficiently to run into the nonlinear phase. The diffusive parameters given are those assumed in the core of the plasma. For the parallel thermal conductivity, a Spitzer-Haerm dependence is assumed. A small amount of parallel particle diffusion is also used in the simulations to approximate the influence that the neglected parallel flow would have on the particle transport. For the perpendicular coefficients, a pedestal transport barrier is approximated by reducing the diffusivity coefficients near the plasma edge. Outside the plasma, the perpendicular diffusive coefficients are artificially increased to 10 times the core value, in order to keep the vacuum density and temperature relatively low in the axisymmetric state. This is necessary because a limiter geometry is used without modelling the target, so that there are closed magnetic flux surfaces outside the plasma in the simulation domain. For this reason, the parallel transport alone would not ensure reasonable vacuum conditions are maintained.

Regarding resolution, the number of radial, n_{rad}, and poloidal, n_{pol}, grid elements were chosen to resolve the dynamics. For the external kink case shown in Section 3.3, a non-flux aligned polar grid with 201 radial and 121 poloidal elements was used. The dominant low n modes which are simulated have large structures that are well resolved at this relatively high poloidal resolution. A flux aligned grid with 115 radial and 151 poloidal elements was used for the remaining simulations of the external kink, in order to converge the linearly unstable $n = 5$ mode that was

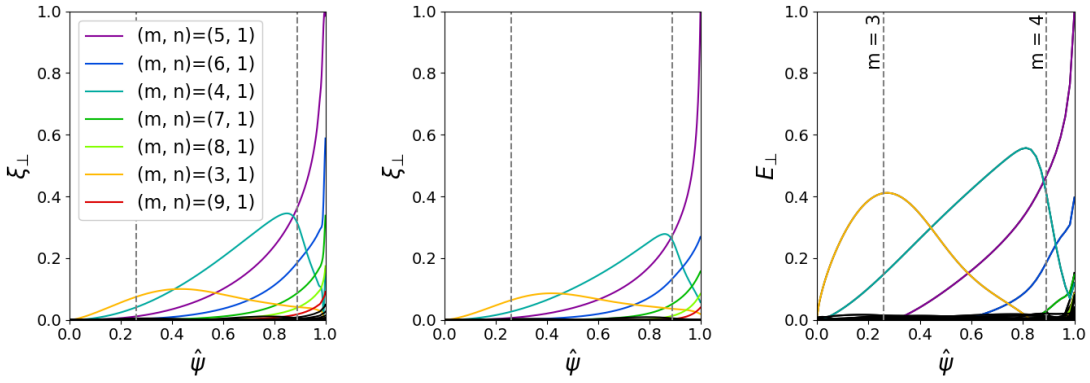

(a) (b) (c)

Figure 3.3: Comparison of radial eigenfunctions observed in JOREK during the linear phase (a), CASTOR3D (b), and the nonlinear perturbation observed in VMEC (c). The Fourier representation has been calculated using PEST coordinates.

found. For the EHO simulation, the grid is aligned to the initial equilibrium flux surfaces. The toroidal mode numbers $n = 0 - 5$ are simulated. 32 poloidal planes were used for both test cases, which is sufficient to resolve the representation of the toroidal harmonics.

3.3 Comparison with JOREK for the external kink case

3.3.1 Comparison of linear eigenfunctions

To begin with, it is important to confirm that the poloidal mode structure of the nonlinear displacement, $E_\perp$, in VMEC is qualitatively consistent with the perturbed displacement, $\xi_\perp$, from linear stability theory as described in Section 2.4.2. To this end, the linear eigenfunction observed in both JOREK and CASTOR3D are compared with the nonlinear Fourier representation of the perturbed displacement from VMEC, as shown in Figure 3.3.

The linear mode structure in JOREK and CASTOR3D shows good agreement across the plasma region, as expected. Comparing these linear eigenfunctions with the nonlinear displacement from VMEC, it can be seen that the structure of the internal (3, 1) contribution is peaked closer to the $q = 3$ surface. This strong peaking is thought to be because the (3, 1) mode has a larger nonlinear amplitude in the saturated state, than during the linear phase.

It should be noted that when comparing the nonlinear displacement found in the VMEC solution, with the perturbed displacement from linear theory, quantitative agreement is not expected. This is because $E_\perp$ does not have the same dependencies as $\xi_\perp$. For example, the nonlinear displacement is not dependent on the density,

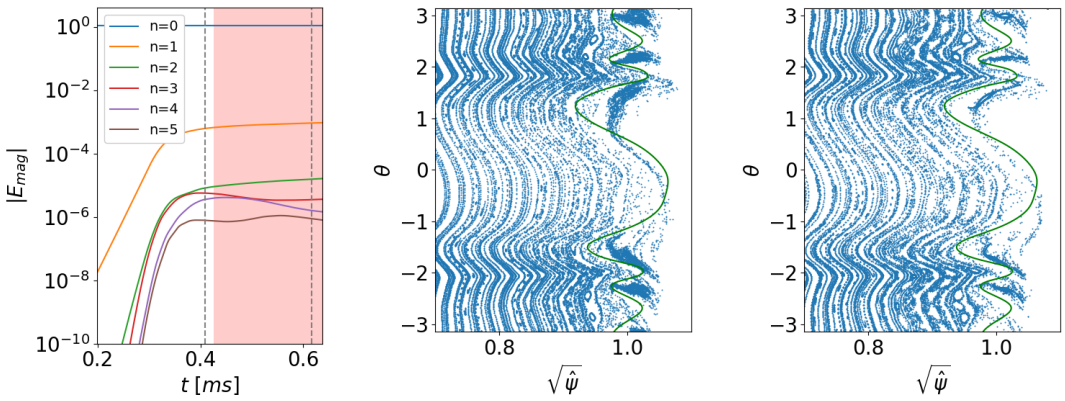

(a) (b) (c)

Figure 3.4: Magnetic energy evolution of the JOREK simulation during the nonlinear phase (a). Poincaré comparisons are made with the perturbed VMEC equilibrium at the initial saturation of the $n = 1$ mode (b) and near the end of the simulation run time (c). The times of the Poincaré plots are marked by grey dashed lines in Figure 3.4 (a). The poloidal magnetic energy spectrum computed in Figure 3.5 (a) is averaged over the region shaded in red. The last closed flux surface from VMEC (green) is overlaid on the Poincaré plots.

as it does not reflect the inertia of the plasma displacement. For this reason, the comparison is only meant to show that $E_\perp$ has a qualitative correspondence with $\xi_\perp$.

3.3.2 Comparison of flux surfaces and nonlinear magnetic energy spectrum

Beginning the nonlinear comparison of results in JOREK and VMEC, Poincaré plots generated at different points in the dynamics are compared against the converged flux surfaces from VMEC. The results in Figure 3.4 show reasonable agreement between the flux surfaces in JOREK and VMEC.

A final quantitative comparison is possible by comparing the magnetic energy spectra from the JOREK simulation with VMEC. The perturbed poloidal flux of the VMEC solution needs to be calculated in a similar representation as in JOREK for this comparison. The magnetic field of the perturbed VMEC solution is therefore re-calculated on a (R, Z, ϕ) grid, using EXTENDER to calculate the magnetic field produced by internal plasma currents beyond the plasma boundary. The axisymmetric vacuum magnetic field can be neglected in this calculation, because this study is only concerned with the $n > 0$ perturbed fields. The poloidal flux is then computed using

$$\int \frac{1}{R} \left(\nabla \Psi \cdot \nabla w\right) dA = \int w \left(\frac{\partial B_\mathrm{R}}{\partial Z} - \frac{\partial B_\mathrm{Z}}{\partial R}\right) dA. \tag{3.2}$$

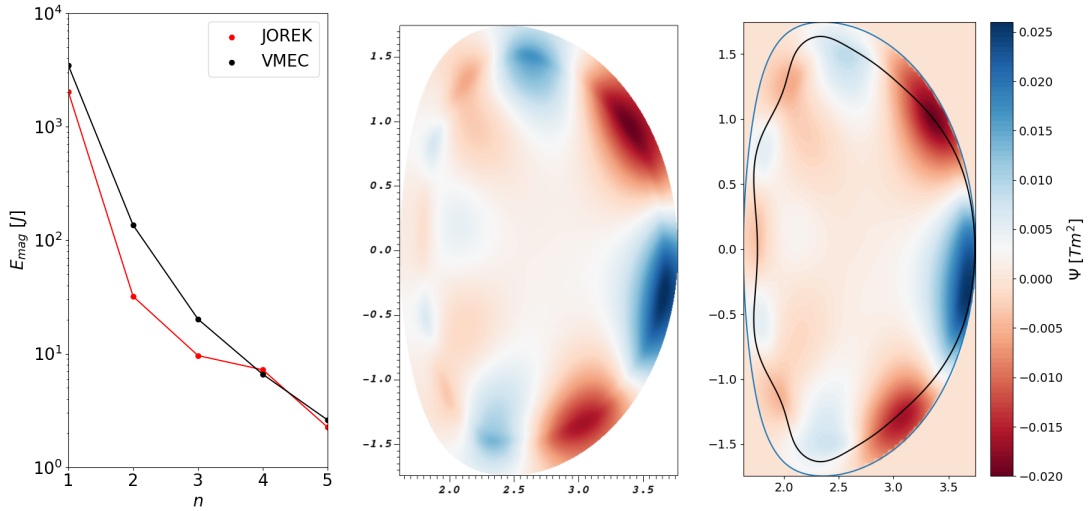

(a) (b) (c)

Figure 3.5: Comparison of perturbed magnetic energy spectrum in JOREK and VMEC solutions (a). The spectrum from JOREK is computed as the average over the red shaded region in Figure 3.4 (a). The perturbed poloidal flux in JOREK at the end of the simulation time (b) is compared with the VMEC solution (c) for a comparable poloidal plane. The simulation boundary used in JOREK (blue), and the last closed flux surface from the perturbed state (black) are also shown. Note that the same colour bar is used in both pseudocolour plots.

Equation 3.2 is written in the weak form, where w is the test function. The righthand side comes from substituting the magnetic field into the definition of $\Delta^*\Psi$ in equation 2.10. By taking a Fourier transform of the computed solution, the same representation of the magnetic field is obtained as in JOREK.

The magnetic energy spectrum of both representations, integrated over the computational domain in JOREK, is shown in Figure 3.5 (a). The two solutions for the saturated state have relatively similar magnetic energies. The local structure of the perturbed poloidal flux, omitting the $n = 0$ mode, in JOREK and VMEC is compared in Figure 3.5 (b) and (c) at the poloidal plane where the mode structures observed in the two codes are approximately in phase. It can be seen that there is good agreement between the two codes, and that the perturbation is strongly dominated by $(5, 1)$ and $(4, 1)$ mode structures.

3.4 Comparison with JOREK for edge harmonics oscillation

3.4.1 Comparison of linear eigenfunctions and mode structure

Similar to Section 3.3, an equivalent equilibrium to the unperturbed state from VMEC in Figure 3.2 is generated in JOREK. The linear perturbation observed in

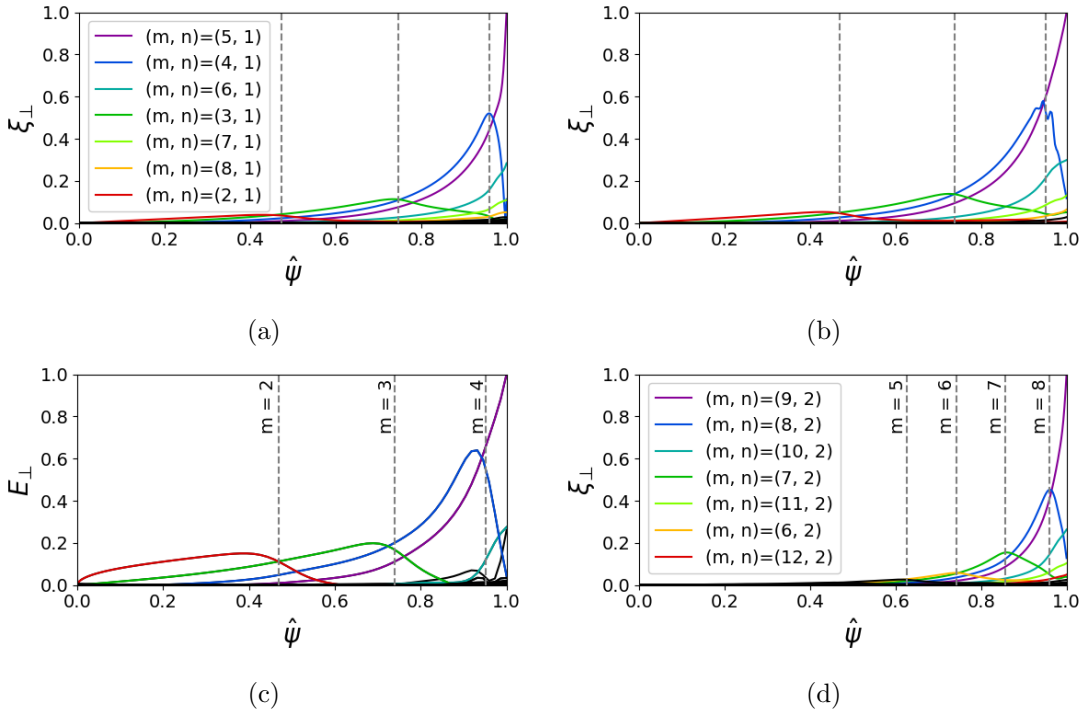

Figure 3.6: Comparison of the $n = 1$ radial eigenfunctions observed in JOREK (a) during the linear phase of the EHO test case, with the radial eigenfunction found in CASTOR3D (b), and the nonlinear perturbation observed in VMEC (c). The linear $n = 2$ mode observed in JOREK is also shown in (d). The Fourier representation has been calculated using PEST coordinates. The location of relevant rational surfaces with their corresponding poloidal mode number are marked by grey dashed lines.

JOREK is then compared with CASTOR3D, and the the nonlinear eigenfunction of the perturbed displacement amplitude in VMEC. The result of the comparison for the $n = 1$ instability is shown in Figure 3.6 (a-c). It can be seen that there is qualitative agreement once again between the different approaches. The typical strong (4, 1) internal contribution to the edge harmonic oscillation is observed in all codes.

The linear dynamics are immediately different to the case considered in Section 3.3, because the $n > 1$ toroidal harmonics are also unstable to linearly independent modes. As an example, the radial eigenfunction for the $n = 2$ mode is shown in Figure 3.6 (d). It can be seen that this mode has a similar structure to the $n = 1$ mode, with a large internal component localised at the $q = 4$ rational surface, and a dominant external component corresponding to the nearest rational surface to the plasma edge, $(nq + 1)/n$.

The linear mode structure of the exfernal modes that are observed in this equilibrium is shown in Figure 3.7 (b). For this case, the $n = 2$ and $n = 3$ toroidal

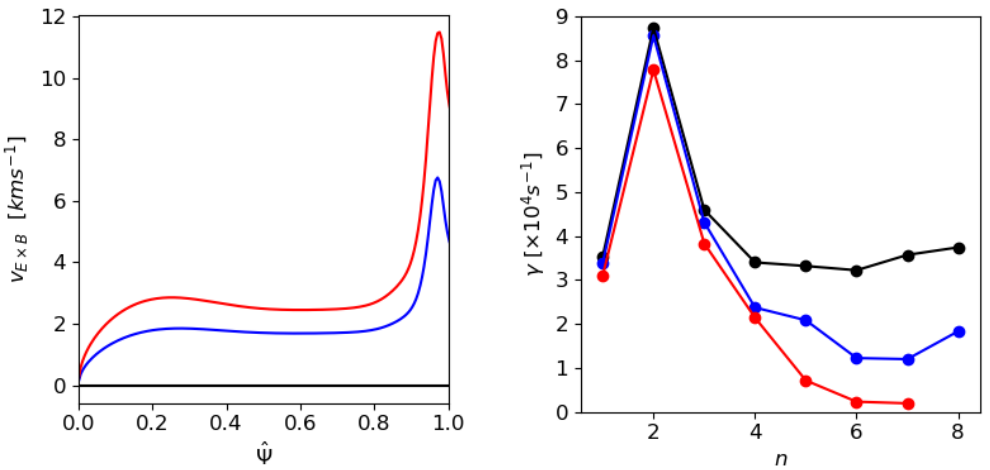

(a) (b)

Figure 3.7: Modification of the $\mathbf{E} \times \mathbf{B}$ velocity (a) with increasing diamagnetic source in JOREK. The red curves correspond to a value for the diamagnetic source in equation 2.34, which is close to the expected value for the modelled equilibrium. Results are also shown without flows (black) and at an intermediate value (blue) The linear growth rate of external modes up to $n = 8$ (b) show that high n modes are stabilised significantly when moderate flows are introduced. The results in this figure have used the resistivity profile from case 2 in Figure 3.8 (a).

harmonics have the largest linear growth rates. As shown in Section 3.4.2, they will therefore lead the initial nonlinear dynamics of the instability in JOREK simulations.

Before proceeding to nonlinear studies, the influence of toroidal and poloidal flows on the dynamics is explored. Equilibrium flows are an important area of research in the context of EHOs. It has been argued that flows play a crucial role in stabilising high n ballooning modes that would otherwise lead the linear dynamics. These ballooning modes can prevent low n kink modes from becoming the dominant nonlinear mode structure. Previous nonlinear studies have already observed the stabilisation of high n modes, and the excitation of low n external modes with increased toroidal and $\mathbf{E} \times \mathbf{B}$ flows [105, 107].

The diamagnetic source term in equation 2.34 was introduced to the EHO equilibrium to confirm that a similar stabilisation of high n modes with increased diamagnetic flows would be observed for the simulated EHO test case. Three equilibrium conditions were considered with increasing values of the diamagnetic source term. The corresponding $\mathbf{E} \times \mathbf{B}$ velocity within the plasma is shown in Figure 3.7 (a). The red curve in Figure 3.7 (a) is considered close to the expected $\mathbf{E} \times \mathbf{B}$ velocity that would be driven in the given equilibrium, however it should be acknowledged that the assumed source has not been informed by experimental observations. The

black curve corresponds to the case without a diamagnetic source, and is the assumed source used in the main simulations carried out in the subsequent nonlinear analysis. The blue curve is an intermediate value, between these two limits.

The modification of the linear growth rates in the no wall limit with increasing flows for $n <= 8$ is shown in Figure 3.7 (b). The expected preferential stabilisation of high n modes is observed, consistent with theoretical models of EHOs [104]. This analysis provides further evidence that low n modes can be expected to dominate the dynamics in an experiment for the given test configuration. In Figure 3.7, the low n modes were marginally stabilised by poloidal flows, unlike in previous studies of DIII-D [107]. However, for the simulated JET-like discharge, it is not clear that this effect should be observed. The inclusion of flows in the linear analysis of these modes serves to show that the dependency observed in JOREK is consistent with experimental and analytic results. In the following sections, the simulations without flows are continued into the nonlinear regime to compare with VMEC results.

3.4.2 Dependence of MHD dynamics on resistivity

The evolution of the magnetic energies for the EHO test case is shown in Figure 3.8. For this test case, parameter scans of the resistivity have been carried out. The test case was first simulated with the resistivity profile of case 1, shown in Figure 3.8 (a), which approximates the ideal MHD conditions in VMEC. As expected from the linear analysis in Section 3.4.1, the $n = 2$ EHO grows fastest, dominating the initial nonlinear dynamics and saturating on the fast ideal MHD timescale. The initial saturated state can be identified as a $n = 2$ EHO by the nature of the toroidal mode coupling, which includes only even toroidal mode numbers [105].

The sub-dominant $n = 1$, 3 and 5 modes continue to grow after the initial saturation of the $n = 2$ mode. The slow growth of the odd toroidal harmonics indicates that the nonlinear dynamics involve resistive effects. To verify this, a second simulation was run with the resistivity inside the plasma prescribed with a Spitzer-like dependence. In such a way, the resistive dynamics are accelerated, compared to case 1. As expected, the odd toroidal harmonics grow faster in this case, indicating resistivity is important in the nonlinear dynamics observed. To determine whether the $n = 1$ mode could dominate later in the nonlinear phase, case 2 is extended over a longer timescale. It can be seen that after approximately 3.5 ms, the $n = 1$ mode begins to suppress the initially prevailing $n = 2$ structures. This $n = 1$ saturated state is compared with the VMEC result in the following sections.

It is important to note the timescale of the MHD dynamics that are observed in the JOREK simulations. In Section 3.1.1, the solution of the VMEC computation was interpreted as the saturated state immediately after the fast phase of the instability, before resistive effects can become important. In the JOREK simulation, this fast phase ends after the saturation of the $n = 2$ mode, at $t \approx 1.3$ ms in case 1 and 2 of Figure 3.8. The expectation from the VMEC result is that the $n = 1$ mode would dominate on this timescale, which is not observed in the JOREK simulations. This leads to two important questions — why does the $n = 1$ mode not dominate

on the ideal timescale in JOREK simulations, and secondly, how much does the observed $n = 1$ mode correspond to the expected ideal EHO mode? The second question is addressed by considering the ergodisation of the plasma and perturbed magnetic energies in Section 3.4.3.

With respect to the first question, it is likely that the nonlinear influence of the $n = 2$ mode reduces the drive for the competing $n = 1$ mode for the simulated case. The rapid linear growth of the $n = 2$ mode, stabilises the $n = 1$ mode through quadratic coupling, as described in [108]. The ideal $n = 1$ mode must be stabilised by the $n = 2$ mode, because any deformation of the flux surfaces related to the odd toroidal mode numbers, which overlaps with the dominant $n = 2$ perturbation, must compete with this nonlinearly saturated mode structure. It can be seen in Figure 3.6 (a) and (d) that the linear perturbation associated with the $n = 1$ toroidal harmonic overlaps with the $n = 2$ perturbation. This implies that the nonlinearly saturated $n = 2$ EHO will have a stabilising influence on the linear $n = 1$ instability during its initial nonlinear saturation.

The sharp rise in the $n = 1$ energy during the initial saturation of the $n = 2$ mode implies that the $n = 1$ mode structure is strongly influenced, as it is forced to accommodate the $n = 2$ EHO. After this point, the deformation of the plasma leads to thermal losses that increase the resistivity inside the plasma and reduce it in the vacuum region. The pressure gradient driving the mode in the plasma edge region also relaxes. The saturated $n = 2$ mode also influences the evolution of the $n = 1$ mode through these effects, leading to the slower timescale to saturation of the $n = 1$ mode. While the observed dynamics in JOREK are physically reasonable, the timescale means that these results cannot be used to rigorously verify the VMEC result, which neglects viscoresistive and diffusive effects. In this limit, the dynamics could be different.

A final simulation, case 3, was run with a more realistic Spitzer resistivity inside, and outside the plasma. This simulation serves to highlight the difficulty in predicting the nonlinear outcome of an EHO, because of the strong dependence of the initial dynamics on the assumed resistivity profile. The lower resistivity in the vacuum region has a stabilising effect on the initial ideal MHD instabilities, which brings the ideal and resistive timescales closer together compared to case 1 and 2. The evolution of the magnetic energies is shown in Figure 3.8 (d). It can be seen that for this case, all linearly unstable modes have been partially stabilised, and the $n = 3$ mode leads the dynamics, before quickly being overtaken by the $n = 2$ mode. After this point, there is a period of competition between the $n = 1$ and $n = 2$ modes, before the $n = 2$ mode becomes the principal mode. The $n = 1 - 3$ modes that dominate the perturbation at different points in the dynamics are all kink-peeling modes, such that the linear dynamics are similar to the simulation results for case 1 and 2. The nonlinearly saturated state at the end of the simulation time has changed due to the modification of the resistivity in the vacuum region, highlighting the sensitivity of the nonlinearly dominant mode on this parameter.

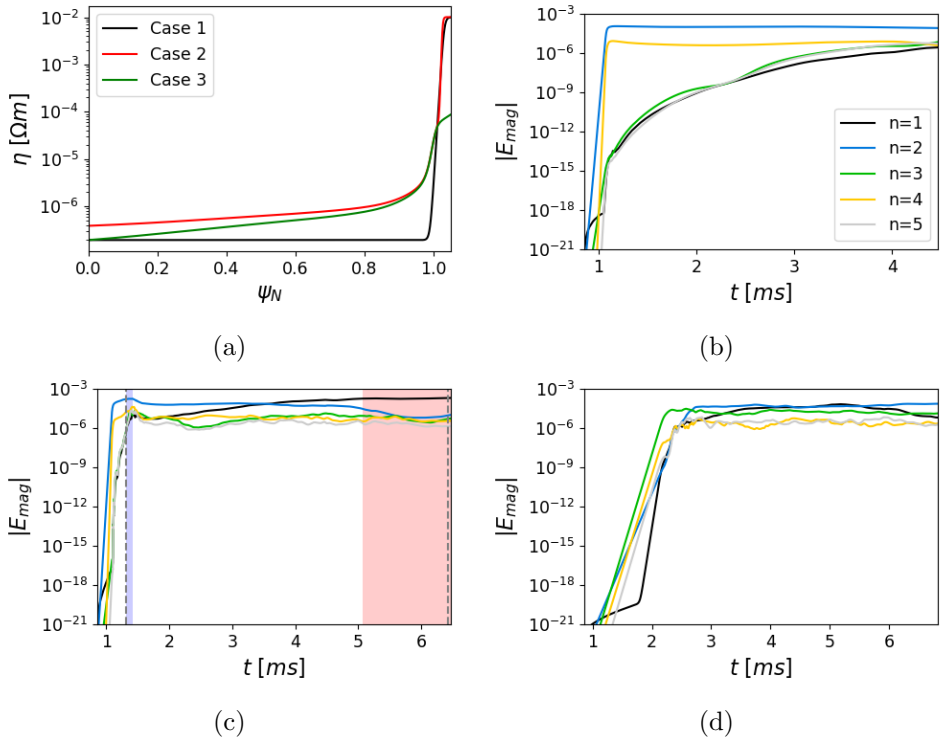

Figure 3.8: Toroidal magnetic energies from JOREK for the EHO test case simulated with different resistivity profiles (a). Note that the energies are normalised by a factor μ_0. A larger core resistivity compared to case 1 (b) is used in case 2 (c) to accelerate the onset of resistive effects. The time points marked by grey dashed lines correspond to the Poincaré plots shown in Figure 3.9, and pseudocolour plots in Figure 3.11 (b) and (c). The coloured regions correspond to the simulation time over which the energy spectrum is averaged over in Figure 3.11 (a). A Spitzer resistivity is used in case 3 (d).

3.4.3 Comparison of flux surfaces and perturbed magnetic energies

The modification of the magnetic geometry and confinement can be used to understand the differences between the nonlinearly perturbed state found in case 2 and the ideal VMEC result. The Poincaré plots in Figure 3.9 are taken at the saturation of the $n = 2$ and $n = 1$ mode. The $n = 2$ mode initially saturates with a dominant (9, 2) perturbation of the poloidal flux. The corresponding island chain can be identified in Figure 3.9 (a), but is faint due to the significant stochastisation in the edge region. Later in the dynamics, when the $n = 1$ mode is dominant, a (5, 1) island chain is observed outside the plasma, as shown in Figure 3.9 (b). The observed magnetic island structure and the approximate structure of the last closed flux surface from the equivalent VMEC computation, shown in green, are in reasonable agreement. The internal flux surfaces in VMEC are replaced by a strongly ergodic region with clearly visible (4, 1) magnetic islands in the region

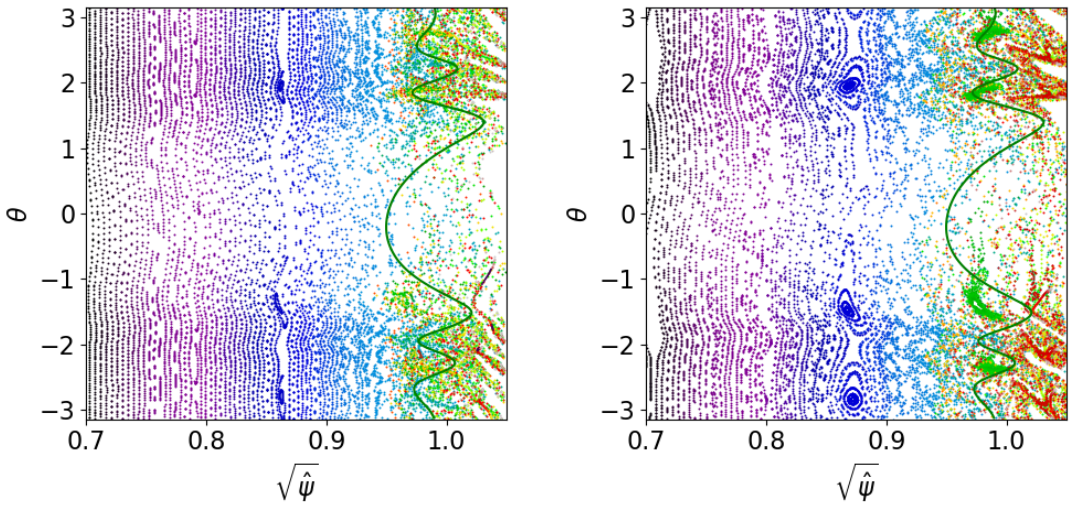

(a) (b)

Figure 3.9: Poincaré comparisons are made with the perturbed VMEC equilibrium at two time points in the nonlinear evolution of case 2. The time points are marked by grey dashed lines in Figure 3.8 (c). Each field line is given a different colour to identify the island structures more easily in ergodic regions. At the initial saturation of the $n = 2$ harmonic, a (9, 2) island structure is identified at the plasma edge (a). At the end of the simulation, (5, 1) and (4, 1) island structures become dominant (b). The last closed flux surface from VMEC (green) is overlaid on the Poincaré plots.

near the plasma boundary.

The connection length of magnetic field lines to the simulation boundary can be used to assess how these internal structures change the parallel transport. This diagnostic is shown in Figure 3.10. The connection length is calculated using the harmonic mean of 1000 sample field lines uniformly distributed along the poloidal angle of the $n = 0$ flux surfaces. The radial coordinate is taken to be the square root of the $n = 0$ component of the normalised poloidal flux. The results are normalised by the maximum distance traced. It can be seen that across the majority of the plasma region, field lines remain well confined within the plasma volume. There is only a significant loss of field lines near the plasma edge. Similar results have been observed in more realistic studies of EHOs in DIII-D using x-point geometry [109].

Similar to Section 3.3, the magnetic energy spectrum has also been calculated and compared between the two codes, as shown in Figure 3.11 (a). The energy spectra in JOREK are taken during the initial saturation of the $n = 2$ mode, and final saturation of the $n = 1$ mode for comparison. For the final $n = 1$ dominated state, it can be seen that while the low n modes agree reasonably well, the high n modes are notably larger in JOREK. The flat spectra observed in the JOREK energies is typically seen when there is MHD activity in the higher n modes which

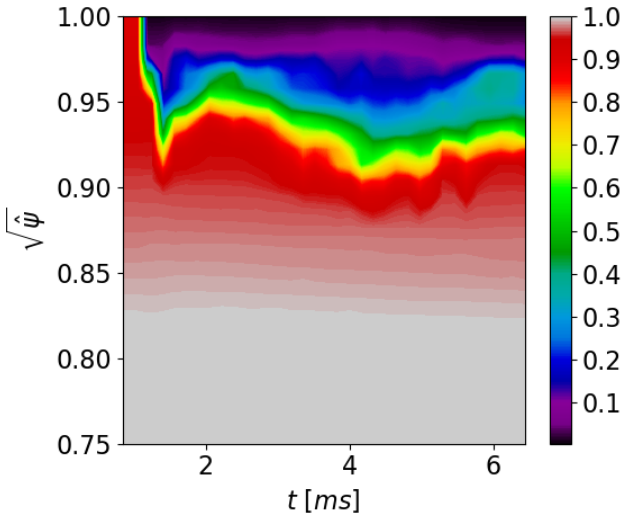

Figure 3.10: Average connection length of field lines to the JOREK simulation boundary as a function of time for case 2. Note that the results are normalised by the maximum distance traced, which is in the plasma core.

is not driven by the lower toroidal harmonics. This behaviour is also observed later in this thesis in Chapter 6, when studying the change in the nonlinear saturation of external kink modes with reduced plasma current. It will be shown in Figure 6.5 of this separate study that the magnetic energy spectrum remains broad when multiple toroidal harmonics are linearly unstable or nonlinearly triggered. In other words, for the EHO case that is considered in this study, the magnetic energy spectrum in Figure 3.11 (a) is broad because the higher toroidal harmonics are linearly unstable in JOREK, as shown by the linear mode structure in Figure 3.7. The decay of the energies seen in the VMEC spectrum is typical for an instability which is driven by the $n = 1$ mode alone, implying that the high n modes observed in JOREK are suppressed.

The perturbation of the poloidal flux from JOREK is shown at the time of saturation for the $n = 2$ mode in Figure 3.11 (b). This shows that the instability is initially led by a (9, 2) external structure, as expected from the linear eigenfunction observed in Figure 3.6 (d). Near the end of the simulation time, shown in Figure 3.11 (c), the poloidal flux perturbation looks very similar to the stationary perturbation in VMEC. This indicates that the resistive dynamics have not changed the overall structure of the mode from the ideal result.

The question remains, why does the energy spectrum differ in Figure 3.11 (a)? The connection length diagnostic shows that the overall mode structure has strong similarities to previous observations of EHOs, and the poloidal flux perturbation is very similar to the VMEC result. It seems that the instability observed in the two codes has strong similarities, despite the discrepancy in the energies of higher

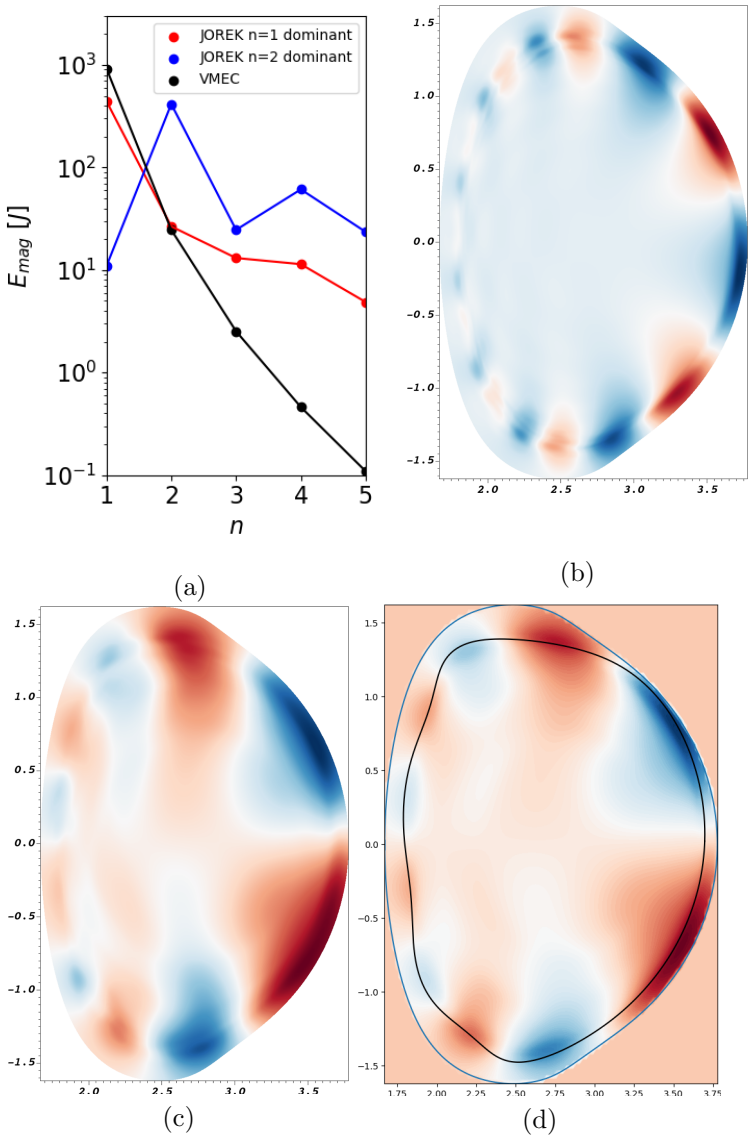

Figure 3.11: Comparison of the perturbed magnetic energy spectrum in JOREK and VMEC (a). The energy spectra during the $n = 2$ dominant phase (blue), and the final $n = 1$ dominant mode (red), corresponding to the blue and red regions in Figure 3.8 (c), are shown. The perturbed poloidal flux in JOREK during the initial saturation of the $n = 2$ mode (b) and at the end of the simulation time (c) is plotted for the time slices marked by grey dashed lines in Figure 3.8 (c). A comparable poloidal plane from the VMEC solution (d) is shown with the JOREK simulation boundary (blue), and the plasma boundary from the perturbed state in VMEC (black). The colour bars are not the same in the three pseudocolour plots, so that the poloidal structures can be more easily compared with one another.

toroidal harmonics. As a result, it appears that the VMEC solution does not capture the full toroidal mode coupling of the instability, represented by the sub-dominant modes in Figure 3.11 (a). This could be because of the assumption of nested flux surfaces in VMEC, which prevents the ergodisation of the edge region observed in JOREK, as shown in Figure 3.9.

3.5 Discussion

In this chapter, nonlinear MHD simulations have been compared with saturated free boundary MHD perturbations in VMEC for external modes. For the considered external kink case, where the initial unperturbed equilibrium is unstable to a single dominant linear perturbation, the agreement between the two approaches is reasonable. For the more complex dynamics observed in the EHO test case, where several competing toroidal mode numbers feature in the dynamics, the dominant perturbation observed in the two codes can differ. Because the $n = 2$ toroidal mode number is significantly more unstable than the $n = 1$ mode, the $n = 1$ mode is found to only dominate on a resistive timescale. Comparing the structure of this resistive perturbation with the $n = 1$ mode observed in VMEC, the mode structure remain in reasonable agreement, in terms of the dominant poloidal flux perturbation. The JOREK results show signs of stronger toroidal mode coupling, which is likely suppressed in VMEC due to the assumption of closed flux surfaces, which prevents the plasma ergodisation in the edge region observed in JOREK. The main nonlinear JOREK simulations presented in this study were run without diamagnetic flows, in order to have similar stationary equilibrium conditions as are assumed in VMEC. The linearly unstable high n modes seem to lead to deviations between the JOREK and VMEC simulation results. In such a way, it is expected that including flows, which suppress these high n modes, could improve the agreement in Figure 3.11 (a). In addition, equilibrium codes such as SPEC [57] or SIESTA [110] relax the assumption of nest closed flux surfaces. It would therefore be interesting to see if the magnetic energy spectrum observed in such codes recovers the high n spectral content observed in JOREK through ergodisation of the plasma edge region. Such a study is a possible direction for future work.

The results show that a reasonable link can be drawn between the two modelling approaches, even for advanced test cases. This is not to say that the results should agree well in general. Experimentally, similar ideal external modes can nonlinearly trigger resistive core MHD instabilities [29], which VMEC is not expected to capture. In such cases, a stronger deviation in the dynamics can be expected. In addition, caution needs to be taken when multiple competing modes are observed in the linear analysis of the perturbation, but even in these cases, the results from VMEC clearly have a correspondence with the results from a full time evolving approach. For this reason, it was considered reasonable to use the approach in VMEC to provide an initial assessment of external modes in stellarators, as considered in the next chapter.

4 Applying VMEC to model nonlinear MHD activity in stellarators

The assessment of free boundary equilibrium approaches for the study of nonlinear MHD is continued in this chapter. The studies of external modes in Chapter 3 are extended to consider stellarator equilibria. As there are only a few studies which have attempted to use VMEC for modelling MHD activity in stellarators, this work considers classical stellarators as a first step, with the purpose of understanding the behaviour of VMEC, and characterising the nonlinear states obtained in such simple geometries. By scanning the ellipticity, and current profile, a parameter space is defined in which to search for nonlinearly saturated states in Section 4.1. It is found that (4, 1) external kink modes can be converged with ι preserving computations for cubic current profiles. In Section 4.2, resolution scans are used to show that the saturated state is not well defined by enforcing the conservation of helicity alone. To resolve this problem, an additional constraint on the observed plasma current spike is enforced to define the appropriate resolution parameters to use.

Parameter scans of the edge safety factor and external rotational transform are then performed in Section 4.3. While saturated states can be found where the nonlinear perturbation amplitude is correlated with the linear growth rate observed using linear MHD codes, additional perturbed equilibria have been found which contradict this trend. It is argued that the latter perturbed equilibria are bifurcated states that do not correspond to the MHD dynamics. The nonlinear energy spectrum of the modes is then considered in Section 4.4, showing that the perturbation in classical stellarators have dominant contributions from the toroidal harmonics that belong to the $N_\mathrm{f} = 1$ mode family. It is argued, using free boundary JOREK simulations, that the increase in the $n = 0$ poloidal magnetic energy could be caused by a modification of the energy distribution in the vacuum region due to the plasma current spike. A preliminary comparison of VMEC results with JOREK stellarator simulations shows that the dominant poloidal mode structures in the $l = 2$, $N_\mathrm{p} = 2$ stellarator are consistent in both codes, cross validating the modelling approaches. These initial results are intended to be further developed for publication, and are a first step towards future studies considering external modes in optimised devices.

4.1 Parameter space for nonlinear studies

As discussed in Section 2.3.2, it is not clear that an ideal MHD unstable equilibrium will necessarily converge to a saturated state. In this section, the parameter space for VMEC studies is narrowed down by searching for a region where saturated states can be robustly converged. As classical stellarators are of interest, the modelled stellarators are all in the $\beta \approx 0$, high aspect ratio, $A = R_0/r_{\text{minor}} \approx 10$, limit.

To begin with, scans of the ellipticity, $\kappa = b/a$, where b is radius along the semi-major axis, and a is the radius along the semi-minor axis, and the initial current profile are considered to narrow down the parameter space. The toroidal current profiles are set to be parabolic of the form

$$j(s) = 1 - s^p, \tag{4.1}$$

where p is an integer constant. Note that, as discussed in Section 2.3.3, the ι profile is kept fixed during the equilibrium computation. Scans of $1.0 <= \kappa <= 1.5$ and $2 <= p <= 4$ were carried out. Results for the scan using $p = 3$ are shown in Figure 4.1. With reduced κ and increased p, convergence becomes more difficult. This is expected as the edge current density gradient increases with p, making the perturbation more violent, and the magnetic shear at the plasma edge decreases with κ, as shown in Figure 4.1 (a), such that the instability becomes more global. The perturbation is therefore harder to converge.

As it is intended to model classical stellarators in this study, the unperturbed equilibria would ideally have a circular plasma cross section. Such equilibria could not be converged within the considered parameter space, however. A small amount of vertical shaping, $\kappa \geq 1.25$, was found to be necessary in order to converge the perturbed equilibrium state, using $m = 15$ and $n = 6$ as the maximum poloidal and toroidal mode numbers in the computation. It is thought that this is because the equilibria at lower ellipticity are linearly more unstable. This is shown by the growth rates, $\hat{\gamma}$, shown in Figure 4.1 (b), where $\hat{\gamma}$ has been normalised by the volume averaged magnetic field strength of the equilibrium. The normalised amplitude of the (4, 1) component of the perturbed displacement of the plasma boundary, $\hat{\eta}_{\text{n=1, m=4}}$, where the displacement has been normalised by the minor radius, is also shown in Figure 4.1 (b). For this reason, all further parameter scans set $\kappa = 1.25$ and $p = 3$, varying q_{edge} and ι_{ext}.

4.2 Convergence scans

Before proceeding to scans of the physical parameters, q_{edge} and ι_{ext}, it is important to understand the convergence properties of the perturbed equilibria that are being considered. In previous studies of RMPs [63], it was found that computations of tokamak plasmas do not converge with increasing poloidal resolution due to the high resolution required in order to resolve the resonant poloidal mode number at the edge. A similar observation is made in this study, as shown in Figure 4.2.

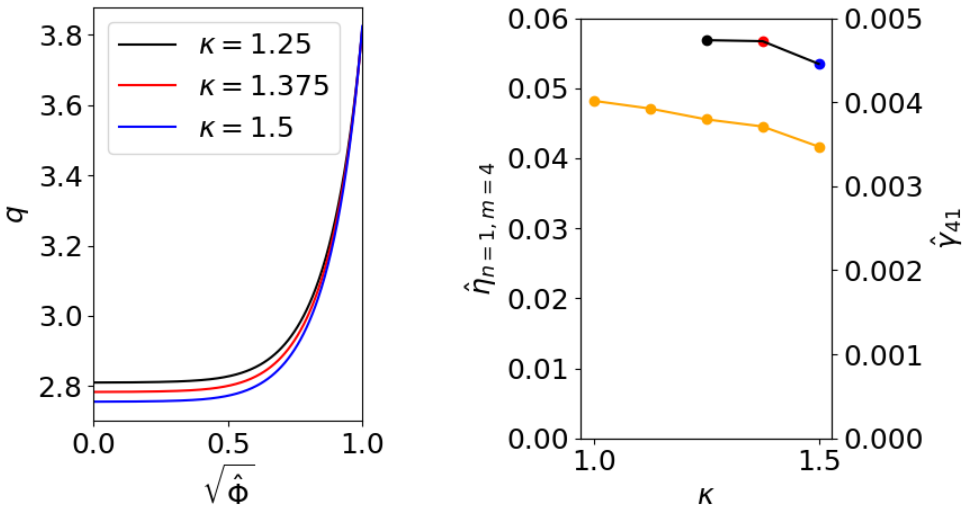

(a) (b)

Figure 4.1: Parameter scan of the ellipticity, κ, for tokamak cases with $q_{\text{edge}} = 3.85$, and $p = 3$. The shear of the q profile (a) increases with κ. The normalised nonlinear displacement amplitude (black, left y-axis) and linear growth rates (orange, right y-axis) are shown in (b). Nonlinearly saturated states can only be found for $\kappa >= 1.25$.

While the displacement of the plasma boundary is converged at reasonable radial resolution, N_{s}, the result is not converged in the poloidal resolution for any of the simulated cases. The implied contributions to the saturated mode structure from the higher poloidal harmonics is plausible, given that $m = 4n$ modes are required to resolve the resonant poloidal mode of a given toroidal mode number for the modeled (4, 1) dominant instability. In addition to this observation, the toroidal resolution requirement increases with N_{p}, such that edge displacements are harder to converge for the $N_{\text{p}} = 5$ case. This is likely due to higher toroidal components of the mode as a result of the mode coupling produced by the $n > 0$ components of the background vacuum magnetic field. It should be noted that, unlike the boundary representation itself, the plasma boundary deformation can be represented well by a single Fourier component, $\hat{\eta}_{\text{n=1, m=4}}$, because the Fourier representation is taken in straight field line coordinates.

The above observations present a challenge to the use of this approach for physics studies — all of the above equilibria are valid perturbed equilibrium states that could correspond to a saturated ideal MHD mode, so how does one determine the numerical resolution which is most representative of the true saturated state produced by the ideal MHD dynamics? Following the discussion in Section 2.3.3, it should be possible to identify the relevant saturated state by enforcing additional physical constraints on the MHD dynamics. In this work, constraints on the evo-

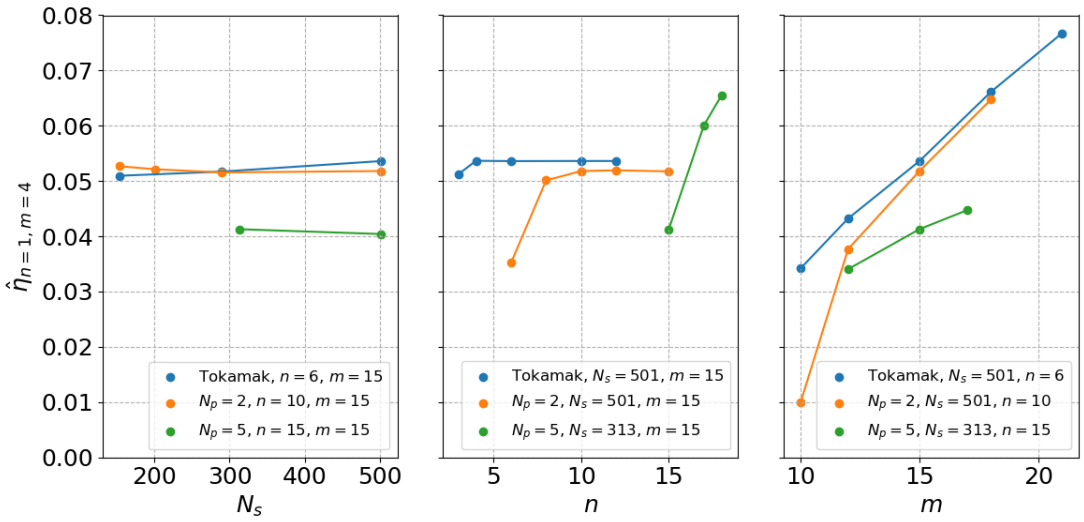

Figure 4.2: Resolutions scans for the normalised boundary displacement as a function of radial resolution, N_s, and maximum toroidal, n, and poloidal, m, mode numbers in the flux surface representation (left to right). Results are shown for tokamak (blue), $N_\mathrm{p} = 2$ (orange) and $N_\mathrm{p} = 5$ (green) stellarator cases with $q_\mathrm{edge} = 3.9$. The stellarator cases both have $\iota_\mathrm{ext} \approx 0.1$.

lution of the plasma current are explored.

The convergence of the toroidal plasma current density with radial and poloidal resolution is shown in Figure 4.3 and Figure 4.4. Convergence difficulties were encountered for free boundary equilibria with $N_\mathrm{s} > 501$ using reasonable computational resources, and so this is the limit for the radial resolution used for the initial free boundary convergence scan shown in Figure 4.2. It can be seen in Figure 4.3 (a) that the plasma current at the plasma boundary, $\hat{\Phi} = 1$, does not converge with increasing radial resolution, even though the plasma boundary itself is not modified significantly by increasing the radial resolution. A similar observation was once again observed in [63]. The response to the plasma deformation in this region is similar to the shielding of magnetic islands that has been observed in previous studies, which has been shown to have significant resolution requirements in VMEC [111]. However, for the main metric of interest in this study — the deformation of the plasma — convergence in the radial resolution is easily achieved.

At the same time, however, when the converged solutions from Figure 4.2 are restarted, keeping the final perturbed boundary fixed, and using a higher radial resolution, numerical structures can be observed in the equilibrium solutions. A comparison of the original free boundary solution with the fixed boundary computations is shown in Figure 4.4. The perturbed plasma boundary is fixed, and the computation is repeated with increased radial resolution at $N_\mathrm{s} = 2001$. It can be seen that as the poloidal resolution is increased, the enhanced radial resolution re-

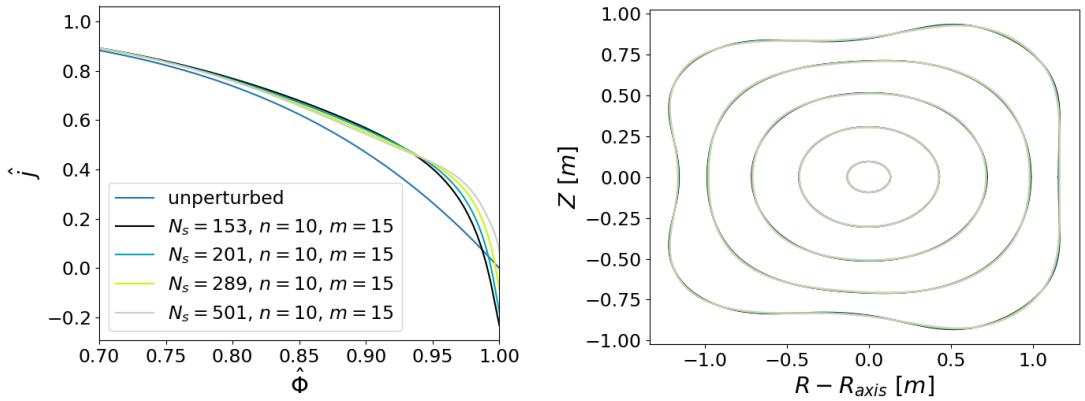

(a) (b)

Figure 4.3: Variation of the toroidal current density profile (a) and plasma flux surfaces (b) with increasing radial resolution, N_s, for $N_p = 2$ stellarator case with $q_{edge} = 3.9$ and $\iota_{edge} \approx 0.1$. The radial resolution strongly affects the plasma current profile, while the plasma displacement is almost identical for all considered resolutions.

veals a localised current sheet at the plasma boundary. Using $m = 15$, this current sheet could only be converged to $f_{tol} = 10^{-12}$. Further, in Figure 4.4 (b), numerical oscillations are observed in the plasma core. These numerical features, which worsen with increased poloidal mode number could indicate that the use of a lower poloidal resolution, around $m = 10$ for the tokamak case, where the toroidal current profile is not modified significantly with increased N_s would produce more physical results. While this approach to constraining the equilibria could be promising, it is currently not clear at what point the current sheets should be considered numerical. A recent study has considered this question in Cartesian geometry [112], but there is still not a clear answer to resolve the problem, and so this approach to constraining the solution was not pursued further in this initial study.

Alternatively, one might consider applying an additional physical constraint on the VMEC equilibrium to define the appropriate resolution. In [63], where fixed current VMEC computations were performed, such that q_{edge} could be modified, an additional physical constraint was used to define the numerical parameters, namely a constant edge safety factor between the unperturbed and perturbed solutions. This constraint is already enforced in ι preserving computations, and therefore a constraint is imposed on the current profile here instead. An alternative constraint to identify more realistic solutions could be to ensure that the observed current spike between the perturbed and unperturbed solutions is reasonable in magnitude. For studies which compare to an experiment, prior knowledge of the current spike can be used to inform the resolution requirements. Unfortunately for this study, there is no corresponding experiment to compare against, and so it is unclear what the expected current spike should be. For this reason, it is assumed that at $q_{edge} = 3.9$,

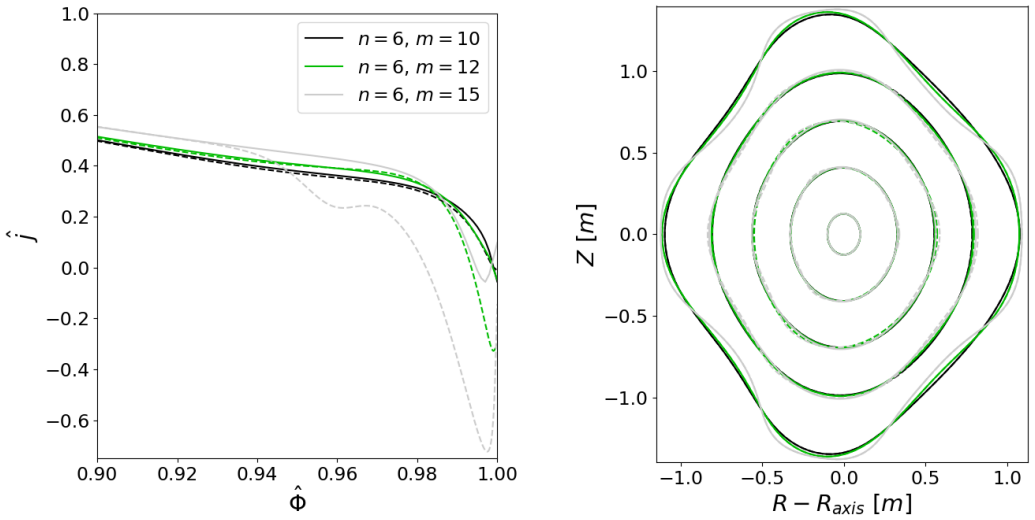

(a) (b)

Figure 4.4: Variation of the toroidal current density profile at the plasma edge (a) for perturbed tokamak equilibria with $q_{\text{edge}} = 3.9$, using different poloidal resolutions. The radial resolution is increased from $N_{\text{s}} = 501$ (solid) to $N_{\text{s}} = 2001$ (dashed) with the plasma boundary kept the same. At high poloidal resolution, numerical variations of the edge current and internal flux surfaces (b) can be observed. Note that the $N_{\text{s}} = 2001$ computations are only converged to $f_{\text{tol}} = 10^{-12}$ and the $m = 15$ computation only converged to $f_{\text{tol}} = 2 \times 10^{-12}$.

a current spike on the order of 5 % would be reasonable.

The variation of the plasma current spike observed in resolution scans is shown in Figure 4.5. It can be seen that the current spike remains below 5 % for the tokamak and $N_{\text{p}} = 2$ case when $m <= 15$. For this reason, the results in Section 4.3 use this value. The radial resolution, $N_{\text{s}} \approx 300$, is used in all cases, and the toroidal resolution is varied from $n = 6$ for the tokamak case, to $n = 15$ in the $N_{\text{p}} = 5$ stellarator case. Based on the results in Figure 4.5, it seems that the $N_{\text{p}} = 5$ case will be under resolved. Higher resolution simulations were attempted but were not tractable due to high computational cost, and convergence difficulties.

4.3 Correlation of nonlinearly saturated mode amplitude with linear growth rates

The saturated behaviour of the external kink is compared with the expectation given by linear theory for circular tokamak plasmas. It is expected that the external kink amplitude should increase with the linear growth rate. For the simulated tokamak cases, this behaviour is observed, as shown in Figure 4.6. Similar results have been observed in [71]. In addition, the observed plasma current spike is shown

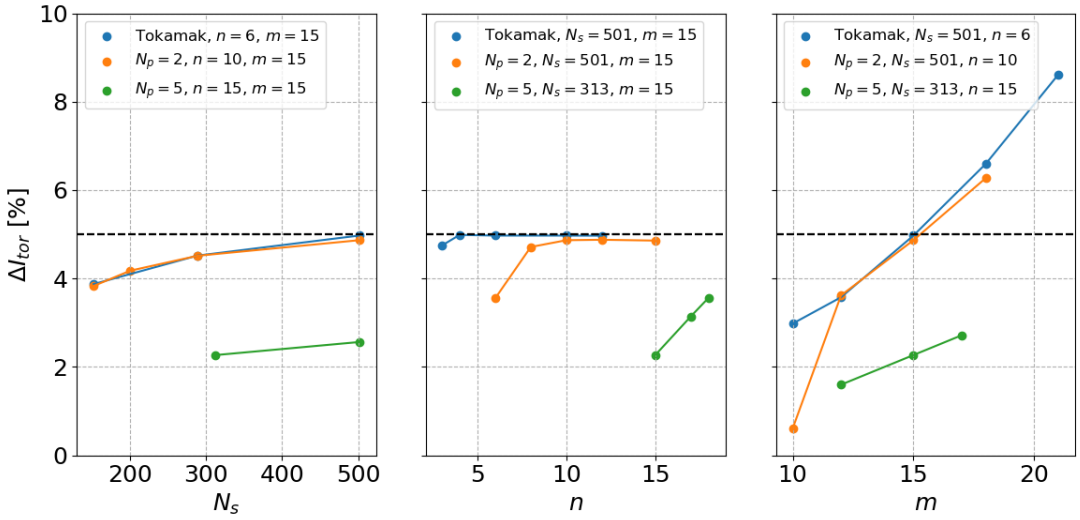

Figure 4.5: Resolution scans for the plasma current as a function of radial resolution N_s, maximum toroidal mode number n, and maximum poloidal mode number m (left to right). Similar to Figure 4.2, the plasma current spike does does not converge with increasing poloidal resolution.

in Figure 4.6 (d). It can be seen that the spike in current varies up to approximately 8 %, which is considered comparable to current spikes observed in other simulations of violent MHD dynamics [113, 114]. Given that the modelled kink saturates, the current spike may be an overestimate, however this cannot be confirmed without an experimental comparison, and the trend is considered reasonable enough to continue with this exploratory study.

It should be noted that the external kink could not be observed in either VMEC or CASTOR3D at $q_\mathrm{edge} = 3.55$. Below this value, only a resistive, internal (3, 1) tearing mode was observed in linear scans with CASTOR3D. This shows that the perturbed states have only been observed within the identified window of linear instability, which supports the notion that they correspond to physical perturbations of the initial equilibrium state.

For the simulated tokamak cases, the nonlinear displacement can be seen to vary most in proximity to $q_\mathrm{edge} = 3.9$. This point was therefore chosen for further scans of $l = 2$ stellarators with $N_\mathrm{p} = 2$ and $N_\mathrm{p} = 5$. The nonlinear displacement of these cases is plotted as a function of the external rotational transform at the unperturbed plasma axis, $R = 10$, in Figure 4.7 and 4.8.

For the $N_\mathrm{p} = 2$ case, computations are carried out using $n = 6$ and $n = 10$ producing different physical trends. For $n = 6$, it can be seen that the saturated perturbed amplitude continues to decrease, such that the external rotational transform appears to have a stabilising influence on the nonlinear dynamics of the external kink. For $n = 10$, the mode amplitude unexpectedly grows with the frac-

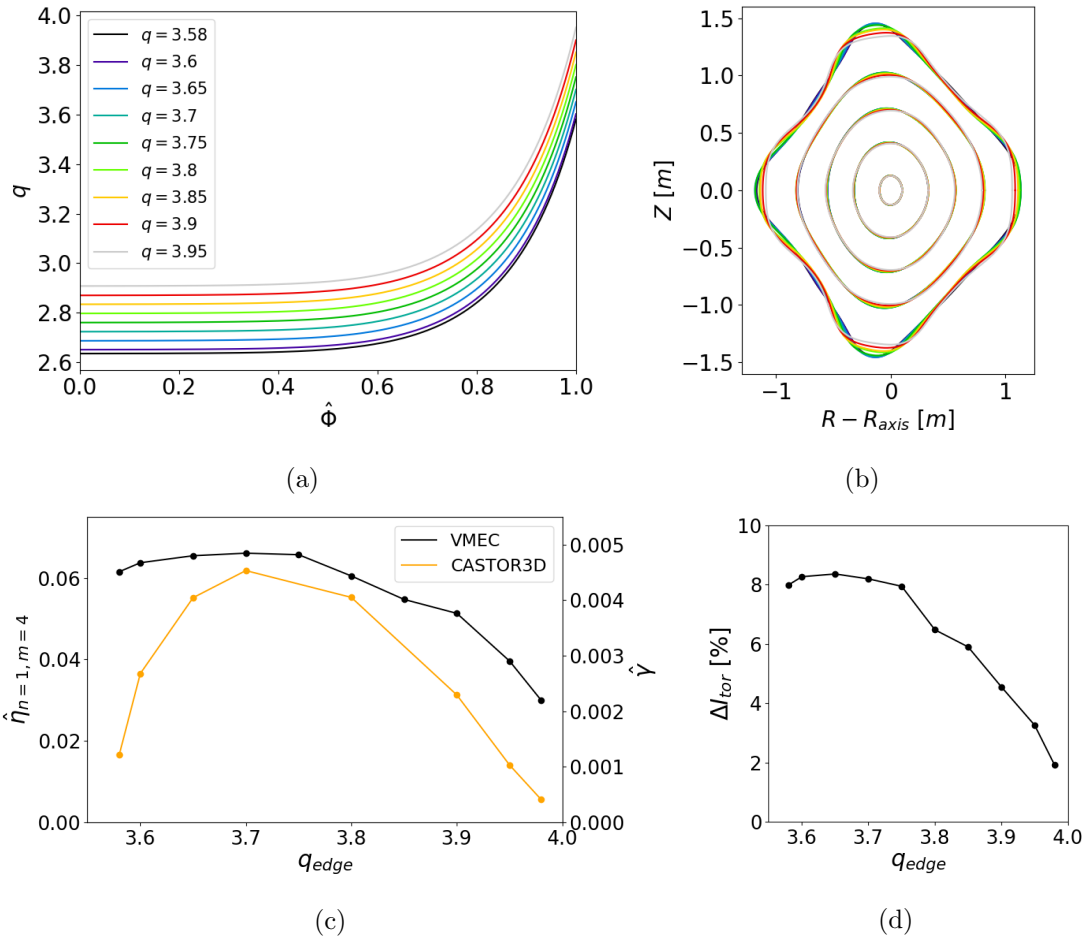

Figure 4.6: The q profile (a) and perturbed surfaces in the $\phi = 0$ plane (b) of tokamak cases. In (c), the perturbation amplitude (black, left y-axis) approximately follows the structure of the linear growth rate (orange, right y-axis). The plasma current spike (d) ranges up to 8 %.

tion of external rotational transform. It is currently unclear which of these two solutions is physical. The trends in the linear growth rates should indicate that the saturated mode amplitude will decrease, if the dependencies of the nonlinearly saturated mode amplitude in simple stellarators is the same as has been derived for tokamaks, however this has not been shown rigorously [87]. Further, the parameter scan that is explored in this study is essentially one where the toroidal plasma current is decreased, relative to the applied external field. For increasing ι_{ext}, the effective plasma current should tend to zero, such that the drive for instability is removed. For this reason, the $n = 6$ case is currently considered a physical solution, while the $n = 10$ is a bifurcated state.

A similar scan was carried out for $N_{\text{p}} = 5$ stellarators. With increasing ι_{ext} only a stabilising trend was found, however in this case the toroidal resolution was $n = 15$,

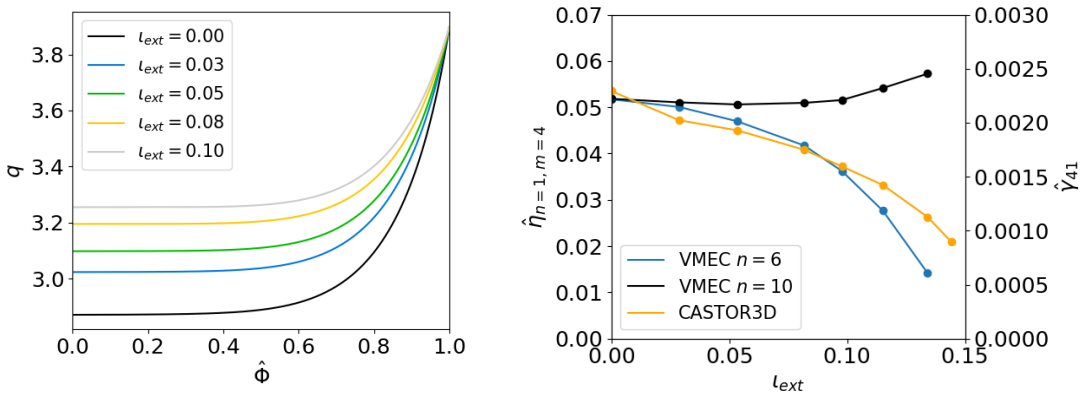

(a) (b)

Figure 4.7: Modification of the q profile (a) with increasing ι_{ext} for $l = 2$ $N_{\text{p}} = 2$ stellarators. The behaviour of the nonlinearly saturated perturbation amplitude (left y-axis) with increasing ι_{ext} depends on the maximum toroidal mode number used in the computation. The results with $n = 6$ (blue) are considered more physical than with $n = 10$ (black), as the behaviour is correlated with the change in the linear growth rate (orange, right y-axis).

which is shown to be underresolved from Figure 4.2. If a higher resolution that is toroidally resolved were used, it may have been possible to recover similar larger amplitude perturbed states to those observed when using $N_{\text{p}} = 2$. Unfortunately, higher resolutions were found to be prohibitively expensive to run parameter scans for this case.

4.4 Assessment of the nonlinearly saturated perturbed magnetic energy

The change in the poloidal magnetic energy spectrum can in principle be used to infer how the magnetic configuration has been modified by the instability, and confirm whether a more energetically favourable state has been reached. As discussed in Section 2.4, for a free boundary mode, the magnetic energy should in principle be considered over all real space to account for the modification of the energy in the vacuum region. A method to compute the total energy could not be found, but the EXTENDER [115], NESCOIL [116], and MAKEGRID codes could be used to compute the plasma and vacuum magnetic fields in a finite domain both inside and outside the plasma volume on a R, Z, ϕ grid.

The magnetic field is therefore computed and Fourier decomposed inside a cylindrical torus, centred at $R = 10$, with minor radius, $r_{\text{minor}} = 1.75$. This torus contains all of the simulated cases considered in the parameter scans from Section 4.3. An example of the Fourier decomposed radial magnetic field, B_{R}, for an unper-

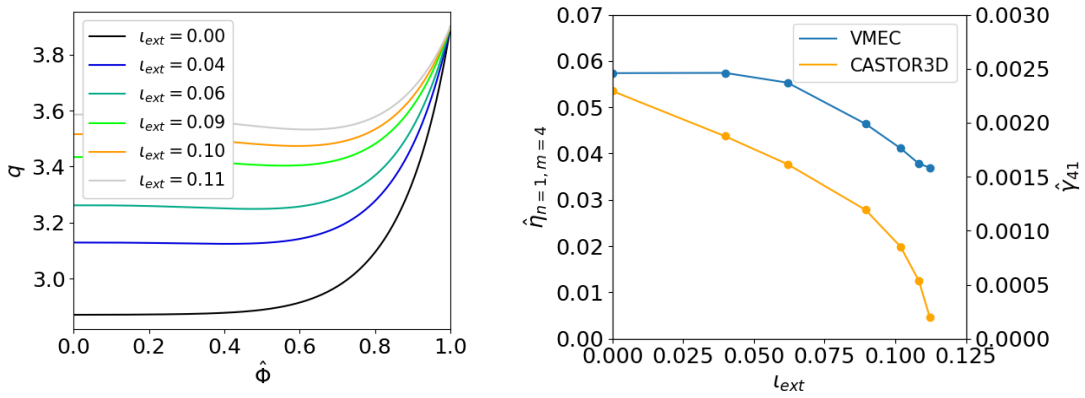

(a) (b)

Figure 4.8: Modification of the q profile (a) with increasing ι_{ext} for $l = 2$ $N_{\text{p}} = 5$ stellarators. The nonlinearly saturated perturbation amplitude (blue, left y-axis) decreases with the linear growth rate (orange, right y-axis). Note that computations at higher spectral resolution were not possible for this case, due to the demanding computational requirements.

turbed $l = 2$, $N_{\text{p}} = 2$ stellarator is shown in Figure 4.9. It should be noted that the $n = 2$ component of the equilibrium magnetic field is larger than the $n = 0$ component, indicating that it contributes a significant component of the equilibrium magnetic field.

The poloidal magnetic energy spectrum is then computed, normalising by the square of the volume averaged toroidal magnetic field such that results of different equilibrium computations can be compared with one another. The results for three cases with different field periodicities are shown in Figure 4.10. It can be observed that the energy in the perturbation is notably smaller in the stellarator cases.

A similar result to Figure 3.5 (a) is observed for the tokamak case. For stellarators however, it can be seen that the perturbation exists predominantly in the $N_{\text{f}} = 1$ mode family of the simulated stellarator device. This means that the energy corresponding to the perturbation cascades down from the dominant $n = 1$ mode to $n = 3$, 5, and so on in the $N_{\text{p}} = 2$ case. Equally in the $N_{\text{p}} = 5$ case, the $n = 4$ and $n = 6$ modes are notably larger than the members of the $N_{\text{f}} = 2$ mode family. These results are expected due to the toroidal mode coupling of the instability in stellarators.

In contrast, the $N_{\text{f}} = 0$ mode family shows a decrease in poloidal magnetic energy for $n > 0$ toroidal harmonics. This means that the plasma perturbation results in a reduction in the associated contributions of the symmetry preserving components of the perturbed equilibrium. A similar result is obtained for $N_{\text{p}} = 2$. This could be because these toroidal harmonics contribute to the equilibrium drive for the instability, which releases energy from these toroidal harmonics in the perturbed state.

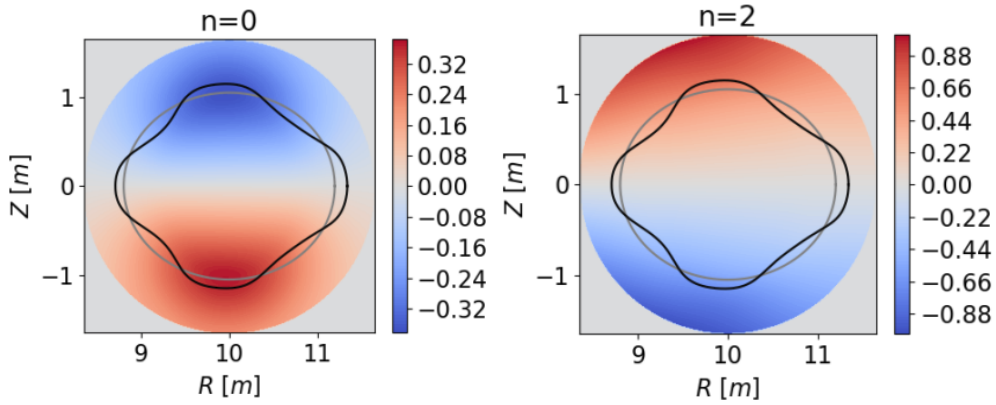

(a) (b)

Figure 4.9: $n = 0$ (a) and $n = 2$ (b) Fourier components of the total radial magnetic field, B_{R}, of the total magnetic field in tesla. The field is computed within a cylindrical torus enclosing the plasma volume in the $\phi = 0$ plane for a $l = 2$, $N_{\mathrm{p}} = 2$ stellarator with $\iota_{\mathrm{ext}} = 0.029$. The initial (grey) and perturbed (black) plasma boundary are overlaid on the data.

At the same time, it is important to note an unexpected result, which is that the $n = 0$ poloidal magnetic energy has increased in all cases. As in the tokamak case, the $n = 0$ energy provides the drive for the MHD instability, the overall energy in this mode should decrease as a result of the MHD perturbation. The computed energies in Figure 4.10 do not include the energy outside the cylindrical torus, and so it could be that this observation is due to the unaccounted energy in this part of the vacuum region. In order to understand the nature of the dynamics further, the local poloidal magnetic energy in the VMEC computations is compared with observations running a free boundary simulation with the JOREK code in the next section.

4.4.1 Understanding the increase in $n = 0$ poloidal magnetic energy

To understand the increase in the $n = 0$ poloidal magnetic energy, the local change of the $n = 0$ and $n = 1$ components of the tokamak case in Figure 4.10 is plotted in the $\phi = 0$ plane in Figure 4.11. Considering the $n = 1$ energy, the $m = 8$ poloidal mode structure is expected as the magnetic energy corresponds to the square of the magnetic field, which has a $m = 4$ dominant perturbation for the modelled (4, 1) external kink. As expected, the increase in energy corresponding to the perturbation is only in the region localised around the plasma boundary, where the flux surfaces of the equilibrium are modified most significantly.

The change in the $n = 0$ component is more global. Several structures can be observed. Firstly, there is a region where the poloidal energy has decreased around the plasma boundary. This is likely the energy lost in driving the MHD instability from the $n = 0$ mode. In addition to this effect, there is also a global structure in

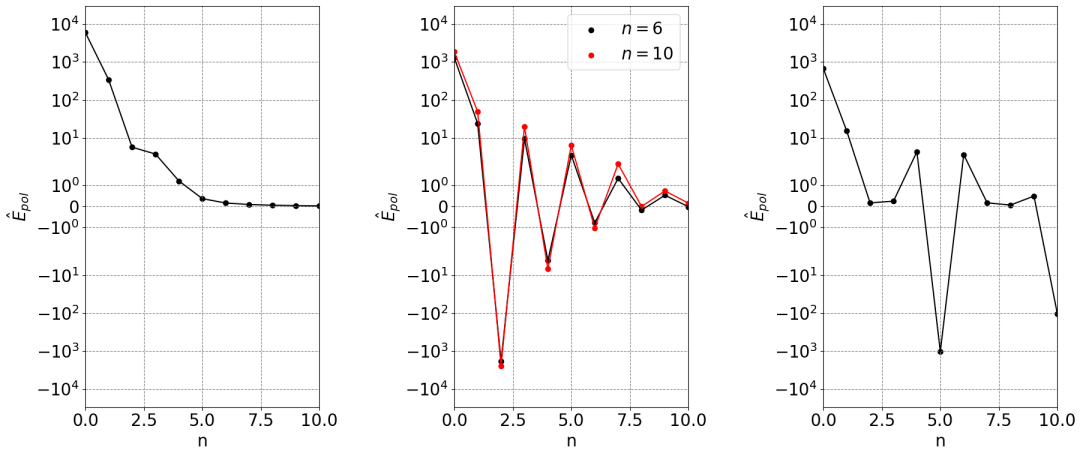

(a) (b) (c)

Figure 4.10: Perturbed magnetic energy of the tokamak (a), and $l = 2$ classical stellarators with $N_p = 2$ (b) and $N_p = 5$ (c) at $q_{edge} = 3.9$.

the plasma core. This can be identified as the result of a slight shift in the plasma axis, as shown in Figure 4.11 (c), where the influence of an axis shift is isolated by calculating the difference in total magnetic energy when the plasma currents of the unperturbed equilibrium are artificially shifted rigidly in the outboard direction. It can be seen however that the axis shift does not account for the increase in magnetic energy in the region outside of the plasma volume, observed in Figure 4.11 (a).

To understand this feature of the VMEC results, a free boundary JOREK equilibrium was constructed of the tokamak case. This equilibrium was then evolved with free boundary conditions applied to all toroidal harmonics. The evolution of the poloidal magnetic energies is shown in Figure 4.12. It can be seen in Figure 4.12 (b) that as the $n = 1$ external kink saturates, an increase in the $n = 0$ energy

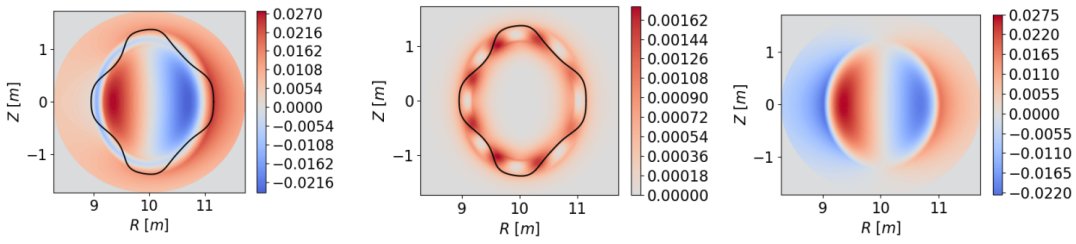

(a) (b) (c)

Figure 4.11: Change in the spatial distribution of the Fourier decomposed poloidal magnetic energy in the $\phi = 0$ plane for a tokamak case with $q = 3.9$ for the $n = 0$ (a) and $n = 1$ (b) toroidal harmonics. The change in the poloidal magnetic energy as a result of a radial axis shift of the unperturbed plasma (c) explains the core structure in the $n = 0$ component.

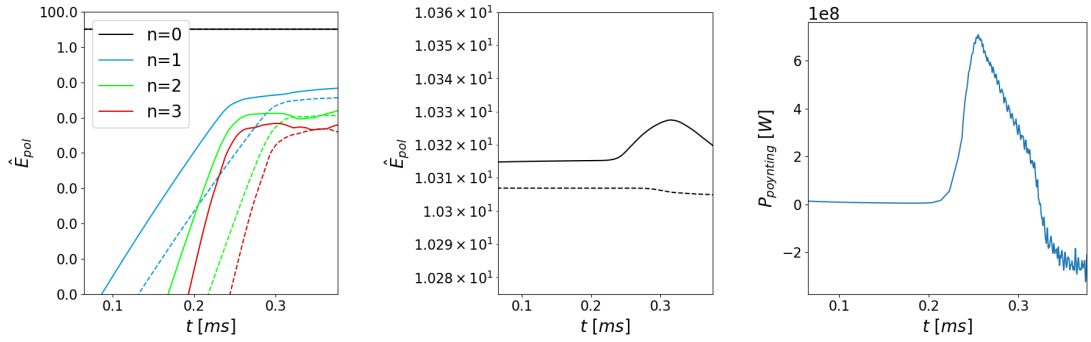

(a) (b) (c)

Figure 4.12: Evolution of poloidal magnetic energy spectrum (a and b) in $n = 0$ free (solid) and $n = 0$ fixed (dashed) boundary JOREK simulations of the tokamak test case modeled in VMEC with $q_{\text{edge}} = 3.9$. The Poynting flux (c) into the free boundary JOREK simulation domain indicates the increase in $n = 0$ integrated poloidal magnetic energy comes from the vacuum region.

is observed, similar to in VMEC computations. To confirm that this observation is related to the finite integral over the simulation domain, which does not capture all of the energy in the free boundary system, a simulation is also run applying a fixed boundary condition to the $n = 0$ poloidal flux. With this boundary condition, the $n = 0$ energy does not increase. The result is expected because the fixed boundary implies that the the simulated domain is a closed system, such that the total magnetic energy cannot increase as a result of the instability. Finally, the Poynting flux on the JOREK boundary is computed in the free boundary simulation case, as shown in Figure 4.12 (c). This diagnostic shows that there is a flux of magnetic energy into the system from the vacuum region.

The fixed boundary simulation, and the Poynting flux diagnostic confirm that the increase in the $n = 0$ energy in JOREK is due to an exchange of energy between the integrated volume, and the vacuum region. The exchange of energy is likely due to the changing current profile, and total plasma current. To first order, the confined plasma can be treated as a current carrying loop. If such a current loop has an increasing current, similar to the spike in current observed in the VMEC result, the induced Poynting flux will be towards the current loop. While the rearrangement of current in VMEC and JOREK results is more complex than such a simplified case, the first order effect of the dynamics should be similar, explaining the increase in the $n = 0$ energy in the integrated region. This analogy breaks down when considering the energy over all space, which would increase in the case of a loop with increasing current. In the case of the external kink, it is expected that the total energy would decrease because the spatial current distribution changes. At the time of writing, this aspect of the dynamics is not fully understood, but is intended as a topic of future work.

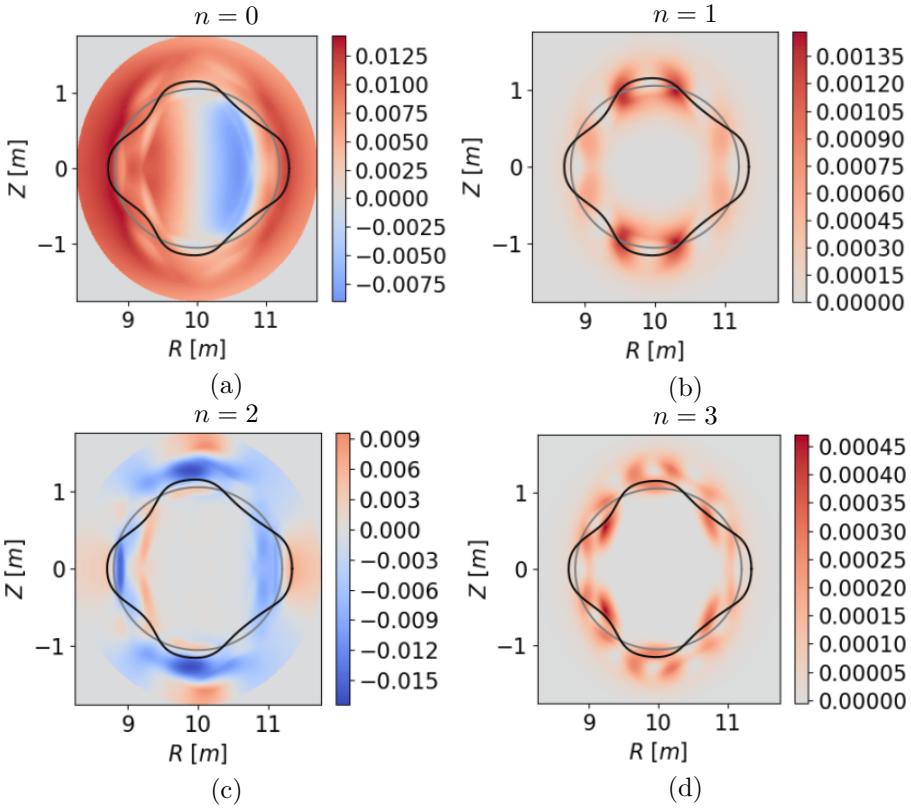

Figure 4.13: Fourier decomposition of the $n = 0 - 3$ poloidal magnetic energies (a-d) of the $l = 2$, $N_\mathrm{p} = 2$ stellarator with $\iota_\mathrm{ext} = 0.029$. The initial (grey) and perturbed (black) plasma boundary are overlaid on the data.

4.4.2 Poloidal mode structures in $l = 2$, $N_\mathrm{p} = 2$ stellarator case

The poloidal mode structure of the stellarator case, shown in Figure 4.13, is clearly more complicated than the tokamak case. Similar features can be observed in the $n = 0$ energy as in Figure 4.11, in terms of the increase in energy in the vacuum region, and internal structure corresponding to a small axis shift. The energies around the plasma boundary behave differently, however, because of the $l = 2$ stellarator field, which varies the plasma boundary toroidally. This means that parts of the perturbation to the equilibrium field are taken up by the $n > 0$ members of the $N_\mathrm{f} = 0$ mode family. This is also the most probable explanation for the drop in energy that can be seen in the $n = 2$ component of the perturbed energy.

Considering the $N_\mathrm{f} = 1$ mode family, the $n = 1$ toroidal harmonic has the same $m = 8$ mode structure as in the tokamak case in Figure 4.11, however the poloidal mode structure shows some localisation in the poloidal direction. It is currently unclear what causes this localisation. Equally, the $n = 3$ mode structure does not have an intuitive structure. The poloidal structure for this mode appears to be a

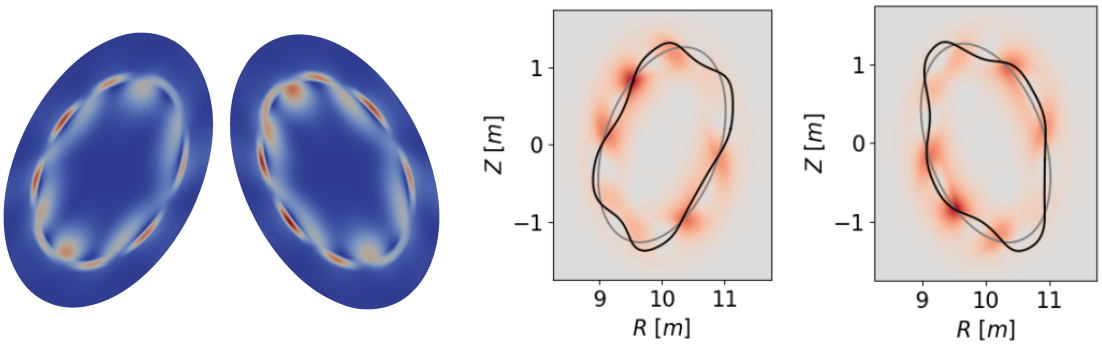

Figure 4.14: Qualitative comparison of $n = 1$ poloidal magnetic energy in a fixed boundary JOREK3D simulation with VMEC in comparable poloidal planes. It can be seen that the same poloidal localisation of the mode structure is observed in both codes. This comparison is not quantitative because the JOREK simulation could only be run fixed boundary, such that the results are not directly comparable.

combination of a $m = 6$ and $m = 12$ mode structure, neither of which correspond to the $m = 24$ mode number anticipated for the perturbed energy at the $q = 4$ resonance of the simulated instability.

While it is not clear what the reason is for the structures observed in VMEC, the structures can be compared with the recently implemented stellarator model in JOREK, as described in [47, 48] to cross validate the two approaches. The current implementation of JOREK3D is constrained to be fixed boundary, such that the dynamics of the external mode is stabilised compared to the VMEC case. Nevertheless, a comparison of the dominant mode structure in the $n = 1$ toroidal harmonic is possible and is shown in Figure 4.14. It can be seen that, in both computational approaches, the poloidal localisation of the mode can be identified in the same approximate region of the domain. This very preliminary result builds confidence in the two modelling approaches — although the numerical models differ significantly, they produce a similar dominant mode structure.

4.5 Discussion

Simple $l = 2$ classical stellarators have been used to gain an understanding of the behaviour of the VMEC equilibrium code when applied to model nonlinearly saturated MHD modes in stellarators. The results of comprehensive resolution scans indicate that the resolution requirements can be prohibitive for high field period devices, however saturated perturbations could be found for classical stellarators up to $N_\mathrm{p} = 5$ within the limits of reasonable computational resources.

It is possible for ι preserving VMEC computations to converge to different solutions depending on the resolution parameters, as previously described in the literature for current preserving computations of RMPs in tokamaks [63]. Which state

is a more physical solution for the MHD dynamics is still unclear. It is proposed to select the resolution parameters by applying an additional physical constraint informed by an intuition of the expected plasma current spike produced by the instability. Considering the physical parameter scans of saturated states that have been computed for $N_{\mathrm{p}} = 2$ stellarators, the expectation from nonlinear theory is that the under-resolved computations are more physical than the computations at higher toroidal resolution, where the mode amplitude grows with increased ι_{ext}.

Considering the evolution of the magnetic energy spectrum, the expected toroidal mode coupling is obtained in the stellarator solutions. Comparisons with JOREK simulations indicate that the unexpected increase in the $n = 0$ poloidal magnetic energy is reasonable, and due to an exchange of energy with the vacuum outside the integration region. Similar comparisons with the stellarator capable models in JOREK are currently limited, because a free boundary condition on the magnetic field has not been implemented for this model. However, preliminary comparisons of the dominant poloidal mode structure of the saturated state indicate that the structures observed in JOREK and VMEC are consistent, helping to build confidence in both approaches. Further work is necessary to understand the exact reason for the mode structures, that have been observed in Section 4.4. The work in this thesis chapter is intended for a future publication, where these outstanding issues will be addressed.

5 Validation of the virtual current model in JOREK

The virtual current model that was introduced in Section 2.6.2 and can be used to model stellarators axisymmetrically is validated against a series of ideal and resistive MHD benchmarks. Beginning with a comparison of tearing modes in a cylindrical plasma in Section 5.1, it is shown that the linear eigenfunction and expected stabilisation of the instability with increasing external rotational transform is observed. A vertical displacement event in a plasma with an elliptical cross section is then studied in Section 5.2. It is shown that the externally applied poloidal field prevents the VDE, as anticipated by previous analytical studies. In Section 5.3, linear growth rates for resistive double tearing mode and kink instabilities for W7-X equilibria with significant ECCD currents are then compared with other MHD codes. Good agreement is found between the axisymmetric approximation and fully 3D results. Finally, the linear growth rate for external kinks in simple $l = 2$ stellarators and a quasi-axisymmetric device are compared with linear results from CASTOR3D in Section 5.4. Reasonable agreement is obtained in the growth rates, and linear eigenfunctions of the modes, justifying nonlinear studies with the virtual current model, carried out in Chapter 6. The results of this thesis chapter have been presented at conferences in [117] and published in [114].

5.1 Tearing mode validation

The linear perturbation of the poloidal flux, Ψ_1, produced by a tearing mode in a cylindrical plasma can be determined by solving the tearing mode equation [75]

$$\frac{1}{r}\frac{\partial}{\partial r}\left(r\frac{\partial \Psi_1}{\partial r}\right) = \frac{m^2}{r^2}\Psi_1 - \frac{\frac{dj_\mathrm{p}}{dr}}{\frac{B_\theta}{\mu_0}(1-\frac{nq}{m})}\Psi_1, \tag{5.1}$$

where $j_\mathrm{p}(r)$ is the plasma current density, and all other variables have their usual definitions. As this model assumes a cylindrical plasma, the toroidal magnetic field is homogeneous, and the poloidal field is a function of the minor radius alone. As a result, modes are linearly decoupled both poloidally and toroidally, such that they can be analysed independently.

As it is expected that resistive effects are only significant in the region localised around the unstable rational surface, the plasma column can be separated into two parts. An ideal region extends from both the axis and plasma boundary to the rational surface being studied. Equation 5.1 describes the perturbation in this

region. Within the infinitesimal region around the rational surface, the dynamics must be treated resistively. For a physically reasonable solution, the poloidal flux must be continuous across the resistive region, but is allowed to have a discontinuity in its radial gradient, which would imply reconnection of the flux surfaces at the rational surface.

To solve this problem, a shooting code has been implemented, following the approach described in [75, 118]. The perturbed poloidal flux is found by matching solutions numerically integrated from the axis and plasma boundary to the rational surface of interest, located at $r = r_s$. First, a solution from the plasma boundary to the rational surface is found for a prescribed value of $\partial\Psi_1/\partial r$ on the boundary. $\partial\Psi_1/\partial r$ at the plasma axis is then iteratively modified until the solutions for both regions match at the rational surface to a given tolerance.

Having found a solution, it can be determined whether the plasma equilibrium is unstable, based on

$$\Delta' = \frac{\frac{\partial\Psi_1}{\partial r}(r_s + \epsilon) - \frac{\partial\Psi_1}{\partial r}(r_s - \epsilon)}{\Psi_1(r_s)}, \tag{5.2}$$

where ϵ is an infinitesimal distance from the rational surface, located at r_s. Equation 5.2 can be related to the Poynting flux. A positive value of Δ' implies a flux of magnetic energy into the rational surface, driving the instability, and causing magnetic reconnection.

To approximate stellarators using this method, $j_p(r)$, used in equation 5.1 can be reduced, while keeping the profiles for the poloidal and toroidal magnetic fields in the circular plasma fixed. This modification is equivalent to the virtual current model, where the total poloidal flux is preserved, while modifying the plasma current. The removed current in the modified equilibrium is essentially treated as virtual, in the sense described in Section 2.6.2.

The profiles used in this test case are shown in Figure 5.1. In this study, the total current is multiplied by a constant, $0 < 1 - \alpha < 1$ in order to produce the plasma current profile, shown in Figure 5.1 (b). For $\alpha = 0$, a cylindrical tokamak case is simulated, which is known to be tearing mode unstable. For $\alpha = 1$, all of the plasma current is treated as virtual current, such that a zero net current device is modelled, which must be stable for this current driven mode. Such an implementation should lead to similar results as the model outlined by Matsuoka et al. [95]. Their model is different, only in that the current density term in equation 5.1 is written in terms of the fraction of rotational transform generated by plasma currents, and they use profiles for the vacuum rotational transform which directly correspond to those of realistic stellarators.

It should be noted that the profiles modelled here do not resemble those of a realistic stellarator. This is because the removed virtual current, and resultant externally generated magnetic field does not necessarily resemble a field that could be generated by external field coils. Nevertheless, the configurations are a good first numerical test for the virtual current model.

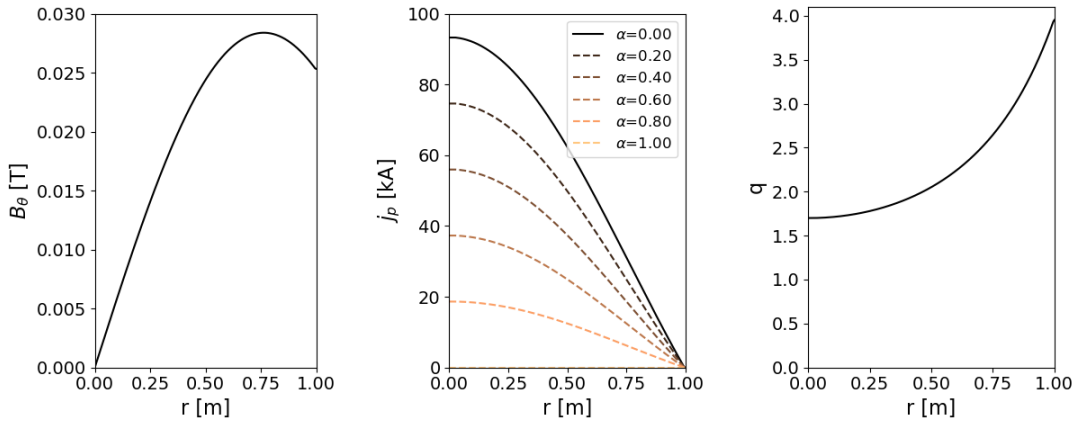

(a) (b) (c)

Figure 5.1: Input profiles for the poloidal magnetic field (a), plasma current (b), and q profile (c) used in the tearing mode test case. The toroidal field is 10 T. To test the virtual current model, the rotational transform of the plasma is held fixed, while a constant fraction of the total current density, α, is treated as virtual current across the plasma radius.

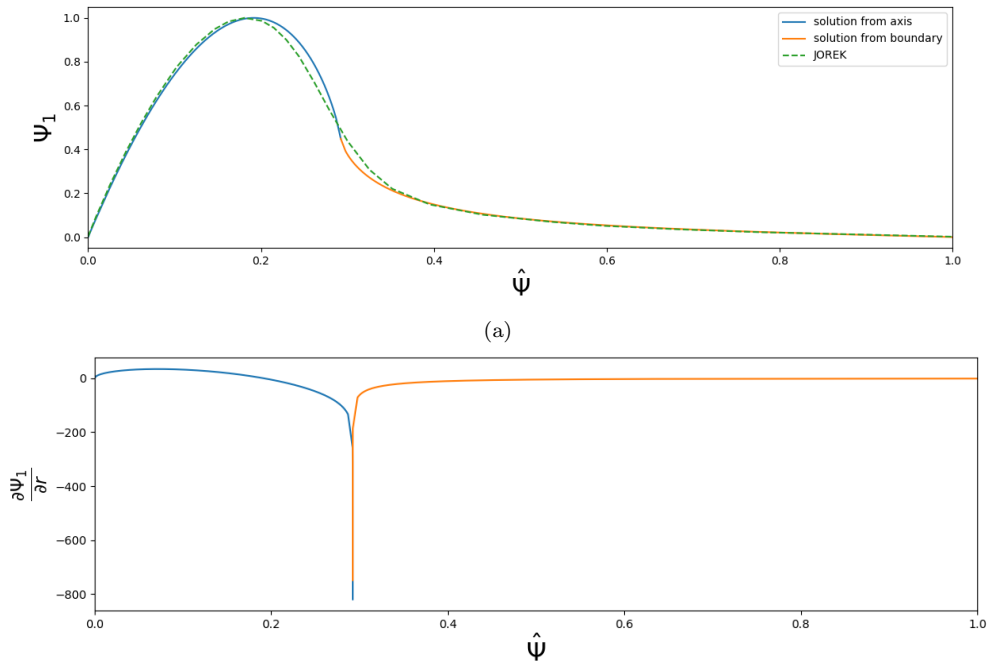

(a)

(b)

Figure 5.2: Plots of the poloidal flux perturbation (a) calculated by JOREK and the tearing mode equation. The plot of $\partial\Psi_1/\partial r$ (b) is used to show that there is a discontinuity at the rational surface in the solution to the tearing mode equation.

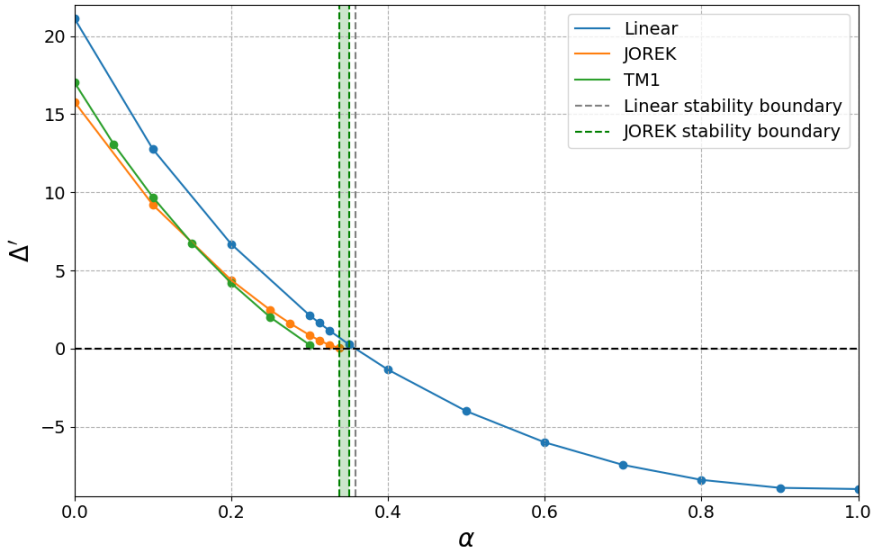

Figure 5.3: Stability parameter Δ' calculated from the linear tearing mode equation (blue), and MHD codes JOREK (orange) and TM1 (green), for varying current fractions, α, removed from the plasma. The dependence of Δ' on α and its stability boundary compare reasonably well for the three methods.

The solution of the perturbed poloidal flux given by the tearing mode equation and calculated in JOREK for $\alpha = 0$ is compared in Figure 5.2 (a). The discontinuity in $\partial\Psi_1/\partial r$ at the rational surface can be clearly seen in the solution to the tearing mode equation in Figure 5.2 (b). It can be seen that the solutions for Ψ compare well, except near the instability itself, where JOREK is more diffuse. This is not surprising as JOREK includes viscoresistive physics outside the infinitesimal region around the rational surface, and is limited by the resolution of the grid used to model the instability.

The stability parameter Δ' can be calculated from the growth rate from JOREK, and TM1 [119], a cylindrical plasma code, and compared with the result calculated from the tearing mode equation, for different values of α. The results of this comparison are shown in Figure 5.3. The results from JOREK and TM1 compare reasonably well, and follow the same trend as the linear theory. The results show that the virtual current model captures the correct linear structure of resistive modes for simple stellarator-like cases.

5.2 Vertical displacement event validation

In this section, a vertical displacement event is studied in a low beta, elliptical plasma. This test case is based on previous work in [21]. The VDE is triggered by introducing a small perturbation to the currents in the poloidal field coils, which

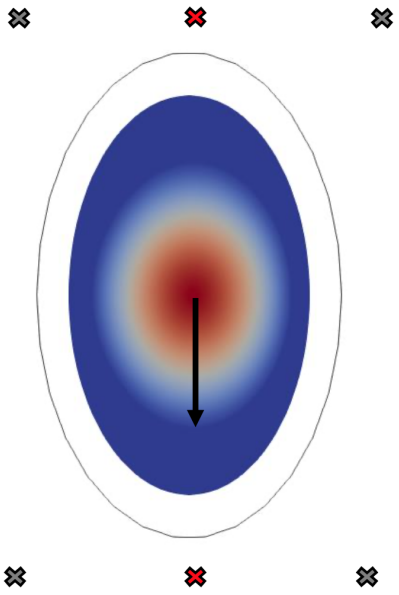

Figure 5.4: Simulation domain of the vertical displacement event test case. The red poloidal field coils are perturbed in order to induce the instability. By introducing virtual currents, the vertical displacement should be stabilised due to the cage-like restoring force of the external rotational transform.

are used to shape the plasma cross section. Figure 5.4 shows an illustrative plot of the simulation domain used in JOREK for this test case. It can be seen that part of the vacuum region is included in the simulated region. The resistive wall modelled with STARWALL is shown encompassing the simulation domain. The location of the poloidal field coils are also shown. To initiate the VDE, the red poloidal field coil currents are changed using a step function, adding a small amount of current to the lower coil, and removing an equal amount from the upper one. The consequence of this change is a small downward force. As the equilibrium coil forces are unstable, and approximately linearly dependent on the vertical displacement of the plasma axis, the displacement from its original equilibrium position should grow exponentially.

Herein, the test case is modified by exchanging plasma current for virtual current to see how this changes the dynamics of the VDE. Similar to Section 5.1, this exchange is done somewhat artificially by setting $j_\mathrm{v} = \alpha j_\mathrm{t}$, where $0 < \alpha < 1$. The external rotational transform of a stellarator produces a stabilising force that should alter the growth of the vertical displacement event, and eventually stabilise it. The restorative force can be more easily interpreted using the virtual current model, which effectively places an additional coil at the plasma axis. The virtual current therefore acts to pull the remaining plasma current back towards the original equilibrium axis.

In order to eliminate the influence of the external wall structures, a very high wall

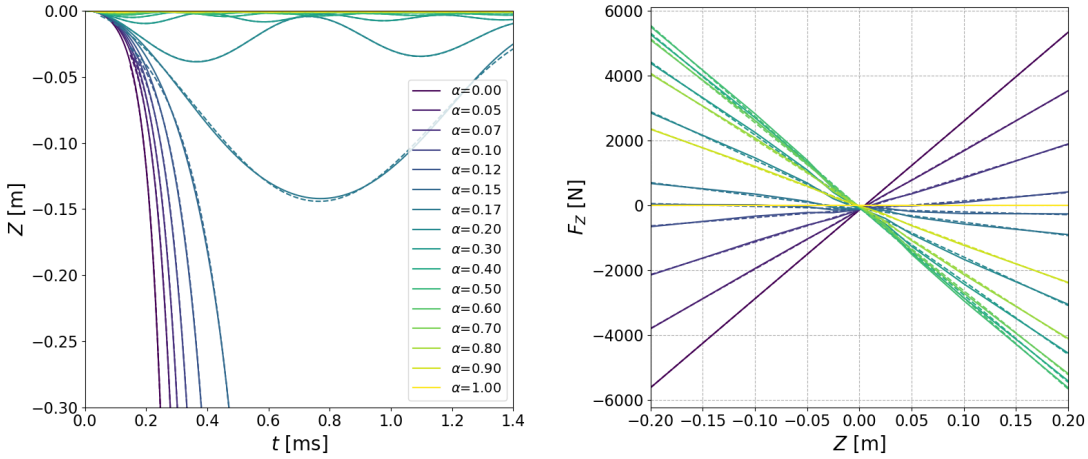

(a) (b)

Figure 5.5: Vertical position of the plasma axis (a) and integrated vertical force (b) on the axis for a given displacement. Results are calculated with varying fractions of virtual current, α. It can be seen that the integrated force on the plasma becomes stabilising, and eventually force free. The transition to a stabilising force corresponds with the transition from an exponential growth in the plasma axis position to a step response.

resistivity is used, such that the simulations are in the no wall limit. Thus, there is no significant nonlinear stabilising force produced by the wall structures. The simulations use only the $n = 0$ toroidal harmonic so that any nonlinearly triggered MHD activity produced by the VDE is suppressed.

The motion of the plasma axis is shown in Figure 5.5. As the virtual current is increased, the motion of the plasma column transitions from the exponential growth to a damped step function, moving the equilibrium to a new stable position, which has been slightly modified by the perturbation applied to the coils. In a typical fusion plasma, the motion is expected to be underdamped, because the viscosity and damping produced by surrounding resistive structures interacting with the plasma should not be strong enough to produce an overdamped motion. As a result, the plasma column overshoots the new equilibrium point, and oscillates around it, eventually becoming stationary.

The observed types of motion are found in many contexts in physics. The unstable exponential growth can be approximated by

$$Z(t, Z_0, \delta Z, \gamma) = Z_0 + \delta Z e^{\gamma t}, \tag{5.3}$$

where Z_0 is the original axis position, and δZ is the initial displacement. The second type of motion is similar to a mass-spring-damper system. In this context, the spring represents the restoring force produced by the virtual currents, once they are dominant over the poloidal field coils. The damper represents the viscosity of

the plasma, which resists its motion. The qualitative dynamics can therefore be estimated by approximating the plasma motion as a rigid displacement, using the typical equations of motion for an underdamped step response

$$z(z_{\text{offset}}, \zeta, \omega_0, \theta_0, t) = z_{\text{offset}} \left[1 - \frac{1}{\sqrt{1-\zeta^2}} e^{-\zeta\omega_0 t} \sin(\omega_0 \sqrt{1-\zeta^2} t - \theta_0) \right]. \tag{5.4}$$

The growth rate, γ, and the oscillation frequency, $\omega_0\sqrt{1-\zeta^2}$, in equation 5.3 and 5.4 can be approximated by integrating the vertical force on the plasma column, assuming a rigid vertical displacement of the entire plasma from its equilibrium axis position. The result of this integration is shown on the righthand side of Figure 5.5. The gradient of the force as a function of vertical position can be used to approximate the growth rate of the axis position as

$$\gamma = \sqrt{\frac{\frac{\partial F_{\text{Z}}}{\partial Z}}{M}}, \tag{5.5}$$

where M is the total mass of the plasma column. $\partial F_{\text{Z}}/\partial Z$ is approximated using a linear fit to the data in Figure 5.5. The oscillation frequency can be approximated using the same formula.

These parameters can also be computed by fitting the axis position data, using equations 5.3 and 5.4. The dashed lines in Figure 5.5 represent the fits of the simulation data. In such a way, the values of γ and $\omega_0\sqrt{1-\zeta^2}$, extracted from the simulation time traces can be compared with the expected values of these parameters from the computation of F_{Z}. The comparison is shown in Figure 5.6.

The transition to vertical stability with increasing virtual currents is well matched by the simulation results, however there are discrepancies in the oscillation frequency, and growth rate away from the transition point. These differences are attributed to nonlinear effects that are not taken into account in the force integral approximation. For low values of α, where the plasma motion is significant, nonlinear stabilising effects play a role. Currents are induced in the computational domain extending beyond the actual plasma boundary due to the small but finite conductivity as a result of the fast motion of the plasma. These currents oppose the plasma motion, reducing the growth rate of the vertical displacement event.

Equally, close to $\alpha = 1$, the currents induced in the plasma by the change in the poloidal field coil currents needs to be taken into account. Although these currents are very small, when most of the current is no longer carried by the plasma, they can significantly stiffen the plasma column, leading to a small amplitude perturbation of the axis, at a high oscillation frequency. Accommodating for these nonlinear effects, the behaviour of vertical displacement events with virtual currents appears to be in good agreement with expectations.

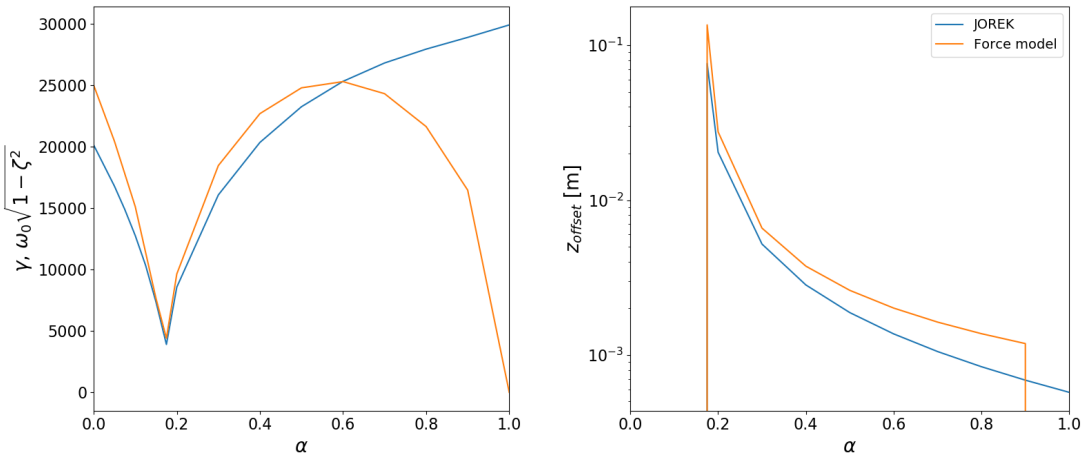

(a) (a)

Figure 5.6: Fits to the growth rate and oscillation frequency of the plasma (a), and final offset of the plasma axis (b), at varying fractions of virtual current, α. There is a good match between the results at low values of α. The reduction in the plasma growth rate and oscillation frequency is thought to be due to nonlinear damping from eddy currents in the vacuum region that has a low but finite conductivity in JOREK. As α increases and the initial conditions of the plasma become force free, the nonlinearities of the induced currents from the changing magnetic field produced by the poloidal field coils are thought to be the cause of the oscillations at high frequency.

5.3 Comparison of double tearing and resistive kink modes in Wendelstein 7-X

After the simplified test cases considered in Sections 5.1 and 5.2, a more challenging validation case for MHD activity observed in the W7-X stellarator is now described. Recent experiments on Wendelstein 7-X have induced plasma terminating events through ECCD. The ECCD currents modify the q profile of the device near the plasma centre, introducing multiple (1, 1) rational surfaces, as shown in Figure 5.7. MHD activity around these low order rational surfaces is one potential cause for the plasma termination observed in experiments.

To test this hypothesis, modified W7-X equilibria had been investigated in previous work using CASTOR3D and TM1 [99, 120]. The results of linear MHD analysis indicate the presence of resistive (1, 1) internal kink, and double tearing modes in the core of the device. The internal kink is expected to lead to nonlinear dynamics similar to the internal relaxation model originally described by Kadomtsev for tokamaks [121].

JOREK is used to model axisymmetric approximations of W7-X using both the tokamak approximation, and virtual currents. Two axisymmetric approximations

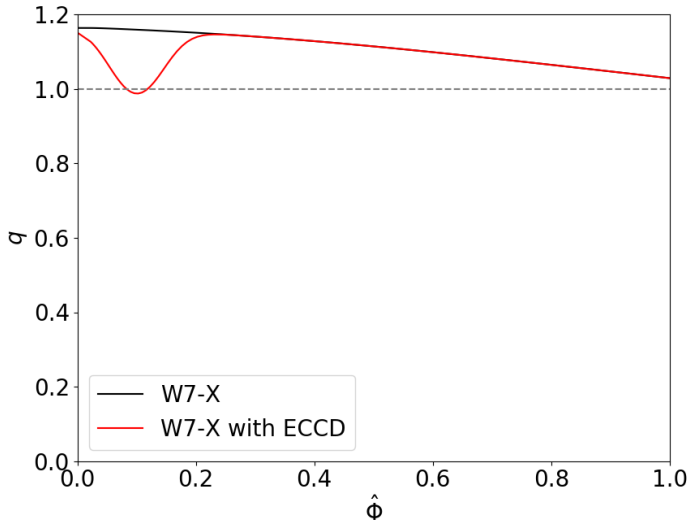

Figure 5.7: Wendelstein 7-X q profiles, with and without ECCD respectively. Note that Ref. [120] scans over a variety of different cases linearly to account for uncertainties regarding the exact configuration, while the work with JOREK focuses on one case for simplicity.

of the plasma boundary are taken. These approximations are compared with the full non-axisymmetric flux surfaces in Figure 5.8. The first maps the W7-X geometry to an equivalent cylindrical plasma, with the average minor radius of the original stellarator equilibrium, using a similar workflow to that shown in Figure 2.4 with a cylindrical boundary. This approximation is similar to those that have been used in a recently published TM1 study [99]. The second uses the $n = 0$ Fourier harmonics of the original equilibrium to define the axisymmetric approximation, as described in Section 2.6.2. By comparing these two axisymmetric approximations, it should be possible to assess the importance of the boundary approximation for the axisymmetric model.

The two approximations are compared with linear studies by TM1 and CASTOR3D in Figure 5.9. The axisymmetric approximations are modelled using both the tokamak and virtual current approximations. In both axisymmetric models, resistive tearing modes are observed from $n = 1$ to 16. Using the tokamak approximation with the $n = 0$ Fourier coefficients defining the boundary, the $n = 1$ mode shows a sharp change in the trend of the growth rates. This is because a (1, 1) resistive kink mode is identified in JOREK, which exceeds the growth rate of the double tearing modes that the CASTOR3D results correspond to.

It should be noted that the virtual current approximation has a larger growth rate than the equivalent tokamak approximation for this case, even though the total plasma current is higher in the tokamak approximation. The reason for this can be identified by considering the function for FF', and $F_{\mathrm{v}}F'_{\mathrm{v}}$, shown in Figure

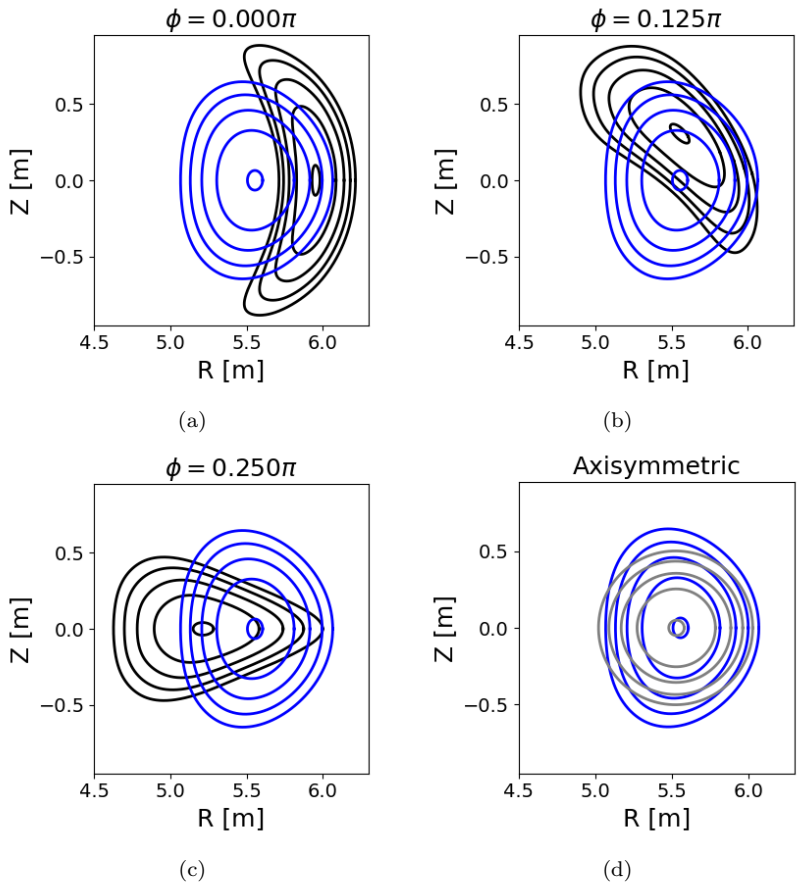

Figure 5.8: Comparison of flux surfaces of W7-X (blue) and its axisymmetric approximation based on $n = 0$ Fourier coefficients (black) in different toroidal planes (a-c). The circular axisymmetric approximation (grey) is also shown (d).

5.10. The contribution of the virtual currents are increasing from the plasma axis to the simulation boundary. This is a common characteristic of virtual currents approximating a realistic vacuum external rotational transform. In a real device, the vacuum poloidal magnetic field contributing to the rotational transform should be strongest near the plasma edge, where the distance to the external field coils is reduced. The result of the additional current in the tokamak approximation is a small reduction in the local current density gradient around the resonant $q = 1$ surfaces. In such a way the current drive of this resistive instability is reduced.

The comparison shows good agreement between the three codes. It should be noted that in CASTOR3D, the full non-axisymmetric instabilities were only modeled up to $n = 10$. For higher n, computations become numerically very demanding as many toroidal and poloidal harmonics need to be taken into account. Due to the complicated Fourier spectra of the eigenmodes caused by the coupling of toroidal harmonics, and due to the numerical challenges posed by the considered case, the

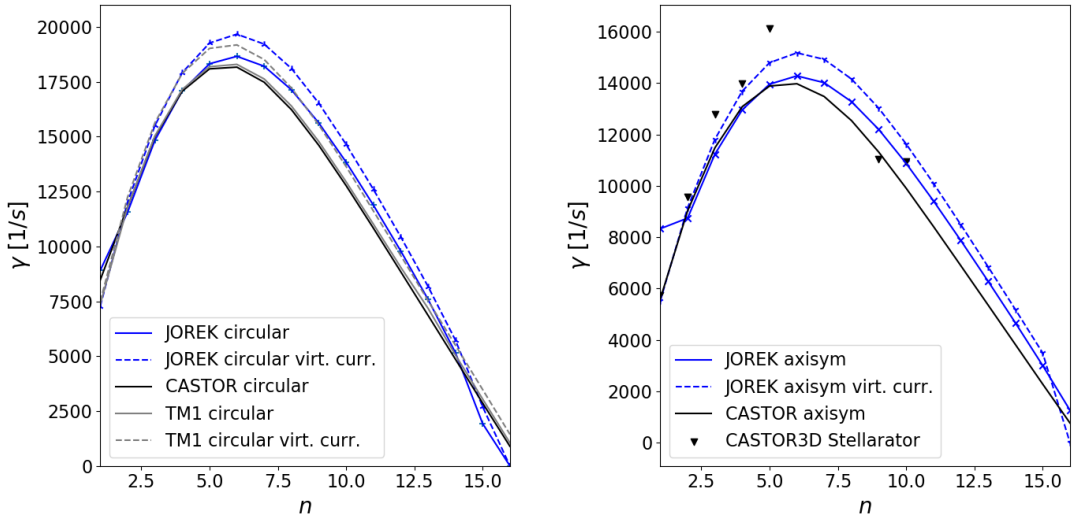

(a) (b)

Figure 5.9: Comparison of double tearing mode and resistive kink growth rates for Wendelstein 7-X, using TM1 (grey), CASTOR3D (black) and JOREK (blue). The axisymmetric approximations are constructed using a circular boundary (a) and one constructed from the $n = 0$ Fourier harmonics of the W7-X boundary (b). The test case is simulated using both the equivalent tokamak (solid) and virtual current model (dashed).

$n = 6$, 7, and 8 modes in CASTOR3D could not be identified in this study.

The error between the full non-axisymmetric CASTOR3D simulations, and the virtual current JOREK simulation using the $n = 0$ Fourier boundary, are within 10 % of one another. This shows that the virtual current model can approximate the full 3D stellarator for such internal modes, even for a device that violates some of the assumptions of the stellarator expansion, due to its non-planar axis, and strong shaping.

5.4 External kinks in $l = 2$ and quasi-axisymmetric stellarators

In this section, external kinks are modelled in two stellarator equilibria to validate the use of the virtual current model for studying these instabilities. A simple $l = 2$ stellarator is considered in the linear validation, alongside the main QA stellarator that is continued into the nonlinear phase in Chapter 6. As will be shown, the results of the virtual current model deviate slightly more for this test case, than for those considered in the previous sections. The $l = 2$ stellarator case is used to better understand the reasons for the larger discrepancy.

The equilibrium profiles of the test cases are shown in Figure 5.11, alongside the profiles of their corresponding axisymmetric approximations. The $l = 2$ stellarator

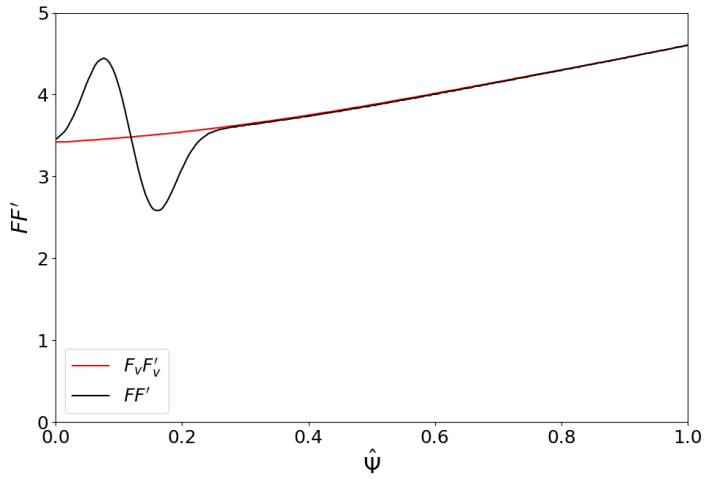

Figure 5.10: FF' (black) and $F_{\mathrm{v}}F'_{\mathrm{v}}$ (red), as defined by equation 2.44, for the W7-X case, using the $n = 0$ Fourier harmonics of the stellarator to define the boundary. The additional current in the tokamak approximation is represented by $F_{\mathrm{v}}F'_{\mathrm{v}}$, and increases towards the plasma boundary. This is the reason for the stabilising effect the increase in current has on the mode. In the virtual current approximation, the additional current is subtracted away from the total current so that for $\hat{\Psi} > 0.25$, there is effectively no plasma current in the device.

was designed as a simple linear test case for external kinks, to validate the virtual current model in a high aspect ratio, low β stellarator, within its known region of validity. A flat current density profile is assumed so that the case would be strongly unstable to external kink modes. The QA configuration is a version of the two field period equilibrium previously modelled in [85], where the pressure profile was modified to

$$p(s) = \begin{cases} (p_0 - p_{\mathrm{vac}})(1 - 2s + s^2) + p_{\mathrm{vac}} & \text{for } s \leq 1 \\ p_{\mathrm{vac}} & \text{for } s > 1 \end{cases} \tag{5.6}$$

where p_0 and p_{vac} are the pressure on axis and in the vacuum region, respectively. This profile ensures that the gradients of density and temperature at the plasma edge smoothly transition to the vacuum conditions. The q profile was also shifted upwards such that the edge safety factor is closer to the $q = 2$ rational surface than in [85]. To obtain a reasonable temperature of approximately 10 keV, the number density is set to 3.295×10^{20} m^{-3}.

Figure 5.11 compares the equilibrium stellarator profiles with their tokamak and virtual current approximations. As described in Section 2.6.2, the profiles have been extended into the vacuum region. The pressure profile is identical in all three cases. The safety factor profile is the same for the stellarator and its approximations

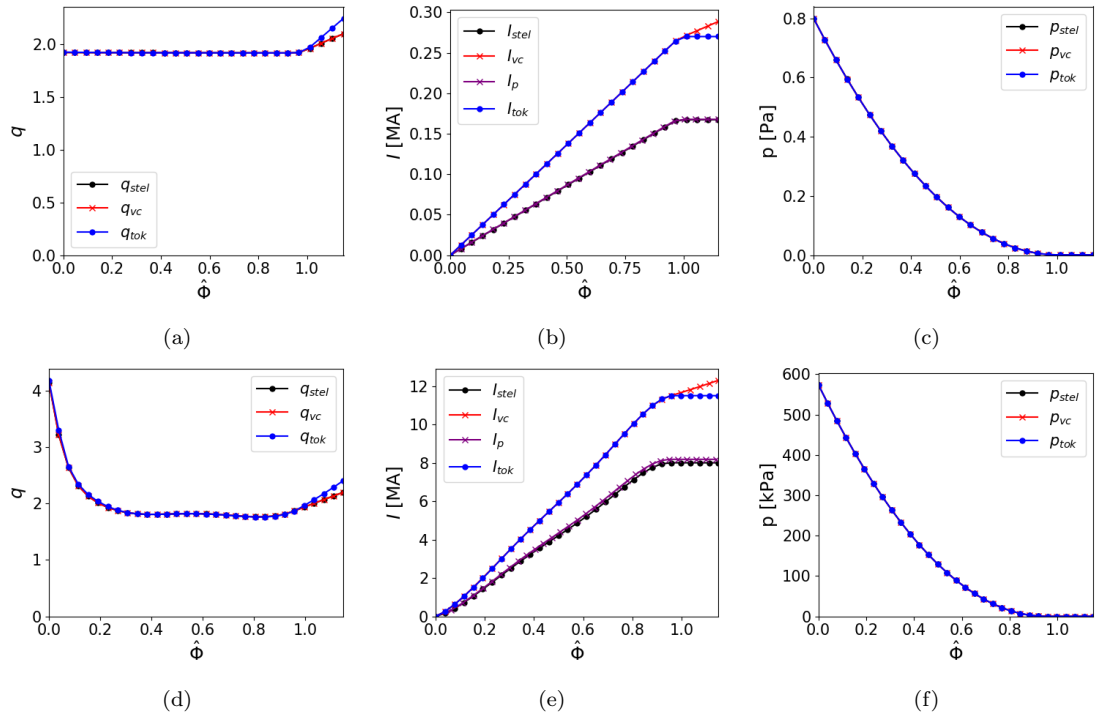

Figure 5.11: Equilibrium profiles for the $l = 2$ stellarator (a-c) and QA device (d-f) test cases, and their axisymmetric approximations. The equivalent tokamak approximation (blue) has a larger total toroidal current, I_{tok}, and vacuum magnetic shear than the stellarator (black). The virtual current approximation (red) has the same pressure, and safety factor profile as the stellarator. I_{vc} continues to increase in the vacuum region, beyond $\hat{\Phi} = 1$. I_{p} is the plasma current in the virtual current model, defined by equation 2.47.

within the plasma, except at the plasma edge. In this region, it can be seen that the magnetic shear in the tokamak case is larger than the stellarator and virtual current approximation. As discussed in Section 2.6.2, this is because the contribution from the external rotational transform in the vacuum region has been neglected. The virtual current approximation matches the stellarator profile outside the plasma by having virtual current in the vacuum region to represent the field generated from external coils.

Figure 5.12 shows the flux surfaces of the generated equilibria for poloidal cross sections at $\phi = 0.0\pi$, 0.25π and 0.5π. After the extension of the plasma, the QA equilibrium has not changed considerably from Figure 1 of [85]. The $n = 0$ Fourier harmonics of the QA equilibrium are compared with the corresponding surfaces from the axisymmetric approximation in Figure 5.12 (d) and (h). Here, it can be seen that the Shafranov shift of the axisymmetric approximation is larger than the 3D case. For the $l = 2$ stellarator, the pressure has been set to an artificially low value, removing this discrepancy. This shows one of the limitations

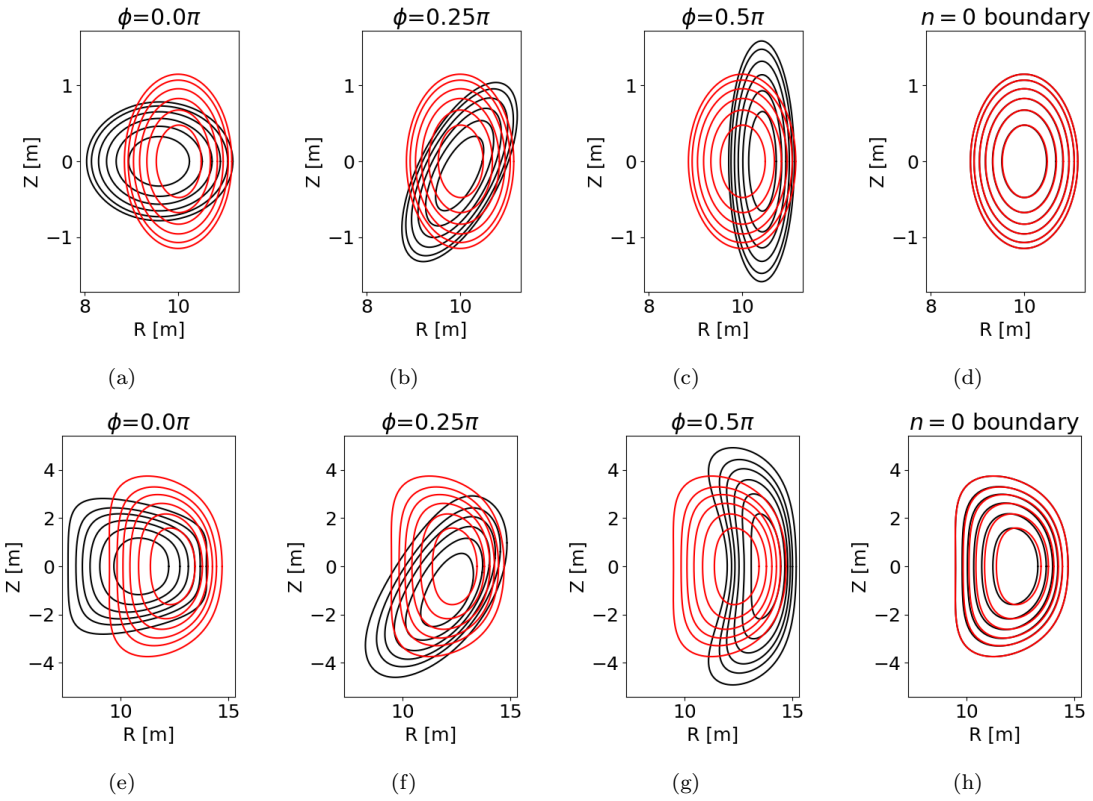

Figure 5.12: Flux surface contours for the $l = 2$ stellarator (a-c) and QA configuration (e-g) test cases. Surfaces of the stellarator equilibria (black) and their virtual current approximations (red) are overlaid at different toroidal planes. The $n = 0$ Fourier components of the complete $l = 2$ stellarator equilibrium (d) are aligned with the flux surfaces of its axisymmetric approximation. A similar comparison for the QA configuration (h) shows a deviation in the Shafranov shift.

of the axisymmetric approximation, which is that the correct magnetic well of a stellarator cannot be captured for the QA case. As a result, the plasma can shift further towards the low field side of the device, modifying the magnetic shear, and local current density gradient, which can have an effect on the MHD stability.

The linear growth rates of the external kink modes observed in the original QA configuration and its axisymmetric approximations are shown in Figure 5.13. For the non-axisymmetric results computed with CASTOR3D, the mode number of the instabilities corresponds to the dominant toroidal mode number of the respective eigenfunction, and the results are split into odd and even mode families. The sinusoidal and cosinusoidal pairs for each n of the stellarator instabilities are also plotted. These orthogonal solutions are only non-degenerate at low toroidal mode numbers in the QA case. For the $l = 2$ stellarator, with a simpler 3D geometry, the two mode families do not diverge significantly. Numerical difficulties were en-

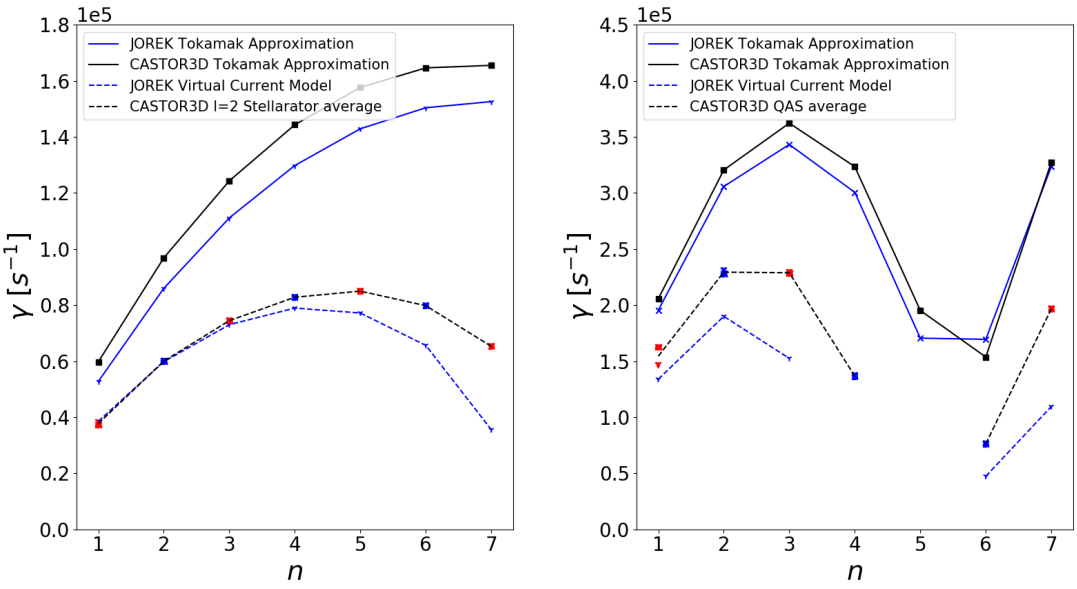

(a) (b)

Figure 5.13: Linear growth rates of external kinks observed in the $l = 2$ (a) and QA (b) stellarators, corresponding to the equilibria in Figures 5.11 and 5.12. The stellarator average and QAS average lines (black dashed) refer to the average of the sinusoidal (triangles) and cosinusoidal (squares) orthogonal solutions of the odd (red) and even (blue) mode families. This average of the stellarator modes is used to compare against the virtual current model (blue dashed).

countered when solutions of extended equilibria, which include part of the vacuum region outside the plasma, were used in CASTOR3D. For this reason, the 3D equilibria are only modeled in CASTOR3D up to the plasma boundary, coupling the vacuum and MHD equations at this interface.

The comparison of the growth rates in the tokamak approximation show very good agreement in JOREK and CASTOR3D for both the $l = 2$ and QA configuration. In the QA case, the lower growth rates close to $n = 5$ and $n = 6$ are attributed to poloidal mode coupling between $(m \pm 1, \mathrm{n})$ pairs inside and outside of the plasma near the plasma boundary, which provide a stabilising effect. This effect can be shown by plotting the relative contributions to the radial displacement eigenfunction, $\xi_\perp$, of the sideband poloidal modes, compared with the dominant (m, n) pair, as shown in Figure 5.14. The $l = 2$ stellarator case, shown in Figure 5.14 (a), has very little poloidal shaping, and thus mode coupling in this stellarator is not expected to be significant, the relative contributions of poloidal sidebands remains small. For the QA case, the results in Figure 5.14 (b) show that there is stronger poloidal mode coupling for the $n = 5$ and $n = 6$ cases.

The (9, 5) and (11, 6) modes are very close to the plasma edge. Small deviations

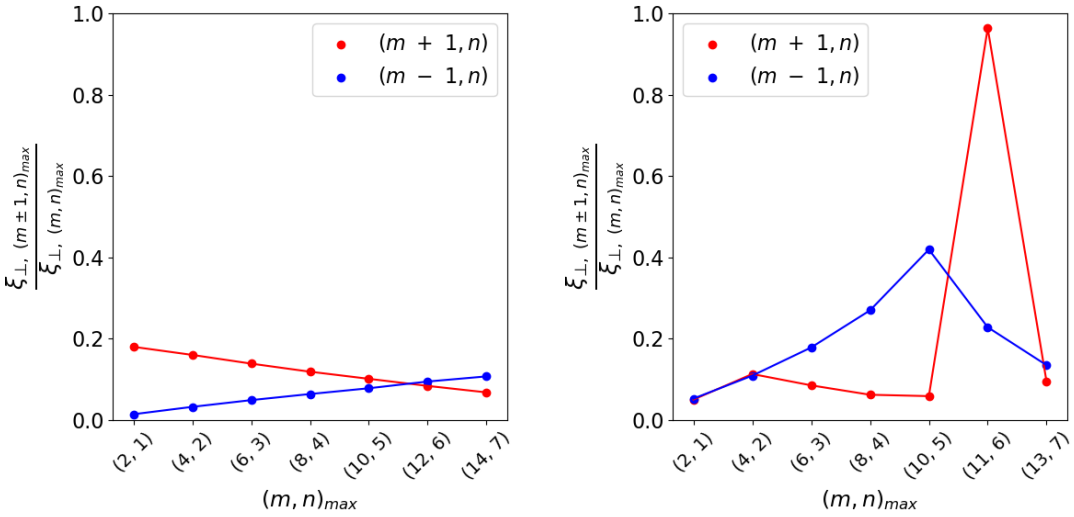

(a) Equivalent l=2 tokamak

(b) Equivalent QAS tokamak

Figure 5.14: Relative magnitude of the maximum radial displacement, $\xi_\perp$, contributions of poloidal sidebands $(m \pm 1, n)_{\max}$ compared to the dominant pair, $(m, n)_{\max}$. The large relative amplitude of the $n = 5$ and 6 modes for the equivalent tokamak of the QAS case indicate more poloidal mode coupling, because the edge safety factor is closer to the $q = 9/5$ and $12/6$ rational surfaces, inside and outside of the plasma, respectively.

in the q profile, and resistivity profile, which defines the plasma boundary, can strongly influence the contribution of the sideband modes close to the plasma edge, and lead to larger deviations between the two codes. In the $l = 2$ stellarator case, the flat q profile was intentionally chosen to be above the closest lower sidebands of the $q = 2$ surface for toroidal modes up to $n = 7$. Figure 5.14 (a) shows that the poloidal coupling is therefore reduced compared to the QA result in Figure 5.14 (b).

The above comparison of the equivalent tokamak approximations serves to demonstrate that the reduced MHD model used in this study is appropriate for modeling these external kinks. Comparing the virtual current model with the stellarator results from CASTOR3D, it can be seen that the general trend of the instabilities is captured in both cases. Particularly in the QA configuration, the deviations are largest where the dominant (m, n) mode is stabilised by its $(m \pm 1,\ n)$ poloidal sidebands. In particular, the $n = 4$ mode found in CASTOR3D for the QA configuration was not observed in JOREK. The reason for the modification of the mode structure cannot be identified from the growth rates alone, but is expected to be due to the modification of the toroidally averaged flux surfaces between the two cases, as shown in Figure 5.12. The compression of the flux surfaces on the outboard side of the tokamak approximation, due to the enhanced Shafranov shift should lead to enhanced poloidal mode coupling. Figure 5.14 (b) shows that this

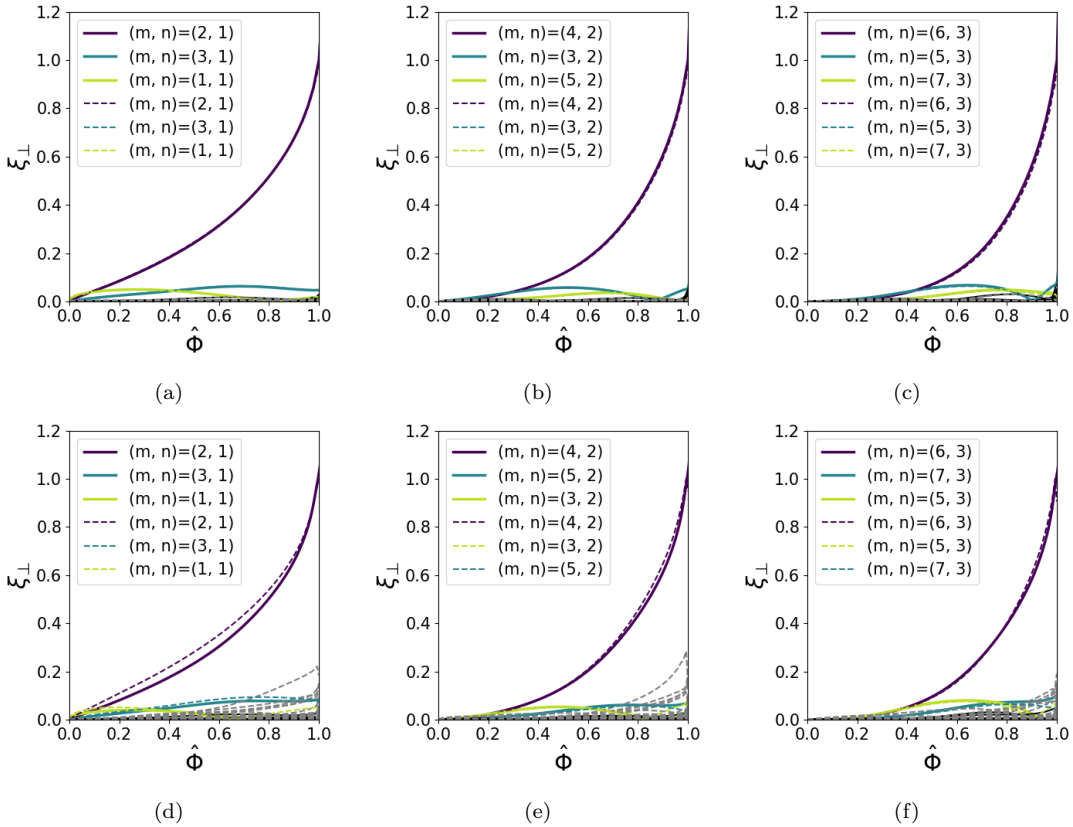

Figure 5.15: Radial displacement eigenfunction comparisons of JOREK (solid) with CASTOR3D (dashed) in Boozer coordinates. The tokamak approximations (a-c) show very good agreement. The virtual current model (d-f) instabilities have similar contributions from the leading toroidal harmonic of the equivalent QA instability in CASTOR3D.

effect is especially important for $4 <= n <= 6$, and could therefore explain why the $n = 4$ mode is stabilised.

To obtain a more detailed comparison of the mode structure, the eigenfunctions for the radial displacement in the QA case are shown in Figure 5.15. The results are compared using Boozer coordinates [14]. The radial structure of the instabilities is remarkably similar for the tokamak approximation. Comparing the virtual current model with 3D results, the structure of the captured contributions from the leading toroidal mode number of the instability compare very well. The grey dashed lines that grow in amplitude towards the plasma edge are from toroidal sidebands of the stellarator instability observed in CASTOR3D, as discussed in Section 2.4.2. The virtual current approximation does not capture the toroidal mode coupling of a stellarator, because the equilibrium magnetic field is not a function of the toroidal coordinate.

The linear mode structure of the virtual current approximation, and the true

stellarator agree surprisingly well, given the complexity of the case being modeled. In particular, the growth rate of the $n = 1$ instability is captured. As it will be shown in the next section, the $n = 1$ mode is dominant in the nonlinear dynamics. For this reason, the virtual current model is considered a reasonable tool for a preliminary study of these modes, which can provide an understanding of the nonlinear dynamics.

5.5 Discussion

In this section, the virtual current model has been validated using a variety of ideal and resistive benchmarks. The purpose of this exercise is to show that the model works and understand what problems it can be reasonably applied to. As can be expected from the ordering in Section 2.6, the low β, high aspect ratio tests of tearing modes, and VDEs capture the expected stabilisation of the instability. This is sufficient evidence to show that the implemented virtual current model provides accurate results within the region of validity of the stellarator expansion which it is based on.

Because the majority of physics questions of interest in stellarator research lie outside this region of validity, the model has been used on more advanced test cases to see how much the linear dynamics are changed as a result of the approximation. Somewhat surprisingly, it has been shown that low n current driven instabilities observed in W7-X can be simulated, obtaining similar linear dynamics to what has been observed in full MHD linear codes. Pushing the model further outside of its intended region of validity by modelling a low aspect ratio, high β, QA equilibrium, comparable growth rates and linear eigenfunctions were found in the axisymmetric approximation of the advanced stellarator when compared to full MHD codes.

It should be emphasised that the above results do not show that the model can be applied to any advanced stellarator of interest. The virtual current model is a severe approximation. However, for the simulated test cases, the observed error in the model is sufficiently small to justify using the model in order to gain a first order understanding of the dynamics in the considered advanced stellarators. The nonlinear dynamics of the W7-X case has been analysed in independent work from this thesis [99]. In the next chapter, simulations of the QA stellarator case in Section 5.4 are continued into the nonlinear phase.

6 Nonlinear simulations of a quasi-axisymmetric stellarator

In this chapter, the linear study of an external kink unstable QA stellarator presented in Chapter 5 is continued into the nonlinear phase. The purpose of this study is to understand the extent to which confinement is lost as the external rotational transform is varied. The simulation parameters used are outlined in Section 6.1. In order to see the influence larger fractions of external rotational transform can have on the dynamics, this parameter is artificially increased, such that the whole parameter space from an equivalent tokamak to zero net current carrying stellarator could be explored. The nonlinear evolution of the external kink is studied in detail in Section 6.2. It is shown that the relatively small external rotational transform used in the real QA stellarator, $\iota_{\text{ext}} \approx 0.15$, does not have a significant stabilising effect on the external kink mode, leading to strong MHD activity. For larger fractions of external rotational transform, a strong loss of confinement is still observed because of nonlinearly triggered internal MHD activity at the $q = 1.8$ and $q = 1.75$ rational surfaces. It is only after a significant amount of plasma current is removed from the device that the MHD activity is sufficiently stabilised to prevent a major loss in confinement, as measured by the connection length of field lines to the edge of the simulation domain. The results of this thesis chapter have been presented in conference proceedings [122] and published in [114].

6.1 Simulation set up and numerical parameters

6.1.1 Numerical and diffusive parameters

Before continuing the simulation from Section 5.4 into the nonlinear regime, some modifications need to be made to the numerical and diffusive parameters used in the simulations. This is because the linear simulations were set up to match the boundary conditions of CASTOR3D, modeling a highly resistive vacuum region outside of the plasma, and approaching the zero viscosity limit within the plasma region. For nonlinear simulations, these conditions are not realistic and numerically demanding, as the fast dynamics drive current sheets near the plasma edge which are very difficult to resolve. This is especially true for the violent kink instabilities at the $q = 2$ rational surface which have been modelled. In order to resolve this issue for a nonlinear study, the numerical and diffusive parameters are modified to the values shown in Table 6.1.

In order to dissipate sub-grid resolution current sheets that form during the

Table 6.1: Diffusive and grid resolution parameters used in nonlinear external kink simulations. The Ψ dependent step function profiles sharply transition from the lower to upper limit of their ranges at the plasma boundary.

Parameter	Range	Dependence
$\chi_\parallel$ $[\mathrm{m}^2 \cdot \mathrm{s}^{-1}]$	$68.9 - 2.18 \times 10^9$	Spitzer-Haerm
$\chi_\perp$ $[\mathrm{m}^2 \cdot \mathrm{s}^{-1}]$	$1.45 - 2.179 \times 10^3$	Step function
$D\parallel$ $[\mathrm{m}^2 \cdot \mathrm{s}^{-1}]$	847.0	Constant
$D_\perp$ $[\mathrm{m}^2 \cdot \mathrm{s}^{-1}]$	$0.847 - 847.0$	Step function
η $[\Omega \cdot \mathrm{m}]$	$1.06 \times 10^{-7} - 3.38 \times 10^{-4}$	Spitzer-like
η_{num} $[\Omega \cdot \mathrm{m}^3]$	$1.06 \times 10^{-12} - 3.38 \times 10^{-9}$	Spitzer-like
μ $[\mathrm{kg} \cdot \mathrm{m}^{-1} \cdot \mathrm{s}^{-1}]$	$9.37 \times 10^{-8} - 2.96 \times 10^{-4}$	Spitzer-like
μ_{num} $[\mathrm{kg} \cdot \mathrm{m} \cdot \mathrm{s}^{-1}]$	$9.37 \times 10^{-13} - 2.96 \times 10^{-9}$	Spitzer-like
n_{rad}	120	-
n_{pol}	150	-
n_{plane}	64	

penetration of the kink into the hot core region, a Spitzer-like profile is used for the plasma resistivity, viscosity and their equivalent hyper-diffusive terms. The parallel conductivity is set based on the Spitzer-Haerm conductivity, such that $\chi_\parallel = 2.18 \times 10^9$ $\mathrm{m}^2\mathrm{s}^{-1}$ at the magnetic axis. Similar to the set up in Section 3.2, the simulation domain does not include a limiter, or x-point, such that there are closed flux surfaces outside of the plasma. Therefore, the edge region does not replicate the transport physics of the vacuum region expected in a real experiment. In order to account for this non-physical effect, a relatively large perpendicular diffusion is used in the vacuum region to approximate the physics of a limiter around the plasma, where transport out of the simulation domain should be high. In the plasma region, the perpendicular particle and thermal diffusion coefficients are spatially constant. Because the parallel momentum equation is neglected in this study, as described in Section 2.6.2, a parallel particle diffusivity is used as a proxy for the parallel mass transport. Heat and particle sources are used to maintain the density and temperature profiles over the timescale of the simulations.

The Ohmic decay of the plasma current, $\eta(j_{\mathrm{vc}} - j_{\mathrm{v}})$ in equation 2.51, is applied only after the initial kink instability has begun to saturate, in order to preserve the current profile during the linear phase. A more realistic bootstrap current profile cannot be evolved from the initial conditions because the initial pressure and bootstrap current density profiles have not been prescribed self-consistently. The decay of the plasma current exacerbates resistive instabilities. As a result, the simulations can be considered a worst case scenario for the dynamics, as the enhanced resistivity should lower the stability threshold for nonlinearly triggered modes [123].

Regarding resolution parameters, all simulated cases use a flux aligned grid with 120 radial, and 150 poloidal grid elements. In the toroidal direction, 64 poloidal

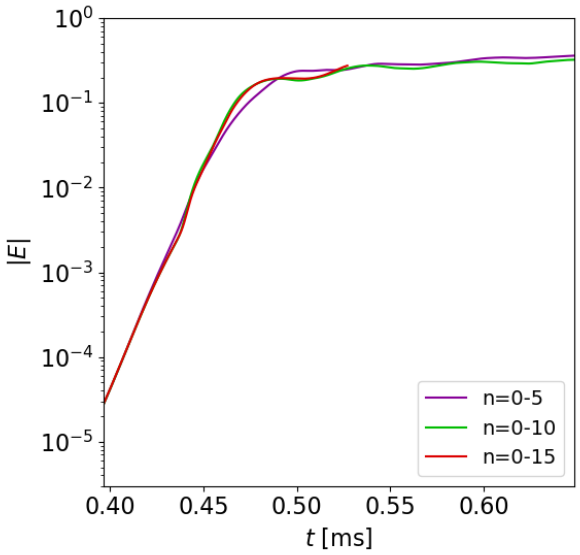

Figure 6.1: Toroidal resolution scan for the tokamak approximation that has the most violent dynamics. The dynamics of the $n = 1$ mode, which dominates the instability, is very well converged, when using 10 toroidal harmonics.

planes are used to capture the simulated toroidal harmonics, up to $n = 15$. A toroidal resolution scan, shown in Figure 6.1, considering the evolution of the magnetic energies in the equivalent tokamak approximation demonstrates that the $n = 1$ toroidal harmonic that leads the instability is sufficiently resolved when 10 toroidal harmonics are included. The main simulations in this study therefore use this resolution.

6.1.2 Equilibria of interest

The QA stellarator considered for this study, has a relatively small external rotational transform, such that the plasma current, I_p, of its virtual current approximation remains high at 8.25 MA. In [85], it has been shown that the external field stabilises the $n = 0$ mode, leading to qualitatively different nonlinear dynamics. The equivalent tokamak would need to be actively controlled in order to avoid a vertical displacement event (VDE), while the QA device is passively stable as a result of the magnetic cage produced by the external field. Vertical stability is not considered in this study, as the focus is on the nonlinear violence of the external kink mode present in the QA stellarator, and whether it is sufficiently suppressed by the modest external rotational transform applied in the device.

With respect to the dynamics of the simulated external kink mode, it will be shown that the virtual current approximation of the stellarator is more stable than the equivalent tokamak. However, the dynamics remain violent, leading to a severe loss of confinement. For this reason, several additional simulations were run at

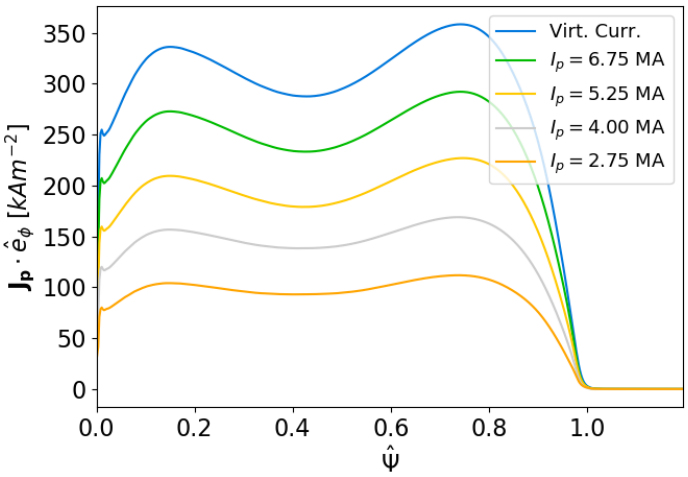

Figure 6.2: Plasma current density of the simulated cases. The I_p = 8.25 MA (Virt. Curr.) case corresponds to the approximation of the original stellarator equilibrium from Section 5.4. The others are conceptual equilibria, that are used to vary the external rotational transform, while fixing all other equilibrium parameters. They maintain the same normalised plasma current density profile as in the original approximation.

reduced plasma currents corresponding to an increased external rotational transform. The same equilibrium is used, preserving the safety factor, pressure and total current profiles from Figure 5.11 (d-f), while reducing I_p. Approximately the same normalised plasma current density profile is maintained as in the original stellarator. The plasma current density of the modified equilibria are shown in Figure 6.2, comparing with the original virtual current approximation from Section 5.4 in blue. Six cases have been simulated at plasma currents ranging from 11.5 MA, in the equivalent tokamak approximation, to 8.25 MA, approximating the original QA configuration, and four conceptual cases with lower current at 6.75, 5.25, 4.00 and 2.75 MA respectively.

The full parameter space from the equivalent tokamak to a virtual current approximation of a zero net current carrying stellarator is explored to give an intuition of when the external kink is nonlinearly stabilised. It should be noted that the modified equilibria at lower plasma currents do not have a known corresponding 3D equilibrium. They are conceptual cases generated for the purpose of this study, to isolate the effect of the external rotational transform, keeping all other variables in the equilibrium the same. If the parameter space was studied using real configurations, it is likely that the amount of 3D shaping would strongly increase as the plasma current reduces. Such non-axisymmetric shaping is not accounted for in the stellarator expansion ordering that the virtual current model is based on, and so this is an important limitation of the results of this study. This has to be kept in

Table 6.2: Growth rates and saturation times for different plasma currents.

Case	$\gamma_{n=1}$	t_{sat} [ms]	t_{offset} [ms]
Tokamak	4.367×10^4	0.445	0.075
$I_{\text{p}} = 8.25$ MA	1.840×10^4	1.134	0.192
$I_{\text{p}} = 6.75$ MA	8.760×10^3	2.492	0.483
$I_{\text{p}} = 5.25$ MA	3.427×10^3	6.709	1.403
$I_{\text{p}} = 4.00$ MA	3.413×10^2	67.083	13.849
$I_{\text{p}} = 2.75$ MA	-	-	-

mind when interpreting the present study to inform intuition about real devices.

6.1.3 Timescale of dynamics

The dependence of the linear growth rate and time to saturation on the plasma current is shown in Table 6.2. With the modifications to the diffusive parameters described in Section 6.1.1, the structure of the growth rates in the tokamak and virtual current approximation is damped compared to the growth rates observed in Figure 5.13 (b). Even so, the external kink modes remain violently unstable. The growth rates decrease significantly with increasing virtual current, until for the $I_{\text{p}} = 2.75$ MA case, the virtual current approximation becomes linearly stable to external kinks. Some of the plots in this chapter use a normalised time, $\hat{t}$, such that cases can be compared, despite their varying time scales. $\hat{t}$ is normalised by the linear growth rate of the $n = 1$ kink instability, $\gamma_{n=1}$, such that

$$\hat{t} = 1.1769 \times 10^{-6} \, \gamma_{n=1} \, (t - t_{\text{offset}}) \tag{6.1}$$

where the prefactor is the time normalisation to JOREK units, and t_{offset} is used so that, at $t = 0$, all simulated cases have the same magnetic energy in the $n = 1$ mode, which has become linearly unstable.

6.2 Nonlinear evolution of the external kink

6.2.1 Variation of global quantities

In this section, the evolution of the total plasma current and thermal energy in time, as well as the time averaged toroidal magnetic energy spectrum during the nonlinear phase are shown. These global quantities can be used to gain a broad understanding of the nature of the dynamics and how the reduction in plasma current changes the nonlinear evolution. The diagnostics indicate the linearly unstable external kink modes are stabilised with decreasing plasma current. In addition, indications of nonlinear triggering of internal MHD activity are identified. This nonlinear effect is discussed in more detail in subsequent sections.

In the early nonlinear phase, the external kink should lead to similar current dynamics as in a constrained relaxation process [124, 125]. The current profile flattens, redistributing into the vacuum region. As a result, the inductance of the plasma decreases, leading to a current spike. The magnitude of the spike is a reasonable metric for the violence of the initial instability. Figure 6.3 (a) shows the evolution of the normalised plasma current profiles as a function of time. As expected, in the equivalent tokamak approximation, there is a large current spike as the instability saturates. With larger external rotational transform, the instability becomes milder and the timescale to saturation increases. This means that the amplitude of the current spike reduces, and the dynamics begin to enter a hybrid timescale, where resistive effects can dissipate the spike in current at the plasma edge. For this reason, the current spike is not as pronounced as I_p decreases. Eventually for the $I_\mathrm{p} = 4.00$ MA case, the initial kink instability becomes so mild that a current spike is not observed, and the current resistively decays.

The change in thermal energy stored in the plasma volume, E_therm, over time is plotted for all cases in Figure 6.3 (b). In most cases the thermal energy does not change significantly in the simulated time frame. This is because the dynamics are strongest in the outer region of the plasma, while most of the thermal energy is stored in the core, because of the assumed parabolic pressure profile, as shown in Figure 5.11. Somewhat surprisingly, the $I_\mathrm{p} = 6.75$ MA case loses the most thermal energy. Note that this is partly due to the longer timescale of this simulation, compared with the higher plasma current cases, as shown by the definition of $\hat{t}$ in equation 6.1. The increase in thermal losses is too large to be due to the longer timescale of the simulated instability alone. The behaviour at $I_\mathrm{p} = 6.75$ MA is expected to be because of enhanced transport inside the plasma due to overlapping internal modes as discussed in Section 6.2.3. At $I_\mathrm{p} = 4.00$ MA, the thermal energy does not decay significantly. It is shown in Section 6.2.4 that confinement is maintained over most of the plasma region in this case.

The time averaged MHD activity can be visualised by considering the magnetic energy spectra during the nonlinear phase, as shown in Figure 6.4. Most of the simulated cases have a very broad magnetic energy spectrum which remains large up to the $n = 10$ mode. This is to be expected given that the edge q being modeled is below 2, and is therefore highly unstable. In the tokamak case especially, all the simulated toroidal harmonics are linearly unstable. As I_p decreases, more modes are stabilised, such that the $n = 1$ component becomes the driving mode in the nonlinear saturation. While the energies of the $n = 1$, 2 and 3 modes reduce with the plasma current, the higher toroidal harmonics remain relatively constant during the nonlinear phase. This provides further evidence that these toroidal harmonics are not just driven by the low n external kink modes, and the stability threshold of internal modes has been crossed. This is in particular true for the $n = 4$ and 5 modes, as discussed in Section 6.2.3, which have a localised peak in the magnetic energy spectrum in Figure 6.4. The $I_\mathrm{p} = 4.00$ MA case shows a significantly lower saturated energy than the higher current cases. This seems to be because the initial

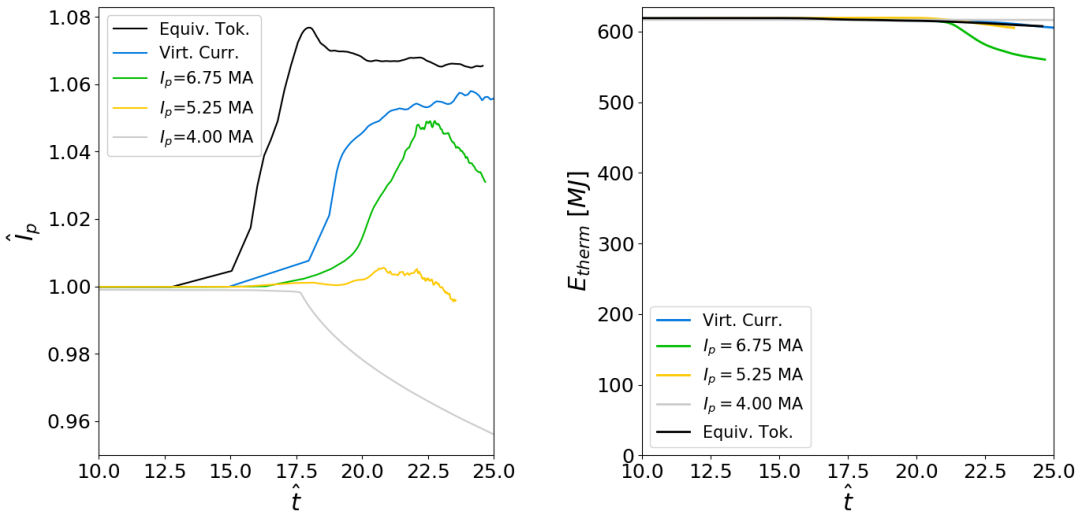

(a) (b)

Figure 6.3: Normalised plasma current (a) and thermal energy (b) during the evolution of the external kink. The $I_\mathrm{p} = 6.75$ MA case has a significantly increased transport of thermal energy out of the plasma.

kink instability is not violent enough to trigger MHD activity at internal surfaces.

6.2.2 General dynamics

Time traces of the energy and pseudocolour plots of the temperature in normalised units are shown in Figure 6.5 for the unstable cases that were simulated. Contours of density are also overlaid on the temperature plots. The initial saturation of the external kink is lead by the low toroidal harmonics. As the higher harmonics continue to grow and saturate, the outer region of the plasma becomes increasingly chaotic, leading to a loss of thermal energy.

In the equivalent tokamak approximation, the $n = 2$ mode leads the instability. This can be expected from the linear growth rates observed in Figure 5.13 (b) where the $n = 2$ mode has a larger growth rate than the $n = 1$ instability. Soon after its saturation, the $n = 2$ perturbation is suppressed by the $n = 1$ mode, as can be seen from the change in the density contours in Figure 6.5 (b) and (c), which trace the (4, 2) and (2, 1) mode structures that form. The saturation of the $n = 1$ mode is followed by a relatively stationary phase where the higher toroidal harmonics continue to grow, and saturate. The combination of multiple toroidal harmonics that are all linearly unstable leads to significant loss of confinement, and heat transport through perpendicular convection, and parallel conduction in the outer region of the plasma.

As I_p is decreased, the higher toroidal harmonics are stabilised first, such that the $n = 1$ mode initially drives the other harmonics. This can be seen to lead to

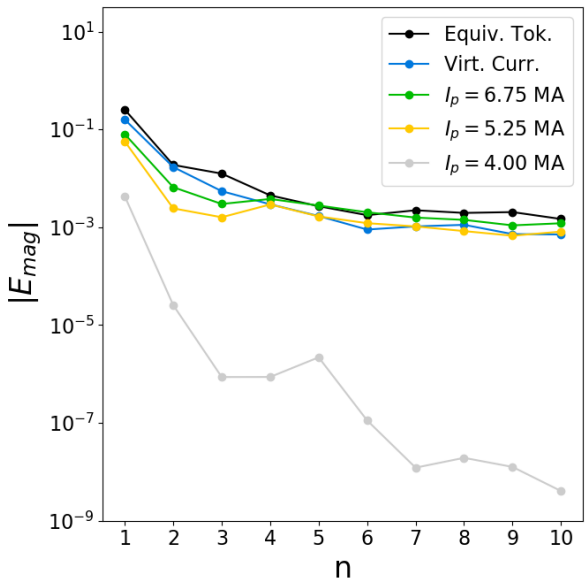

Figure 6.4: Magnetic energy spectrum during the nonlinear phase in which the external kink has saturated.

similar, but milder dynamics in the virtual current case with $I_\mathrm{p} = 8.25$ MA. The $I_\mathrm{p} = 6.75$ MA and 5.25 MA cases follow the same initial trend, such that the $n = 1$ kink is milder. However the $n = 4$ and $n = 5$ modes play a larger role after the initial saturation, especially in the $I_\mathrm{p} = 6.75$ MA case. Here, it can be seen that there is a transient peaking of the $n = 4$ and $n = 5$ modes around $t = 2.9$ ms. This indicates that the kink triggers further internal instabilities led by these modes. A combination of this effect and the longer timescale of the instability lead to larger thermal losses by the end of the simulation, as can be seen from the constricted temperature plot in the $I_\mathrm{p} = 6.75$ MA case at $t = 3.178$ ms. Despite the longer time scale, the thermal losses in the $I_\mathrm{p} = 5.25$ MA case are smaller. This indicates that the combined internal and external instabilities are stronger at $I_\mathrm{p} = 6.75$ MA.

Compared to the other simulated cases, the dynamics at $I_\mathrm{p} = 4.00$ MA are much milder. Comparing the density contours in Figure 6.5 (r) with the initial contour, shown in light blue, it can be seen that the initial (2, 1) kink saturates with a relatively small deformation of the plasma. The internal perturbations led by the $n = 5$ mode close to the plasma edge do not penetrate significantly into the plasma region, or lead to secondary deformations of the plasma edge. The time scale of the $I_\mathrm{p} = 4.00$ MA case is an order of magnitude longer than at $I_\mathrm{p} = 6.75$ MA, with much milder thermal losses that are unlikely to lead to a disruption without additional contributions to the destabilisation of the plasma that have not been modeled.

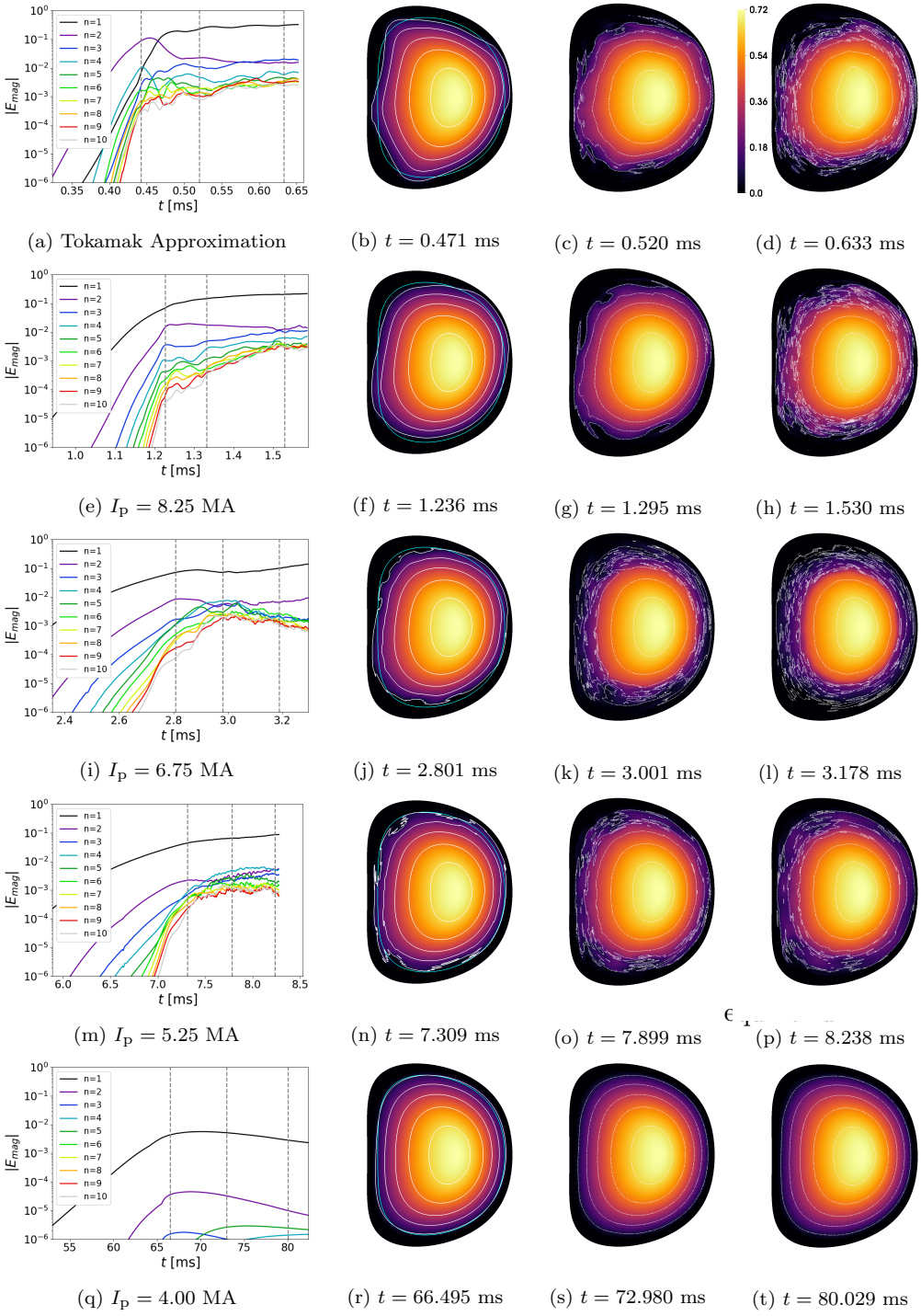

(a) Tokamak Approximation (b) $t = 0.471$ ms (c) $t = 0.520$ ms (d) $t = 0.633$ ms

(e) $I_\mathrm{p} = 8.25$ MA (f) $t = 1.236$ ms (g) $t = 1.295$ ms (h) $t = 1.530$ ms

(i) $I_\mathrm{p} = 6.75$ MA (j) $t = 2.801$ ms (k) $t = 3.001$ ms (l) $t = 3.178$ ms

(m) $I_\mathrm{p} = 5.25$ MA (n) $t = 7.309$ ms (o) $t = 7.899$ ms (p) $t = 8.238$ ms

(q) $I_\mathrm{p} = 4.00$ MA (r) $t = 66.495$ ms (s) $t = 72.980$ ms (t) $t = 80.029$ ms

Figure 6.5: Energies of toroidal harmonics, and pseudocolour plots of normalised temperature, during the dynamics. Contour lines of the number density at 10% to 90% of the initial peak value are also shown. The initial 10% contour is given in light blue in (b), (f), (j), (n) and (r) to show the plasma deformation.

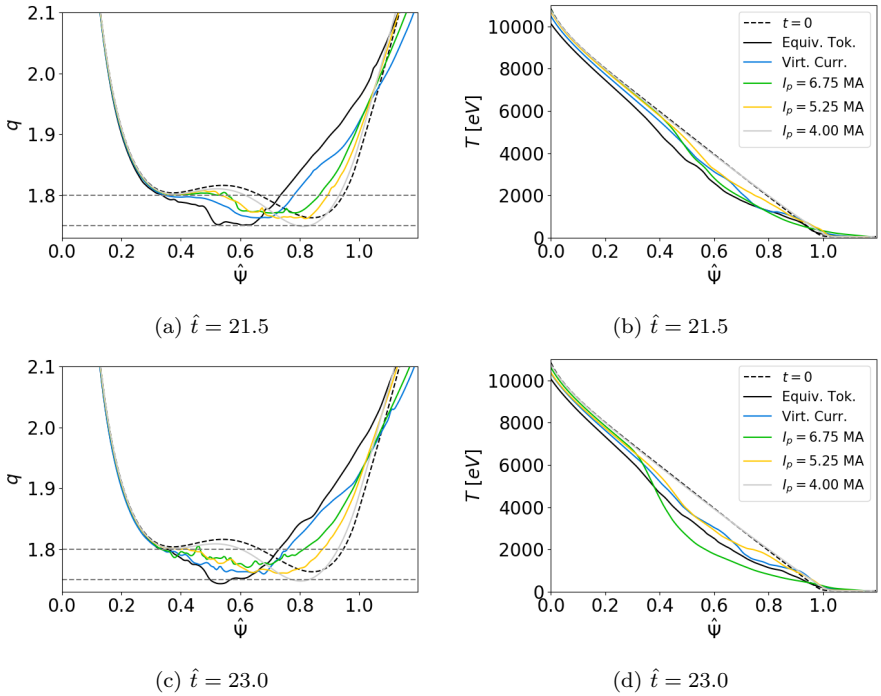

(a) $\hat{t} = 21.5$ (b) $\hat{t} = 21.5$

(c) $\hat{t} = 23.0$ (d) $\hat{t} = 23.0$

Figure 6.6: q profile (a and c) and temperature profiles (b and d) averaged on the $n = 0$ normalised poloidal flux, $\hat{\Psi}$, surfaces at $\hat{t} = 21.5$ (a-b) and $\hat{t} = 23.0$ (c-d). Island structures can be observed in the profiles, indicating internal modes have been triggered by the external kink. Flat regions are observed in q profiles, around the $q = 1.8$ and $q = 1.75$ surfaces.

6.2.3 Internal modes

It is possible to observe internal modes as island structures in the surface averaged radial plots of temperature, shown in Figure 6.6 (b) and (d). Magnetic islands cause a local flattening of the temperature profile around rational surfaces, through parallel thermal transport [126]. Two time points are shown during and after the strong MHD activity observed for the $I_\mathrm{p} = 6.75$ MA case. The surfaces that are averaged over are defined by the $n = 0$ flux surfaces. The q profiles shown in Figure 6.6 (a) and (c) are therefore only approximate, but give an indication of where the rational surfaces are located. Island structures can be inferred from the temperature plots around points where the profiles are partially flattened. The q profile suggests that the (9, 5) and (7, 4) rational surfaces are important in the dynamics.

It can be seen that the q profile is flattest for the $I_\mathrm{p} = 6.75$ MA case both during and after the dynamics around the $q = 1.8$ and 1.75 rational surfaces. The external kink redistributes the plasma current, moving the peak in local current density at the plasma edge both into the plasma and out into the vacuum. Overall, this leads to a flattening of the q profile. In the tokamak case, redistribution occurs up to

the region of strong negative shear in the plasma core, where the q profile remains unchanged. Based on the q profiles in Figure 6.6, it appears that the radial extent of this process reduces with I_p, as the kink dynamics become milder.

For the $I_\mathrm{p} = 6.75$ MA case, the redistributed current acts to mostly flatten the outer region of negative shear ($0.6 < \hat{\Psi} < 0.8$) in the q profile. This allows the $n = 4$ and 5 modes to dominate in the mid-region of the plasma, such that their island structures overlap. As shown in the temperature plots from a later point in time, the temperature profile relaxes significantly after this point, while in the other cases, the island structures seem to be too far apart to overlap and form ergodic regions. In such a way, less thermal energy is transported out of the plasma.

The significance of the (9, 5) and (7, 4) modes can also be shown using pseudo-colour plots of the poloidal flux, as in Figure 6.7. The contours show the $n = 4$ and $n = 5$ components of the flux for the equivalent tokamak, $I_\mathrm{p} = 6.75$ MA, and $I_\mathrm{p} = 5.25$ MA cases. All three cases show (7, 4) and (9, 5) structures, indicating that internal modes have been triggered. In Figure 6.7 (c) and (f), which show the equivalent tokamak case, (8, 4) and (10, 5) structures can also be observed, suggesting that the (2, 1) external kink still interferes with the internal modes.

The modes that are triggered could be either resistive double tearing modes, or infernal modes. There is typically a transition between the two modes depending on how close the plasma is to the ideal stability threshold [127]. The modes are normally distinguished by differing dependencies of the linear growth rate on resistivity, which cannot be analysed for the nonlinearly triggered modes in this paper. It can be seen in Figure 6.5 that at $I_\mathrm{p} = 6.75$ MA, the $n = 4$ and $n = 5$ energies fall during the period where significant thermal energy is lost, indicating that the modes might be pressure driven. This observation and the apparent occurrence of the (7, 4) mode in plasmas that do not seem to have a $q = 1.75$ rational surface give some indication that the nature of these modes might be infernal.

6.2.4 Plasma ergodisation

Similar to the analysis in Chapter 3.4.3, the connection length of magnetic field lines to the simulation boundary can be used as a metric for the loss of confinement. Field lines are traced for a maximum of 100 toroidal turns around the torus, or until they connect with the simulation boundary. The connection length is determined by the harmonic mean of 1000 poloidal sample points on each of 51 radial surfaces, defined by the $n = 0$ component of the poloidal flux. The computed connection length is plotted over time in Figure 6.8 for the equivalent tokamak, $I_\mathrm{p} = 6.75$ MA and $I_\mathrm{p} = 4.00$ MA cases. Values are normalised by the connection length in the plasma core.

The dynamics is split into two phases. The initial ergodisation of the kink is characterised by a sudden loss in confinement near the plasma edge. For cases with larger I_p, this initial stochastisation driven by the external kink penetrates further into the core region. Later in time, there is a gradual loss of confinement further

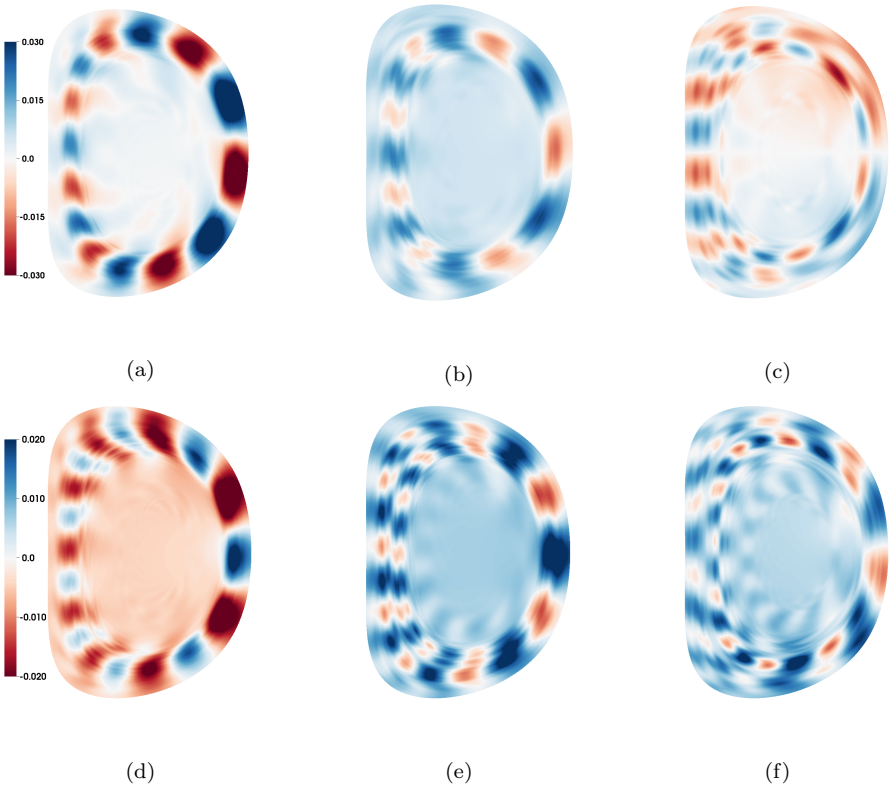

Figure 6.7: Pseudocolour plots of the $n = 4$ (a-c) and $n = 5$ (d-f) components of the poloidal flux perturbation for the $I_\mathrm{p} = 5.25$ MA (a and d), $I_\mathrm{p} = 6.75$ MA (b and e) and tokamak approximation (c and f) cases, at $\hat{t} = 22.48$. (7, 4) and (9, 5) internal modes have been triggered in all cases.

inside the plasma as MHD activity grows on the internal rational surfaces. After the strong internal modes in the $I_\mathrm{p} = 6.75$ MA case, it can be seen that there is a partial recovery of the internal surfaces. It is expected that if the other simulations were continued further, a similar recovery may be observed once a comparable amount of thermal energy is lost, and the drive for the internal modes diminishes. At $I_\mathrm{p} = 4.00$ MA, the initial kink only penetrates up to $\sqrt{\hat{\Psi}} \approx 0.95$, and does not lead to a complete loss of confinement in this region. The subsequent internal modes break up the flux surfaces close to the plasma edge, but confinement is maintained over most of the plasma. Later in time, the edge current density gradient and total plasma current reduce due to resistive effects. This causes the edge safety factor to rise, and the drive for the instability to relax. As such, the energy in the toroidal perturbations decays, and the associated magnetic islands shrink, there is a partial recovery of confinement in the simulation domain, such that losses are mostly in the vacuum region.

Poincaré plots are shown in Figure 6.9 at $\hat{t} = 23.0$. A dominant (2, 1) island structure is observed in all cases. In the equivalent tokamak approximation, the

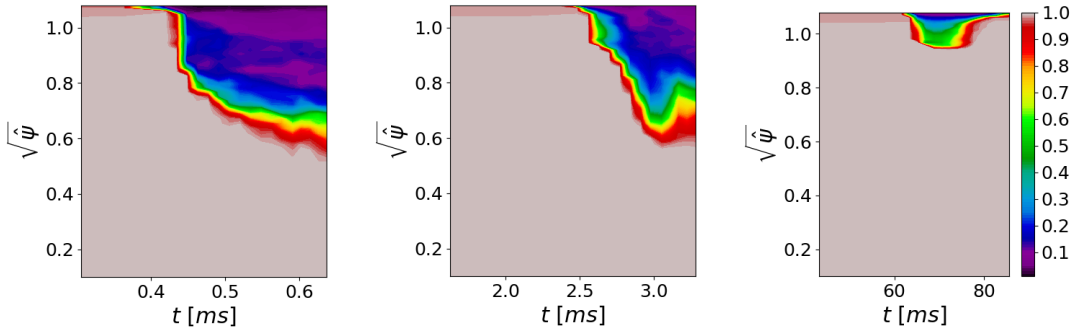

(a) Tokamak Approximation (b) $I_p = 6.75$ MA (c) $I_p = 4.00$ MA

Figure 6.8: Plots of normalised connection length to the simulation domain boundary at the end of the simulated timeframe.

island structure is deformed by the remnants of the sub-dominant (4, 2) mode. Relatively little structure can be observed in the region where confinement is lost. This is because field lines very quickly connect to the simulation boundary via the large (2, 1) magnetic islands outside the plasma.

In the equivalent tokamak, the radial extent of the (2, 1) instability is larger than in cases with lower plasma current. This can be seen from the visible kink in the core flux surfaces compared to the virtual current cases. The (2, 1) deformation of the plasma reduces with I_p. In the $I_p = 6.75$ MA case, it can be seen that there is more significant stochastisation in the mid-region of the plasma than in the equivalent tokamak, as a result of the internal modes discussed in Section 6.2.3. The initial (2, 1) deformation of the plasma reduces with I_p.

Similar to the connection length plots, the Poincaré plot of the $I_p = 4.00$ MA case show relatively little deformation of the plasma. Large islands are still apparent, but they are much less ergodic, which leads to better confinement of the field lines within the external (2, 1) island structure. Smaller (7, 4) and (9, 5) island chains have been identified just inside the plasma region, as shown in Figure 6.10, but they remain at low enough energies to only mildly degrade the confinement in the outer region of the plasma.

6.3 Discussion

In this chapter, the virtual current model has been used to model external kinks with JOREK nonlinearly in axisymmetric approximations of a QA configuration. It has been shown that, while the nonlinear dynamics of the tokamak approximation and stellarator are known to be different due to the vertical stability of the latter, the external kink remains violently unstable for the simulated QA configuration. It can be expected that such strong MHD activity will lead to a significant loss of confinement.

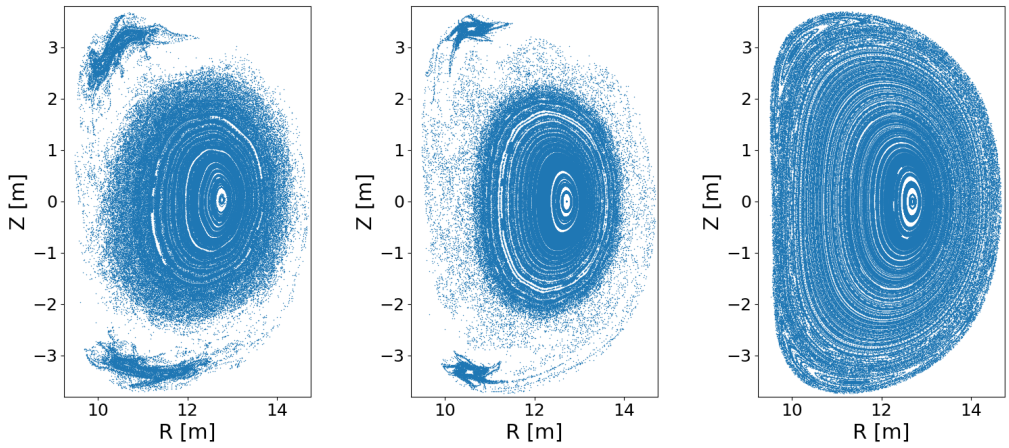

(a) Tokamak Approximation (b) $I_\mathrm{p} = 6.75$ MA (c) $I_\mathrm{p} = 4.00$ MA

Figure 6.9: Poincaré plots taken at $\hat{t} = 23.0$ for the equivalent tokamak approximation (a), $I_\mathrm{p} = 6.75$ MA (b) and $I_\mathrm{p} = 4.00$ MA case.

To explore the influence of larger fractions of external rotational transform on the nonlinear dynamics, this parameter was artificially increased. While it is acknowledged that the artificial increase of external rotational transform used in this study does not capture all of the 3D effects which are likely to become important as the external contribution to the poloidal field is increased, these qualitative results have been carried out to inform the direction of future studies with a stellarator capable 3D nonlinear code.

In the nonlinear phase, the violence of the initial external mode is reduced with increased contribution of virtual currents to the rotational transform, as measured by the current spike observed in the plasma, and the initial loss in confinement due to the kink instability. Nonlinearly triggered internal modes, in particular for this case the (7, 4) and (9, 5), mean that the loss in confinement can remain large, even after an appreciable external rotational transform has been introduced. This means that the variation of thermal losses with increasing external rotational transform can be non-monotonic. There are cases at large external rotational transform where internal modes are mild, indicating that the initial external modes could lead to a nonlinearly stable state.

Further extensions to this work could consider the original QA device in more detail, exploring further destabilising effects such as impurities introduced from the plasma touching wall structures. However, as this study has shown, the test case considered here is extremely violent, even without these additional destabilising effects. As a result, this particular QA configuration is unlikely to be a candidate for a reactor experiment. This conclusion is unsurprising, as the low edge q was optimistic from a MHD perspective. The fusion community is likely to be interested in more conservative QA configurations, which have been designed with a larger fraction of external rotational transform [11]. As discussed in Section 2.6, it

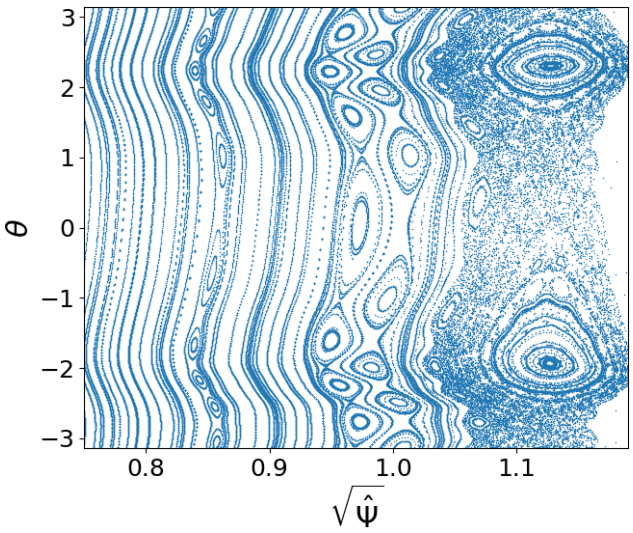

Figure 6.10: Poincaré plot of the plasma edge taken at $\hat{t} = 23.0$ for the $I_p = 4.00$ MA case. Multiple (9, 5) and (7, 4) magnetic island chains near the plasma edge can be observed in line with the multiple rational surfaces (see Figure 6.6).

is unlikely that an axisymmetric approximation will be able to provide high fidelity analysis of such devices, because 3D shaping will become more important. Eventually a non-axisymmetric nonlinear MHD code, will be necessary to look at the detailed dynamics. In the next chapter, developments towards the commissioning of such a code are discussed.

7 Towards nonlinear modelling of stellarators

In this section, the contributions carried out as part of this thesis towards the implementation and testing of a fully non-axisymmetric nonlinear solver in JOREK are outlined. This development was led by Nikita Nikulsin who derived and implemented a stellarator capable reduced MHD model in JOREK, previously tested in the tokamak limit [45, 46]. Several contributions to the testing of this model for stellarator cases were made within this thesis. First, a non-axisymmetric finite element mesh was imported to JOREK from the GVEC equilibrium code, converting to the necessary ansatz for the magnetic field used in the JOREK models. An overview of the process for importing stellarator equilibria to JOREK, articulating the need for an interface to an equilibrium code, is given in Section 7.1. The implementation and validation of the import from GVEC is discussed in Section 7.2. In the next step, the reduced MHD model is verified by designing a linear benchmark based on previous experimental observations on the W7-A stellarator. This case was used to compare the linear growth rates computed by the JOREK reduced MHD model for resistive tearing and ballooning mode cases, against those computed by the full MHD model in CASTOR3D. Reasonable agreement was found between the two modelling approaches, as shown in Section 7.3. The results in this chapter were presented in conference proceedings [49] and published in [47].

7.1 Importing stellarator equilibria to JOREK

The conventional approach for generating equilibria for tokamaks in JOREK, using its in-built Grad-Shafranov solver, will not work for stellarators. The advantage of solving the equilibrium internally, is that equilibrium force balance can be converged in the numerical representation used in JOREK, such that the initial equilibrium condition is ensured. For stellarator equilibria, the development of an in-built equilibrium solver using the magnetic field ansatz in equation 2.26 would require a significant amount of work in itself. This is because the representation of the vector potential makes no assumptions about the magnetic field structure, such as nested flux surfaces, which are normally used to simplify the equilibrium solution space. For this reason, it was decided instead to import stellarator equilibria from existing equilibrium codes, such as GVEC [56].

GVEC is a modern implementation of VMEC, which is being used increasingly to initialise simulation conditions for several codes, such as CASTOR3D,

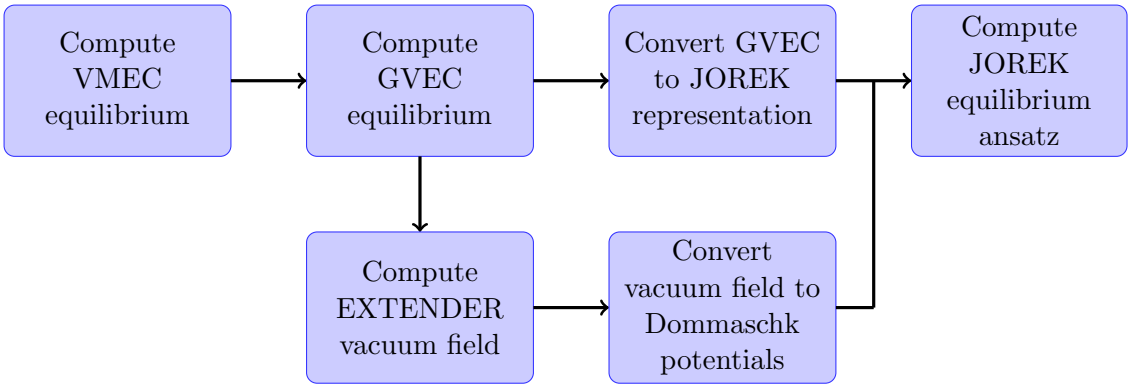

Figure 7.1: Workflow for importing stellarator equilibria to JOREK

and GENE3D. Similar to VMEC, GVEC uses a 2D Fourier series for its poloidal and toroidal directions, such that the representation of the equilibrium flux surfaces and straight field line angle are also given by equations 2.12. One of the main differences between the codes is the radial representation of flux surfaces. GVEC uses a B-spline finite element representation which can handle non-uniform grids, unlike VMEC.

In order to convert from the GVEC field representation to the JOREK ansatz, the steps in Figure 7.1 are necessary. A VMEC computation is currently used as an input to define an initial guess for GVEC. Once GVEC has been appropriately converged, the representation of its flux surfaces are then used to define a flux surface aligned JOREK grid. The total magnetic field is also converted to a representation which can be used to solve for the JOREK magnetic field ansatz, as an initial condition for nonlinear simulations. Construction of the magnetic field ansatz also requires knowledge of the vacuum magnetic field, represented as Dommaschk potentials to ensure smoothness [128]. The potentials can be computed from the GVEC equilibrium by first calculating the vacuum field using the EXTENDER code [115], and then converting to Dommaschk potentials.

The challenge when using the workflow in Figure 7.1 is to minimise the error in equilibrium force balance that is introduced by the conversion between the two magnetic field representations. The main contribution to the validation of the workflow which was carried out in this thesis was the implementation and assessment of the GVEC grid and fields imported to JOREK. The methods used to generate the vacuum field and convert to the JOREK ansatz are described in [47]. The implementation and validation of this conversion routine is outlined in the next section.

7.2 Conversion of GVEC equilibria to JOREK

This section describes the implementation of the grid representation for stellarator cases in JOREK, and its validation, using a W7-X test case. The steps in the

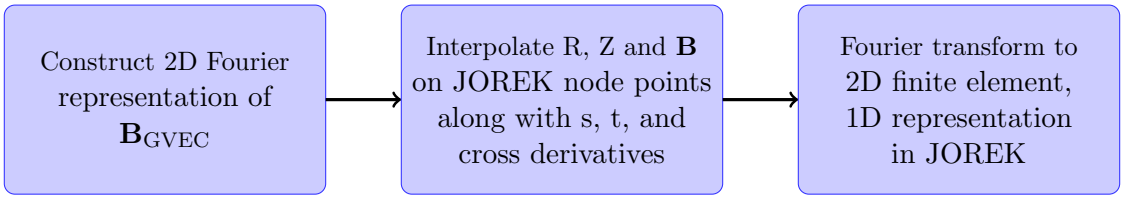

Figure 7.2: Workflow for constructing JOREK grid and representation of $\mathbf{B}_{\mathrm{GVEC}}$

conversion routine are shown in Figure 7.2. In order to model 3D configurations efficiently, the symmetry of the axisymmetric grid in JOREK needs to be relaxed, such that R and Z are dependent on the toroidal coordinate, ζ. This means that, similar to the physics variables that are evolved in time, the geometry now also needs to be represented as a toroidal Fourier series.

A conversion routine has been written to change from the 2D Fourier, 1D radial spline representation in GVEC to the 2D poloidal finite element, 1D toroidal Fourier degrees of freedom, used in JOREK at the desired node locations. In addition to the (R, Z) grid representation of the GVEC grid, the magnetic field $\mathbf{B}_{\mathrm{GVEC}}$ needs to be imported. The s and t derivatives in the JOREK finite element basis, as defined in Section 2.5.2, for $\mathbf{B}_{\mathrm{GVEC}}$ are required to initialise the representation of the JOREK magnetic field. In order to obtain these derivatives, a 2D Fourier representation of $\mathbf{B}_{\mathrm{GVEC}}$ is first constructed, similar to the representation of R and Z. The values of R, Z and $\mathbf{B}_{\mathrm{GVEC}}$ are then interpolated at the desired node locations, taking uniform samples in the toroidal direction. A toroidal Fourier transform is then used to generate the degrees of freedom in JOREK.

By using a sufficiently high resolution, this imported representation of $\mathbf{B}_{\mathrm{GVEC}}$ in JOREK should remain smooth, and able to maintain the force balance that has been converged in the original GVEC calculation. This representation of the GVEC field is then used to initialise the JOREK ansatz for the vector potential in equation 2.26, removing the $\nabla\Omega \times \nabla\Psi_{\mathrm{v}}$ term, which is neglected in the reduced MHD model currently implemented. As described in [48], neglecting this term means that the reduced MHD ansatz in JOREK does not ensure that force balance is maintained. However, the force imbalance is expected to be small, such that a new equilibrium force balance should be found shortly after the imported initial conditions are evolved in time.

Lastly, it should be noted that, when representing such equilibria, ζ does not necessarily need to be equal to the toroidal angle, ϕ, as in the tokamak model, such that the constant ζ planes represented by 2D finite elements remain in a single constant ϕ plane. However, in the current implementation of the grid, $\zeta = \phi$ is assumed. This simplifies the extension of the code to stellarators, as the Jacobian of the volume element in such a coordinate system remains the same as in the

tokamak model, given by

$$\begin{aligned} J &= \frac{\partial \mathbf{r}}{\partial s} \cdot \left(\frac{\partial \mathbf{r}}{\partial \theta} \times \frac{\partial \mathbf{r}}{\partial \phi} \right) \\ &= \left[\frac{\partial R}{\partial s} \frac{\partial Z}{\partial \theta} - \frac{\partial R}{\partial \theta} \frac{\partial Z}{\partial s} \right] (s, \theta, \phi) \, . \end{aligned} \tag{7.1}$$

In the future, this constraint may be removed, if it is found to be beneficial for the practical application of the code.

Toroidal resolution requirements for the GVEC import

Considering equations 2.12, the individual contributions to the 2D Fourier representation of R and Z can be split into multiplications of poloidal and toroidal sinusoidal terms with the same poloidal and toroidal mode numbers. As such, it is possible to represent R and Z as a 1D Fourier series in the toroidal direction which conforms to the original GVEC representation, in the sense that the number of toroidal Fourier harmonics necessary should be the same as in GVEC.

The toroidal resolution requirements for the magnetic field are not so clearly defined, as shown in the following; using the GVEC coordinate system, the covariant basis vectors of the general flux surface coordinate system are given by

$$\mathbf{e}_\mathrm{s} = \begin{bmatrix} \frac{\partial R}{\partial s}\cos(\zeta) \\ \frac{\partial R}{\partial s}\sin(\zeta) \\ \frac{\partial Z}{\partial s} \end{bmatrix}, \mathbf{e}_\theta = \begin{bmatrix} \frac{\partial R}{\partial \theta}\cos(\zeta) \\ \frac{\partial R}{\partial \theta}\sin(\zeta) \\ \frac{\partial Z}{\partial \theta} \end{bmatrix}, \mathbf{e}_\zeta = \begin{bmatrix} \frac{\partial R}{\partial \zeta}\cos(\zeta) - R(s,\theta,\zeta)\sin(\zeta) \\ \frac{\partial R}{\partial \zeta}\sin(\zeta) + R(s,\theta,\zeta)\cos(\zeta) \\ \frac{\partial Z}{\partial \zeta} \end{bmatrix} \tag{7.2}$$

and the contravariant components, ∇s, $\nabla \theta$ and $\nabla \zeta$, can be calculated from the appropriate cross products of these vectors. The magnetic field and vector potential in Cartesian coordinates can then be calculated as

$$\mathbf{B} = \left[\left(\iota(s) - \frac{\partial \lambda}{\partial \zeta} \right) \frac{\partial \Phi}{\partial s} \mathbf{e}_\theta + \left(1 + \frac{\partial \lambda}{\partial \theta} \right) \frac{\partial \Phi}{\partial s} \mathbf{e}_\zeta \right] / J \tag{7.3}$$

$$\mathbf{A} = \left[\Phi(s) \nabla \theta - \lambda \frac{\partial \Phi(s)}{\partial s} \nabla s - \chi(s) \nabla \zeta \right] \tag{7.4}$$

where J is the Jacobian of the coordinate system. It is important to realise that the form of $\mathbf{B}$ and $\mathbf{A}$ are not constrained to the original Fourier representation of R and Z. The multiplication of sinusoidal terms in (7.3) lead to higher harmonics. The Jacobian includes a multiplication of three sinusoidal terms which can lead to mode numbers 3 times as high as the original representation. Division by this term is a nonlinear operation, which makes it unclear how many harmonics are needed in the Fourier representation of the magnetic field. For this reason, the import has been implemented in such a way that the toroidal resolution of the grid

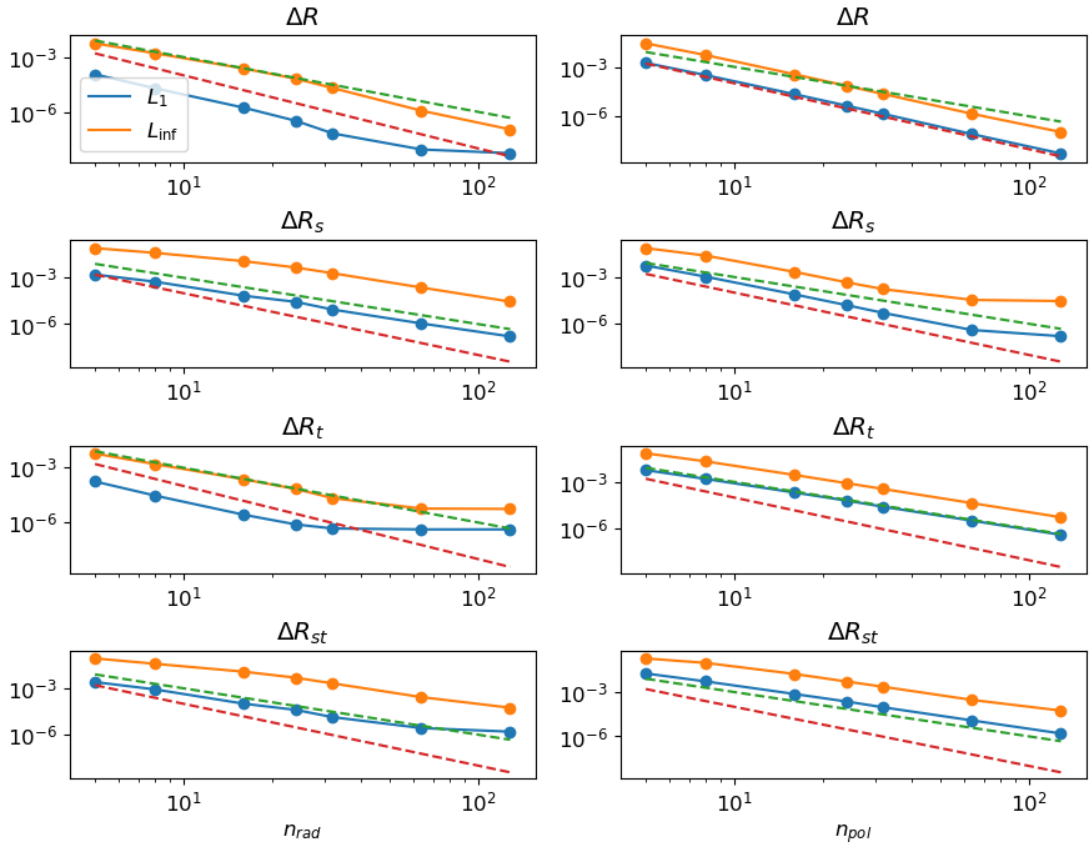

Figure 7.3: L_1 and L_{inf} grid convergence plots for the absolute error in the R coordinate, and its radial, poloidal and cross derivative - R_{s}, R_{t} and R_{st}, respectively - of a W7-X equilibrium. 3^{rd} (green) and 4^{th} order convergence are shown for comparison.

imported to JOREK can be set to an arbitrarily high resolution. For nonlinear MHD simulations, the accuracy of the magnetic field import needs to be assessed carefully.

Grid convergence studies for W7-X

In order to test the performance of the import routines into JOREK, a W7-X equilibrium is converted to the JOREK representation, computing the error in the field variables with the original GVEC representation. As discussed above, the toroidal resolution of the grid should be well resolved in the toroidal direction if the same number of Fourier harmonics are used as in the original GVEC equilibrium. The node points in the finite element mesh are therefore captured to machine precision.

An error can be introduced in the representation of poloidal planes, due to the

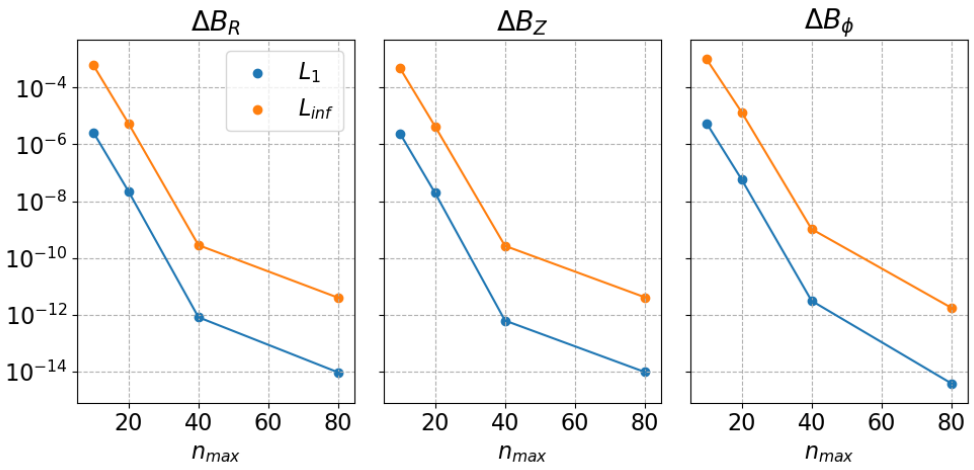

Figure 7.4: L_1 and L_{inf} convergence plots for the absolute error in the magnetic field representation of a W7-X equilibrium with varying resolution. The poloidal and toroidal resolution are multiplied by a constant factor from the base GVEC equilibrium with $m_{\text{pol}} = 12$, $n_{\text{tor}} = 10$ as a function of poloidal and toroidal resolution. It can be seen that a significant increase in the number of modes is necessary to capture the original field accurately.

3rd order Bézier surfaces, which represent the poloidal finite elements. The degrees of freedom used at the nodes for this representation are the $(R,\ Z)$ coordinates, as well as their radial, poloidal and cross derivatives. In order to assess the error, random points are sampled in (s, θ, ϕ) within the plasma domain, using a uniform distribution. After the grid has been imported to JOREK, the same (s, t, ϕ) points are interpolated, comparing the coordinates in R and Z with the original GVEC representation.

The convergence of the L_1 and L_{inf} norms for R and its derivatives are shown in Figure 7.3, for the W7-X test case. If either the radial or poloidal resolution are increased independently, it is expected that the R and Z coordinates should converge to 4th order, while the derivatives will converge at 3rd order. This behaviour is approximately captured in Figure 7.3, such that the grid representation behaves as expected.

In order to assess the resolution requirements for the magnetic field, the error in the 2D Fourier representation of $\mathbf{B}_{\text{GVEC}}$, constructed as part of the conversion routine, is compared with the original representation of the magnetic field, defined by the equilibrium solution and equation 7.3. The results in Figure 7.4 show that indeed more coefficients are needed than are present in the GVEC solution. How important this error is for JOREK simulations is not yet clear. During this thesis, most of the simulations were carried out assuming the same number of toroidal harmonics in the GVEC solution. Even so, physical results were obtained for classical stellarators, as shown in Section 7.3. It remains to be seen whether the

toroidal resolution needs to be increased to obtain an accurate import for optimised stellarators, where the field is more complicated. This issue needs to be tackled as part of future work.

7.3 Initial studies of W7-A resistive instabilities

In this section, an initial linear benchmark of the growth rates of MHD instabilities is carried out to validate the reduced MHD model in JOREK. W7-A was a high aspect ratio, $l = 2$, planar axis stellarator with 5 field periods. The poloidal field was generated by combination of external helical field coils, and Ohmic current drive. The initial validation of JOREK for use with stellarators is carried out on a 5 period, elliptical equilibrium, based on the W7-A stellarator.

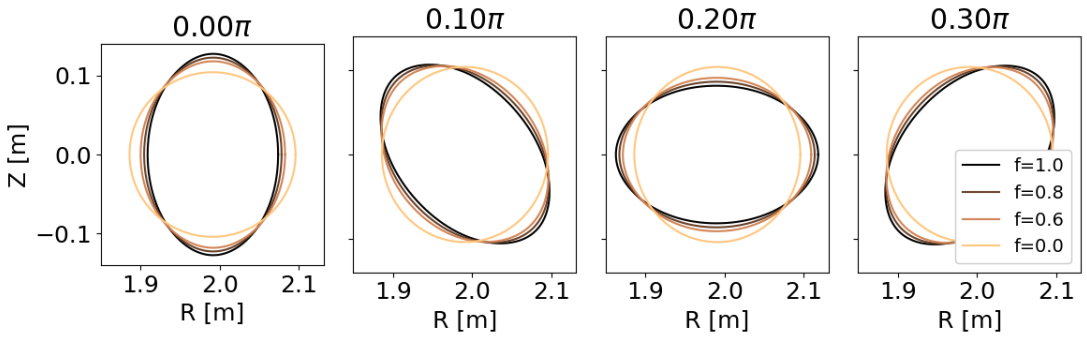

Figure 7.5: Flux surfaces for W7-A equilibria varying the external rotational transform.

The simple design of W7-A makes it possible to vary the fraction of external rotational transform by modifying the elliptical deformation of the plasma, as shown in Figure 7.5. In such a way, the external rotational transform can be controlled using only the $(m = 1, n = 1)$ Fourier coefficients of R and Z on the boundary. The maximum external rotational transform, ι_{ext}, is approximately 0.23 [32]. W7-A was able to produce arbitrary elliptical equilibria between this extremum and the axisymmetric tokamak case. To generate this spectrum of equilibria within VMEC, the $(m = 1, n = 1)$ Fourier coefficients of the boundary representation can be varied using

$$R^{\text{C}}_{\text{m=1, n=1}} = f R^{\text{C, } \iota_{\text{ext}} \approx 0.23}_{\text{m=1, n=1}}, \tag{7.5}$$

$$Z^{\text{S}}_{\text{m=1, n=1}} = f Z^{\text{S, } \iota_{\text{ext}} \approx 0.23}_{\text{m=1, n=1}}, \tag{7.6}$$

where $0 < f < 1.0$, and R^{C}_{mn} and Z^{S}_{mn} represent the fixed boundary Fourier coefficients of the up-down symmetric equilibrium being computed.

Early experimental work assessed the dynamics of resistive tearing modes on W7-A for the same current density profile, and an increasing fraction of external

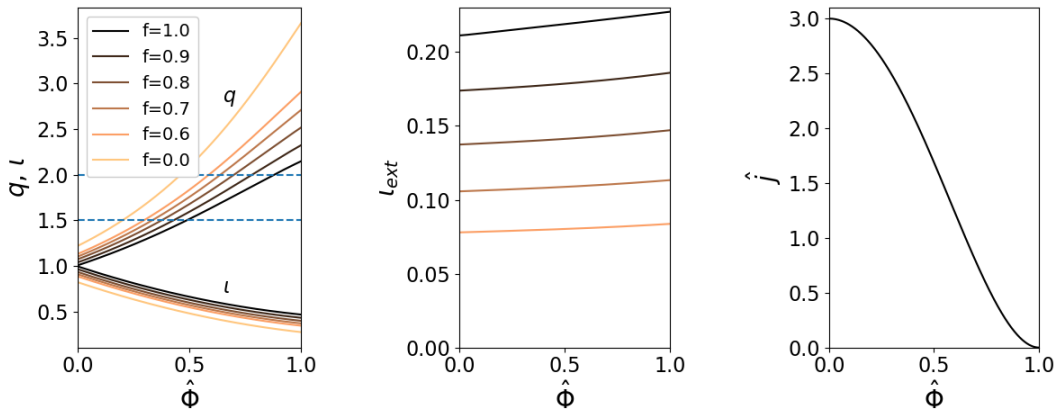

(a) (b) (c)

Figure 7.6: Safety factor profile (a), external rotational transform (b), and normalised current density profile (c) for a low β, W7-A test equilibria. Note that the external rotational transform shown is only approximate, as it is computed by converging vacuum equilibria in VMEC for the prescribed plasma boundary.

rotational transform [32]. It was found that for $\iota_{\text{ext}} \approx 0.15$, (2, 1) tearing modes, which could lead to disruptions, were stabilised [32]. The basic effect that produces this stabilisation has little to do with 3D effects. As shown in in Figure 7.6, the increased external rotational transform decreases the safety factor on axis, shifting the unstable $q = 2$ surface closer to the plasma edge. Consequently, the (2, 1) tearing mode saturates at a lower amplitude, due to the lower current density gradient at the rational surface, and higher wall stabilisation.

Similar equilibria to these experiments can be generated in VMEC. Because the temperature profile of the initial experiments is not exactly known, a cubic current profile given by

$$j(s) = 3 - 6s + 3s^2, \tag{7.7}$$

has been used with a similar total plasma current to the original device, $I_{\text{p}} = 17.5$ kA.

This approximation generates safety factor profiles that are close to that of the original study. These equilibria are tested for linear stability in CASTOR3D. The growth rate of the (2, 1) tearing mode is shown in Figure 7.7. The tearing modes are linearly stabilised at $\iota_{\text{ext}} \approx 0.15$ - the fraction of external rotational transform that is expected from the experiment.

The generated equilibria are a useful first test case for full 3D nonlinear MHD simulations, because they require relatively low toroidal resolution. For the linear validation, the W7-A equilibrium with $f = 0.6$, or equivalently $\iota_{\text{ext}} = 0.08$, was used. Resistivity and β scans were carried out to ensure that the physical trends observed in both codes were consistent. To increase β, a linear pressure profile

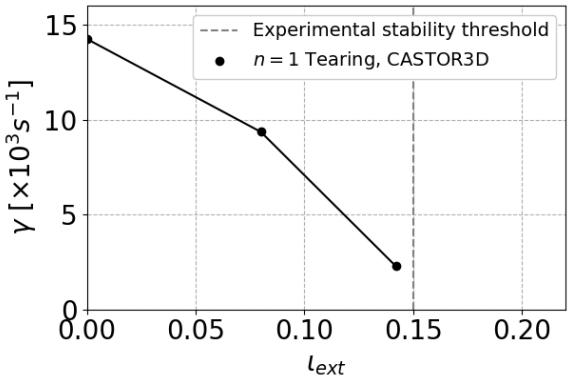

Figure 7.7: Linear growth rates for tearing mode instabilities observed in CASTOR3D. The resistivity in these results is 1.9832×10^{-6} Ωm with a constant pressure and density at 1 Pa and 1×10^{20} m^{-3}, respectively. The observed stabilisation of the tearing mode corresponds approximately to the experimental value.

$p(s) = p_0(1-s)$ was imposed, varying p_0 from 1 Pa to 65 kPa, while preserving the q profile for the equilibrium, shown in Figure 7.6. At high β, preserving the q profile does not lead to experimentally relevant equilibria, as the Ohmic current profile is not preserved, but the equilibria can still be used for this numerical verification study. Modifying p_0 varies β from approximately 0 to 1.47%. The modification of the equilibrium plasma axis, observed both in GVEC and JOREK after the reduced MHD ansatz is applied is shown in Figure 7.8 (a). The consistency in the axis location provides some indication that the import of the GVEC equilibrium is sufficiently accurate for the linear benchmark.

During this β scan, high n, resistive ballooning modes were observed with increasing p_0. The observed $n = 10$ ballooning mode was included in the comparison of JOREK with CASTOR3D. The linear benchmark is shown in Figure 7.8 (b) for both the $n = 1$ tearing mode and $n = 10$ ballooning mode. Reasonable agreement in both the growth rate and physical trends is obtained. The largest error is obtained for the tearing mode where it is expected that neglecting parallel flow could lead to a larger error in the growth rate of the observed mode.

7.4 Discussion

The implementation and validation of a non-axisymmetric grid import from GVEC, and the design and linear benchmarking of a W7-A test case, have assisted the development of a nonlinear stellarator MHD model in JOREK. The results of this chapter validate the linear results of the reduced MHD model for both current and pressure driven modes in classical stellarators.

Of course, the main focus of the fusion community at the moment centres on

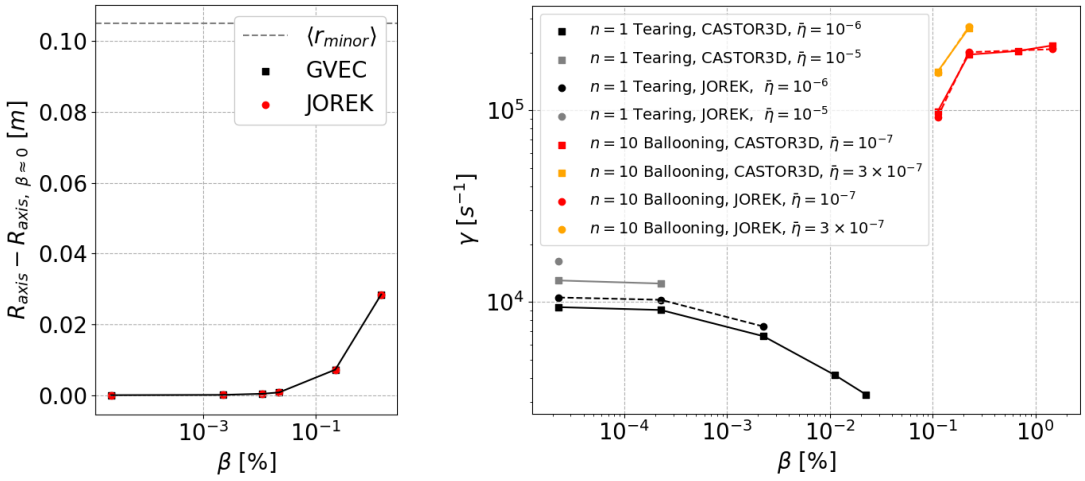

(a) (b)

Figure 7.8: Modification of the R coordinate of the magnetic axis (a) in the $\phi = 0.0$ plane in JOREK and GVEC, as a function of β. Growth rates observed in CASTOR3D and JOREK for resistive tearing and ballooning modes (b). Reasonable agreement is obtained at varying resistivity and β for both modes.

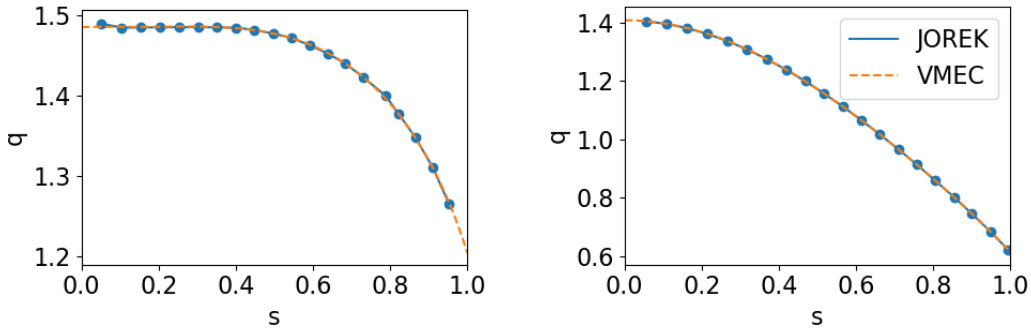

(a) (b)

Figure 7.9: Comparison of q profiles obtained with JOREK and VMEC for W7-X (a) and LHD (b).

optimised stellarators. These devices have much stronger toroidal shaping, and significantly larger external rotational transform than the devices simulated thus far. In such a way, they require additional validation work in their own right. Attempts have already been made to import W7-X and Large Helical Device equilibria to JOREK. The correct q profile is obtained for these equilibria over most of the plasma volume at relatively low toroidal resolution in JOREK, as shown in Figure 7.9. Although more work is necessary to validate these test cases for nonlinear modelling, first linear benchmarks can be considered in the near future.

8 Conclusions and Outlook

Three separate nonlinear modelling approaches have been developed and used as part of this thesis work. In chronological order, the virtual current model used in Chapters 5 and 6 to model stellarators axisymmetrically was the first to be explored. This method was developed with the objective of understanding the nonlinear dynamics of quasi-axisymmetric stellarators, as outlined in Section 8.1. The limits in validity of this approach led to the exploration of equilibrium codes in Chapters 3 and 4. This method was used to simulate nonlinearly saturated free boundary ideal MHD modes in stellarators, as described in Section 8.2. In parallel to these developments, contributions were made in Chapter 7 to the implementation and testing of a stellarator capable reduced MHD model, as outlined in Section 8.3. To conclude this thesis, the future work that could be carried forward from these projects is described in Section 8.4.

8.1 Axisymmetric modelling of nonlinear stability of QA stellarators

The initial objective of this thesis was to make use of simple extensions of the nonlinear MHD models within the JOREK code to assess the nonlinear stability limits of quasi-axisymmetric stellarators, which were of interest to the German fusion community at the time. The approach proposed was called the virtual current model, which used an axisymmetric representation of the externally generated helical field of a stellarator to capture some of the effects that an external rotational transform has on the MHD dynamics. While it was shown in Section 2.6 that this model is only expected to be rigorously valid in the limit of the stellarator expansion — a high aspect ratio, low β ordering with a large number of toroidal field periods — it was hoped that this model could be pushed beyond its strict region of validity to provide a first assessment of optimised stellarators. In particular, the nonlinear MHD characteristics of QA devices were of interest.

The virtual current model implementation was tested within its intended region of validity in Section 5.1 and 5.2, before attempting linear validation studies of optimised stellarators. For the core modes observed in W7-X, surprisingly good agreement was found between the virtual current model and full MHD linear codes, as shown in Section 5.3. In Section 5.4, the linear MHD mode structure of an external kink in a QA device with relatively small external rotational transform was reasonably captured. As a result, it was decided to continue simulations into the nonlinear phase.

The simulated equilibrium was originally found during optimisation studies of QA stellarators. It was discarded as a candidate experimental device, because it was feared that the violent external kinks could lead to disruptions, making the experimental proposal impractical for a future reactor concept. The simulated case could nevertheless be experimentally relevant as a QAS relies on a large bootstrap current such that similar unstable conditions could be crossed during the build-up of plasma current, before operational conditions are reached. To confirm the expectation from the linear results, nonlinear simulations were continued to see whether the mode would saturate or nonlinearly trigger further dynamics. The results of the nonlinear simulations indicate that the global external kink modes do indeed lead to violently disruptive MHD dynamics which would be prohibitive for an experiment. Thus a larger fraction of external rotational transform seems necessary for candidate experiments.

At larger fractions of external rotational transform in optimised stellarators, the validity of the virtual current model for such low aspect ratio, high β, strongly shaped devices is limited. For this reason, the results of any simulations applied in this regime must be taken as qualitative. Simulations which artificially simulated the influence of the external rotational transform at higher fractions showed a stabilisation of the nonlinear dynamics only when a significant amount of the plasma current was removed from the device, indicating that the attractive idea of constructing a QA stellarator with a small external rotational transform may not be practical, as similar challenges to disruptions in tokamaks may be encountered.

8.2 Investigation of VMEC for studying free boundary modes in stellarators

The limits in the validity of the virtual current model, and the disruptive nature of the external kink meant that there were not any immediately attractive directions for future work with this approach. For that reason, it was decided to assess the practicality of using the VMEC equilibrium code to model nonlinearly saturated ideal MHD states. This approach had yet to be validated for nonlinear MHD studies of external modes in tokamaks with a comparison to a full nonlinear solver of the time evolution equations. For this reason, the study began with a validation of the physics results previously published by other authors for external kinks and edge harmonic oscillations.

It was shown in Section 3.3 that the simulated ideal external kink, which is linearly unstable to a single low n mode, found good agreement with the nonlinear simulations performed using JOREK. For the simulation of an EHO instability, the two modelling approaches showed more significant disagreement, due in part to the apparent loss of nonlinear mode coupling in the VMEC solution, as a result of enforcing nested flux surfaces in the final nonlinear state.

While the comparison of this approach with JOREK results for tokamak cases shows that there are limits to the equilibrium models applicability, the approach

offers a complementary, less computationally expensive means of understanding saturated nonlinear MHD states, and so free boundary modelling of stellarators was pursued. This work focused on understanding how to use the VMEC method itself. Simple elliptical tokamak and stellarator equilibria were used for this study. It was shown using poloidal and toroidal Fourier resolution scans that the saturated state is not well defined by enforcing the conservation of helicity alone as a physical constraint. For this reason, it is proposed to use the spike in the plasma current as an additional condition which can determine the most physically meaningful solution computed by VMEC.

Including this physical constraint, the expected nonlinear trends were observed for the dependence of the saturated state on the edge safety factor and external rotational transform. Analysis of the saturated magnetic energy spectrum of stellarator solutions indicates that the energy of the modelled $n = 1$ perturbation is concentrated in the $N_\mathrm{f} = 1$ mode family, as can be expected due to toroidal mode coupling. The observed increase in the computed $n = 0$ poloidal magnetic energy in both VMEC and JOREK computations is attributed to an exchange of energy between the integrated volume and external vacuum region. Finally, a preliminary comparison of the dominant poloidal mode structure observed in VMEC and the JOREK stellarator model, discussed in the next section, showed qualitative agreement, helping to build confidence in both modelling approaches for future studies.

8.3 Steps towards reduced MHD for stellarators

While the simplified models outlined above have been useful in improving the intuition for nonlinear MHD dynamics in stellarators, the final objective of the JOREK group has always been to develop a 3D time evolving approach to modelling stellarators in realistic geometry. Such a model is essential in studying the detailed nonlinear dynamics of optimised stellarators. To that end, a reduced MHD model for stellarators was derived and implemented in parallel to this thesis, as part of a separate thesis project. In support of this work, an equilibrium converter was implemented and tested in Section 7.2, that was used to construct the initial condition for nonlinear MHD simulations of stellarators in JOREK. In addition, a simple test case of resistive modes was designed in Section 7.3. Using the W7-A stellarator, the reduced model implementation was successfully validated against linear growth rates of resistive tearing and ballooning modes in a classical stellarator.

8.4 Future work

There are several directions for future work. In theory, the virtual current model could have been used to study the physics of QA devices with a large external rotational transform using additional physics. Without a critical research question to pursue with the model, such studies were not considered a fruitful use of time.

However, the surprising agreement of W7-X growth rates indicates that this model could prove useful in assisting nonlinear studies of stellarators in the future. The full non-axisymmetric approach is predicted to be computationally expensive, and so it may be helpful to use the virtual current model to first scan the nonlinear parameter space to provide an intuition of the nonlinear dynamics, before embarking on nonlinear studies in full non-axisymmetric geometry.

Considering the use of equilibrium approaches for modelling optimised stellarators, the edge safety factor in such devices is often lower than the stellarators with Ohmic current profiles considered in this thesis. For this reason, it is hoped that the approach can be used to develop preliminary free boundary studies of external modes in optimised stellarators. Appropriate test cases could be external modes in optimised QA stellarators [23], and linear ideal edge perturbations observed on W7-AS [129]. If such studies are successful, they would be helpful both in understanding the dynamics of ideal modes in stellarators, and in providing a future nonlinear benchmark for the models being developed in JOREK.

Lastly, the focus of the JOREK group in the coming years will be the further testing, validation and extension of this model for use with optimised stellarators. Modelling these devices is computationally much more demanding than the classical stellarators that have been considered thus far. Linear benchmarks of the instabilities previously observed in W7-X are intended as the next step to be tackled, as well as the extension of the models to include additional physics such as two-fluid effects and free boundary treatments, which will become relevant depending on the applications considered in future projects.

Bibliography

[1] L Spitzer Jr. Project Matterhorn Report. Technical report, PM-S-1 NYO-993, Princeton University, 1951.

[2] Per Helander, CD Beidler, TM Bird, M Drevlak, Y Feng, R Hatzky, F Jenko, R Kleiber, JHE Proll, Yu Turkin, et al. Stellarator and tokamak plasmas: a comparison. *Plasma Physics and Controlled Fusion*, 54(12):124009, 2012.

[3] Allen H Boozer. Physics of magnetically confined plasmas. *Reviews of modern physics*, 76(4):1071, 2005.

[4] TC Hender, JC Wesley, J Bialek, A Bondeson, AH Boozer, RJ Buttery, A Garofalo, TP Goodman, RS Granetz, Y Gribov, et al. MHD stability, operational limits and disruptions. *Nuclear fusion*, 47(6):S128, 2007.

[5] Francis F Chen. *Introduction to plasma physics*. Springer Science & Business Media, 2012.

[6] J Ongena, R Koch, R Wolf, and H Zohm. Magnetic-confinement fusion. *Nature Physics*, 12(5):398–410, 2016.

[7] AV Burdakov, AA Ivanov, and EP Kruglyakov. Modern magnetic mirrors and their fusion prospects. *Plasma Physics and Controlled Fusion*, 52(12): 124026, 2010.

[8] Alexander Piel. *Single Particle Motion in Electric and Magnetic Fields*, pages 45–71. Springer International Publishing, Cham, 2017. ISBN 978-3-319-63427-2.

[9] H Yamaguchi. A quasi-isodynamic magnetic field generated by helical coils. *Nuclear Fusion*, 59(10):104002, 2019.

[10] A Bader, BJ Faber, JC Schmitt, DT Anderson, M Drevlak, JM Duff, H Frerichs, CC Hegna, TG Kruger, M Landreman, et al. Advancing the physics basis for quasi-helically symmetric stellarators. *Journal of Plasma Physics*, 86(5), 2020.

[11] SA Henneberg, M Drevlak, C Nührenberg, CD Beidler, Y Turkin, J Loizu, and P Helander. Properties of a new quasi-axisymmetric configuration. *Nuclear Fusion*, 59(2):026014, 2019.

[12] Jeffrey P Freidberg. *Ideal MHD*. Cambridge University Press, 2014.

[13] Matt Landreman. Quasisymmetry: a hidden symmetry of magnetic fields, 2019.

[14] Allen H Boozer. Plasma equilibrium with rational magnetic surfaces. *The Physics of Fluids*, 24(11):1999–2003, 1981.

[15] John D Lawson. Some criteria for a power producing thermonuclear reactor. *Proceedings of the physical society. Section B*, 70(1):6, 1957.

[16] Thomas Sunn Pedersen, Ralf König, Maciej Krychowiak, Marcin Jakubowski, Jürgen Baldzuhn, Sergey Bozhenkov, Golo Fuchert, Andreas Langenberg, Holger Niemann, Daihong Zhang, et al. First results from divertor operation in Wendelstein 7-X. *Plasma Physics and Controlled Fusion*, 61(1):014035, 2018.

[17] Matt Landreman and Elizabeth Paul. Magnetic fields with precise quasisymmetry for plasma confinement. *Physical Review Letters*, 128(3):035001, 2022.

[18] AG Peeters. The bootstrap current and its consequences. *Plasma Physics and Controlled Fusion*, 42(12B):B231, 2000.

[19] Hartmut Zohm. *Magnetohydrodynamic stability of tokamaks*. John Wiley & Sons, 2015.

[20] TC Hender, JC Wesley, and J Bialek. MHD stability, operational limits and disruptions [Progress in the ITER Physics Basis (PIPB)]. *Nuclear Fusion*, 47 (6):S128–S202, 2007.

[21] Francisco Javier Artola, P Beyer, G Huijsmans, A Loarte, and M Hoelzl. *Free-boundary simulations of MHD plasma instabilities in tokamaks*. PhD thesis, Aix-Marseille Université, 2018.

[22] GY Fu, LP Ku, WA Cooper, SH Hirshman, DA Monticello, MH Redi, A Reiman, R Sanchez, and DA Spong. Magnetohydrodynamics stability of compact stellarators. *Physics of Plasmas*, 7(5):1809–1815, 2000.

[23] Nuehrenberg C. STELLATOK: Global ideal MHD. Technical report, Max-Planck-Institut für Plasmaphysik, 2017.

[24] ED Fredrickson, MC Zarnstorff, and EA Lazarus. Tearing mode stability of model plasmas in NCSX. *Fusion science and technology*, 51(2):232–237, 2007.

[25] Ming-Sheng Chu and M Okabayashi. Stabilization of the external kink and the resistive wall mode. *Plasma Physics and Controlled Fusion*, 52(12):123001, 2010.

[26] BB Kadomtsev and OP Pogutse. Nonlinear helical perturbations of a plasma in the tokamak. *Sov. Phys. JETP*, 5:575–590, 1973.

[27] Marshall N Rosenbluth, DA Monticello, HR Strauss, and RB White. Numerical studies of nonlinear evolution of kink modes in tokamaks. *The Physics of Fluids*, 19(12):1987–1996, 1976.

[28] GTA Huysmans, TC Hender, and B Alper. Identification of external kink modes in jet. *Nuclear fusion*, 38(2):179, 1998.

[29] P Buratti, M Baruzzo, RJ Buttery, CD Challis, IT Chapman, F Crisanti, L Figini, M Gryaznevich, TC Hender, DF Howell, et al. Kink instabilities in high-beta JET advanced scenarios. *Nuclear Fusion*, 52(2):023006, 2012.

[30] GY Fu. Vertical stability in a current-carrying stellarator. *Physics of Plasmas*, 7(4):1079–1080, 2000.

[31] MC ArchMiller, MR Cianciosa, DA Ennis, JD Hanson, GJ Hartwell, JD Hebert, JL Herfindal, SF Knowlton, X Ma, DA Maurer, et al. Suppression of vertical instability in elongated current-carrying plasmas by applying stellarator rotational transform. *Physics of Plasmas*, 21(5):056113, 2014.

[32] W VII-A Team. Stabilization of the (2, 1) tearing mode and of the current disruption in the W VII–A stellarator. *Nuclear Fusion*, 20(9):1093, 1980.

[33] E Sallander, A Weller, et al. Effects of non-vanishing toroidal current densities on stability in the Wendelstein 7-AS stellarator. *Nuclear fusion*, 40(8):1499, 2000.

[34] A Weller, M Anton, J Geiger, M Hirsch, R Jaenicke, A Werner, W7-AS Team, C Nührenberg, E Sallander, and DA Spong. Survey of magnetohydrodynamic instabilities in the advanced stellarator Wendelstein 7-AS. *Physics of Plasmas*, 8(3):931–956, 2001.

[35] Marco Zanini, HP Laqua, H Thomsen, T Stange, Christian Brandt, H Braune, Kai Jakob Brunner, G Fuchert, M Hirsch, J Knauer, et al. ECCD-induced sawtooth crashes at W7-X. *Nuclear Fusion*, 60(10):106021, 2020.

[36] Y Todo, R Seki, DA Spong, H Wang, Y Suzuki, S Yamamoto, N Nakajima, and M Osakabe. Comprehensive magnetohydrodynamic hybrid simulations of fast ion driven instabilities in a Large Helical Device experiment. *Physics of plasmas*, 24(8):081203, 2017.

[37] Florian Hindenlang, Matthias Hoelzl, and Eric Sonnendrücker. A Parallel 3D DG Framework for Resistive MHD Simulations in Tokamak and Stellarator Geometries. In *25th International Conference on Numerical Simulation of Plasmas (ICNSP 2017)*, 2017.

[38] SC Jardin, N Ferraro, J Breslau, and J Chen. Multiple timescale calculations of sawteeth and other global macroscopic dynamics of tokamak plasmas. *Computational Science & Discovery*, 5(1):014002, 2012.

[39] Carl R Sovinec, Thomas A Gianakon, Eric D Held, Scott E Kruger, Dalton D Schnack, and NIMROD Team. NIMROD: A computational laboratory for studying nonlinear fusion magnetohydrodynamics. *Physics of Plasmas*, 10 (5):1727–1732, 2003.

[40] Yao Zhou, NM Ferraro, SC Jardin, and HR Strauss. Approach to nonlinear magnetohydrodynamic simulations in stellarator geometry. *Nuclear Fusion*, 61(8):086015, 2021.

[41] GTA Huysmans and O Czarny. MHD stability in X-point geometry: simulation of ELMs. *Nuclear fusion*, 47(7):659, 2007.

[42] Matthias Hoelzl, GTA Huijsmans, SJP Pamela, Marina Becoulet, Eric Nardon, Francisco Javier Artola, Boniface Nkonga, CV Atanasiu, Vinodh Bandaru, Ashish Bhole, et al. The JOREK non-linear extended MHD code and applications to large-scale instabilities and their control in magnetically confined fusion plasmas. *Nuclear Fusion*, 61(6):065001, 2021.

[43] Olivier Czarny and Guido Huysmans. Bézier surfaces and finite elements for MHD simulations. *Journal of computational physics*, 227(16):7423–7445, 2008.

[44] SJP Pamela, GTA Huijsmans, M Hoelzl, JOREK Team, et al. A generalised formulation of G-continuous Bezier elements applied to non-linear MHD simulations. *Journal of Computational Physics*, page 111101, 2022.

[45] Nikita Nikulsin, Matthias Hoelzl, Alessandro Zocco, Karl Lackner, and Sibylle Günter. A three-dimensional reduced MHD model consistent with full MHD. *Physics of Plasmas*, 26(10):102109, 2019.

[46] Nikita Nikulsin, Matthias Hoelzl, Alessandro Zocco, Karl Lackner, Sibylle Günter, and the JOREK Team. Testing of the new JOREK stellarator-capable model in the tokamak limit. *Journal of Plasma Physics*, 2021.

[47] Nikita Nikulsin, Rohan Ramasamy, Matthias Hoelzl, Florian Hindenlang, Erika Strumberger, Karl Lackner, Sibylle Günter, and JOREK Team. JOREK3D: An extension of the JOREK nonlinear MHD code to stellarators. *Physics of Plasmas*, 29(6):063901, 2022.

[48] Nikita Nikulsin. Models and methods for nonlinear magnetohydrodynamic simulations of stellarators, 2021.

[49] R Ramasamy, N Nikulsin, K Aleynikova, M Hoelzl, F Hindenlang, E Strumberger, K Lackner, and S Günter. Progress towards nonlinear MHD studies of optimised stellarators using the JOREK code. Poster; 23rd International Stellarator and Heliotron Workshop, Warsaw, Poland, 6 2022.

[50] John M Greene and John L Johnson. Determination of hydromagnetic equilibria. *The Physics of Fluids*, 4(7):875–890, 1961.

[51] Omar Maj. A mathematical introduction to magnetohydrodynamics. In *Vorlesung (SS 2017)*, pages 1–222, 2017.

[52] Jeffrey P Freidberg. *Ideal magnetohydrodynamics*. New York: Plenum Press, 1987.

[53] Steven P Hirshman and JC Whitson. Steepest-descent moment method for three-dimensional magnetohydrodynamic equilibria. *The Physics of fluids*, 26 (12):3553–3568, 1983.

[54] SP Hirshman and DK Lee. MOMCON: a spectral code for obtaining three-dimensional magnetohydrodynamic equilibria. *Computer physics communications*, 39(2):161–172, 1986.

[55] RL Dewar and SR Hudson. Stellarator symmetry. *Physica D: Nonlinear Phenomena*, 112(1-2):275–280, 1998.

[56] F. Hindenlang, O. Maj, E. Strumberger, M. Rampp, and E. Sonnendrücker. GVEC: A newly developed 3D ideal MHD Galerkin Variational Equilibrium Code. Presentation given in Simons Collaboration on Hidden Symmetries and Fusion Energy, 2019.

[57] SR Hudson, RL Dewar, G Dennis, MJ Hole, M McGann, G Von Nessi, and S Lazerson. Computation of multi-region relaxed magnetohydrodynamic equilibria. *Physics of Plasmas*, 19(11):112502, 2012.

[58] IT Chapman, M Becoulet, T Bird, J Canik, M Cianciosa, WA Cooper, T Evans, N Ferraro, C Fuchs, M Gryaznevich, et al. Three-dimensional distortions of the tokamak plasma boundary: boundary displacements in the presence of resonant magnetic perturbations. *Nuclear Fusion*, 54(8):083006, 2014.

[59] AD Turnbull, NM Ferraro, VA Izzo, Edward A Lazarus, J-K Park, WA Cooper, Steven P Hirshman, Lang L Lao, MJ Lanctot, Samuel Lazerson, et al. Comparisons of linear and nonlinear plasma response models for non-axisymmetric perturbations. *Physics of Plasmas*, 20(5):056114, 2013.

[60] Allan Reiman, NM Ferraro, A Turnbull, JK Park, A Cerfon, TE Evans, Matthew J Lanctot, EA Lazarus, Y Liu, G McFadden, et al. Tokamak plasma high field side response to an n= 3 magnetic perturbation: a comparison of 3D equilibrium solutions from seven different codes. *Nuclear Fusion*, 55(6): 063026, 2015.

[61] M Willensdorfer, SS Denk, E Strumberger, W Suttrop, B Vanovac, D Brida, M Cavedon, I Classen, M Dunne, S Fietz, et al. Plasma response measurements of external magnetic perturbations using electron cyclotron emission and comparisons to 3D ideal MHD equilibrium. *Plasma Physics and Controlled Fusion*, 58(11):114004, 2016.

[62] G Suárez López, R Ochoukov, W Tierens, M Willensdorfer, H Zohm, D Aguiam, G Birkenmeier, V Bobkov, M Cavedon, M Dunne, et al. ICRF coupling in ASDEX upgrade magnetically perturbed 3D plasmas. *Plasma Physics and Controlled Fusion*, 61(12):125019, 2019.

[63] G Suárez López, M Cianciosa, T Lunt, W Tierens, R Bilato, G Birkenmeier, V Bobkov, M Dunne, R Ochoukov, E Strumberger, et al. Validation of high-fidelity ion cyclotron range of frequencies antenna coupling simulations in full 3D geometry against experiments in the ASDEX Upgrade tokamak. *Plasma Physics and Controlled Fusion*, 62(12):125021, 2020.

[64] WA Cooper, JP Graves, A Pochelon, O Sauter, and L Villard. Tokamak magnetohydrodynamic equilibrium states with axisymmetric boundary and a 3D helical core. *Physical review letters*, 105(3):035003, 2010.

[65] Andreas Kleiner, JP Graves, Daniele Brunetti, Wilfred Anthony Cooper, Sergei Medvedev, Antoine Merle, and Christer Wahlberg. Current and pressure gradient triggering and nonlinear saturation of low-n edge harmonic oscillations in tokamaks. *Plasma Physics and Controlled Fusion*, 61(8):084005, 2019.

[66] A Weller, AD Cheetham, AW Edwards, RD Gill, A Gondhalekar, RS Granetz, J Snipes, and JA Wesson. Persistent density perturbations at rational-q surfaces following pellet injection in the Joint European Torus. *Physical review letters*, 59(20):2303, 1987.

[67] H Reimerdes, I Furno, F Hofmann, An Martynov, A Pochelon, and O Sauter. Sawtooth behaviour in highly elongated TCV plasmas. *Plasma physics and controlled fusion*, 48(11):1621, 2006.

[68] FD Halpern, D Leblond, H Lütjens, and JF Luciani. Oscillation regimes of the internal kink mode in tokamak plasmas. *Plasma Physics and Controlled Fusion*, 53(1):015011, 2010.

[69] JP Graves, D Brunetti, IT Chapman, WA Cooper, H Reimerdes, F Halpern, A Pochelon, O Sauter, et al. Magnetohydrodynamic helical structures in nominally axisymmetric low-shear tokamak plasmas. *Plasma Physics and Controlled Fusion*, 55(1):014005, 2012.

[70] WA Cooper, D Brunetti, BP Duval, JM Faustin, JP Graves, A Kleiner, H Patten, D Pfefferlé, L Porte, M Raghunathan, et al. Saturated ideal kink/peeling

formations described as three-dimensional magnetohydrodynamic tokamak equilibrium states. *Physics of Plasmas*, 23(4):040701, 2016.

[71] A Kleiner, JP Graves, WA Cooper, T Nicolas, and Christer Wahlberg. Free boundary 3D ideal MHD equilibrium calculations for non-linearly saturated current driven external kink modes in tokamaks. *Nuclear Fusion*, 58(7): 074001, 2018.

[72] Wilfred Anthony Cooper, Daniel López-Bruna, Marian A Ochando, Francisco Castejon, JP Graves, Andreas Kleiner, Samuel Lanthaler, H Patten, Madhusudan Raghunathan, JM Faustin, et al. Stellarator nonlinearly saturated periodicity-breaking ideal magnetohydrodynamic equilibrium states. *Nuclear Fusion*, 58(12):124002, 2018.

[73] Paul R Garabedian. Three-dimensional equilibria in axially symmetric tokamaks. *Proceedings of the National Academy of Sciences*, 103(51):19232–19236, 2006.

[74] AD Turnbull. Plasma response models for non-axisymmetric perturbations. *Nuclear Fusion*, 52(5):054016, 2012.

[75] John Wesson and David J Campbell. *Tokamaks*, volume 149. Oxford university press, 2011.

[76] Hannes Alfvén. Existence of electromagnetic-hydrodynamic waves. *Nature*, 150(3805):405–406, 1942.

[77] GTA Huysmans. External kink (peeling) modes in x-point geometry. *Plasma physics and controlled fusion*, 47(12):2107, 2005.

[78] Carolin Schwab. Ideal magnetohydrodynamics: Global mode analysis of three-dimensional plasma configurations. *Physics of Fluids B: Plasma Physics*, 5(9):3195–3206, 1993.

[79] William A Newcomb. Hydromagnetic stability of a diffuse linear pinch. *Annals of Physics*, 10(2):232–267, 1960.

[80] L Degtyarev, A Martynov, S Medvedev, F Troyon, L Villard, and R Gruber. The KINX ideal MHD stability code for axisymmetric plasmas with separatrix. *Computer Physics Communications*, 103(1):10–27, 1997.

[81] Yueqiang Liu, Anders Bondeson, D Gregoratto, Carl-Magnus Fransson, Y Gribov, and R Paccagnella. Feedback control of resistive wall modes in toroidal devices. *Nuclear fusion*, 44(1):77, 2003.

[82] E. Strumberger and S. Günter. CASTOR3D: linear stability studies for 2D and 3D tokamak equilibria. *Nuclear Fusion*, 57(1):016032, nov 2017. doi:10.1088/0029-5515/57/1/016032.

[83] W Kerner, S Poedts, JP Goedbloed, GTA Huysmans, B Keegan, and E Schwartz. Proceedings of 18th Conference on Controlled Fusion and Plasma Physics, 1991.

[84] E Strumberger, S Günter, P Merkel, and C Tichmann. Linear stability studies including resistive wall effects with the CASTOR/STARWALL code. In *Journal of Physics: Conference Series*, volume 561, page 012016. IOP Publishing, 2014.

[85] E Strumberger and S Günter. Linear stability studies for a quasi-axisymmetric stellarator configuration including effects of parallel viscosity, plasma flow, and resistive walls. *Nuclear Fusion*, 59(10):106008, 2019.

[86] P Merkel and E Strumberger. Linear MHD stability studies with the STARWALL code. *arXiv preprint arXiv:1508.04911*, 2015.

[87] HG Eriksson and C Wahlberg. Nonlinear stability analysis of external hydromagnetic modes in a tokamak. *Plasma physics and controlled fusion*, 39(6): 943, 1997.

[88] Emmanuel Franck, Matthias Hölzl, Alexander Lessig, and Eric Sonnendrücker. Energy conservation and numerical stability for the reduced MHD models of the non-linear JOREK code. *ESAIM: Mathematical Modelling and Numerical Analysis*, 49(5):1331–1365, 2015.

[89] SJP Pamela, A Bhole, GTA Huijsmans, B Nkonga, M Hoelzl, I Krebs, E Strumberger, and JET Contributors. Extended full-MHD simulation of non-linear instabilities in tokamak plasmas. *Physics of Plasmas*, 27(10): 102510, 2020.

[90] Youcef Saad and Martin H Schultz. GMRES: A generalized minimal residual algorithm for solving nonsymmetric linear systems. *SIAM Journal on scientific and statistical computing*, 7(3):856–869, 1986.

[91] Pascal Hénon, Pierre Ramet, and Jean Roman. PASTIX: a high-performance parallel direct solver for sparse symmetric positive definite systems. *Parallel Computing*, 28(2):301–321, 2002.

[92] P. Ghysels, S. L. Xiaoye, C. Gorman, and F. Rouet. A robust parallel preconditioner for indefinite systems using hierarchical matrices and randomized sampling. In *2017 IEEE International Parallel and Distributed Processing Symposium (IPDPS)*, pages 897–906, 2017. doi:10.1109/IPDPS.2017.21.

[93] Giorgio Anania and JL Johnson. Application of the stellarator expansion for plasma stability studies in stellarators. *The Physics of fluids*, 26(10): 3070–3078, 1983.

[94] John M Greene, John L Johnson, Martin D Kruskal, and Lawrence Wilets. Equilibrium and stability of helical hydromagnetic systems. *The Physics of Fluids*, 5(9):1063–1069, 1962.

[95] K Matsuoka, K Miyamoto, K Ohasa, and M Wakatani. Magnetohydrodynamic instabilities in a current-carrying stellarator. *Nuclear Fusion*, 17(6): 1123, 1977.

[96] M Wakatani. Non-linear calculation of the m= 1 internal kink instability in current-carrying stellarators. *Nuclear Fusion*, 18(11):1499, 1978.

[97] Hi R Strauss. Stellarator equations of motion. *Plasma Physics*, 22(7):733, 1980.

[98] M. Wakatani, H. Shirai, H. Zushi, H. Kaneko, O. Motojima, T. Obiki, A. Iiyoshi, and K. Uo. Numerical studies of internal disruptions in Heliotron E. *Nuclear Fusion*, 23(12), 1983. doi:10.1088/0029-5515/23/12/010.

[99] Qingquan Yu, Erika Strumberger, Valentin Igochine, Karl Lackner, Heinrich Laqua, Marco Zanini, Harald Braune, Matthias Hirsch, Udo Höfel, Stefan Marsen, et al. Numerical modeling of the electron temperature crashes observed in Wendelstein 7-X stellarator experiments. *Nuclear Fusion*, 60(7): 076024, 2020.

[100] GTA Huijsmans and A Loarte. Non-linear MHD simulation of ELM energy deposition. *Nuclear Fusion*, 53(12):123023, 2013.

[101] M Hoelzl, P Merkel, GTA Huysmans, E Nardon, E Strumberger, R McAdams, I Chapman, S Günter, and K Lackner. Coupling JOREK and STARWALL codes for non-linear resistive-wall simulations. In *Journal of Physics: Conference Series*, 2012.

[102] R. Ramasamy, G. Bustos Ramirez, M. Hoelzl, J. Graves, G. Suárez López, K. Lackner, and S. Günter. Modeling of saturated external MHD instabilities in tokamaks: A comparison of 3D free boundary equilibria and nonlinear stability calculations. *Physics of Plasmas*, 29(7):072303, 2022. doi:10.1063/5.0090008.

[103] DB Albert. Adiabatic equilibrium calculations of major-radius compression in a tokamak. *Nuclear Fusion*, 20(8):939, 1980.

[104] D Brunetti, JP Graves, E Lazzaro, A Mariani, S Nowak, Wilfred Anthony Cooper, and Christer Wahlberg. Excitation mechanism of low-n edge harmonic oscillations in edge localized mode-free, high performance, tokamak plasmas. *Physical review letters*, 122(15):155003, 2019.

[105] Feng Liu, GTA Huijsmans, A Loarte, Andrea M Garofalo, Wayne M Solomon, Philip B Snyder, M Hoelzl, and L Zeng. Nonlinear MHD simulations of Quiescent H-mode plasmas in DIII-D. *Nuclear Fusion*, 55(11):113002, 2015.

[106] Daniele Brunetti, JP Graves, E Lazzaro, A Mariani, S Nowak, WA Cooper, and Christer Wahlberg. Analytic study on low-external ideal infernal modes in tokamaks with large edge pressure gradients. *Journal of Plasma Physics*, 84(2), 2018.

[107] Xi Chen, Keith H Burrell, Nathaniel M Ferraro, Thomas H Osborne, Max E Austin, Andrea M Garofalo, Richard J Groebner, Gerrit J Kramer, NC Luhmann, George R McKee, et al. Rotational shear effects on edge harmonic oscillations in DIII-D quiescent H-mode discharges. *Nuclear Fusion*, 56(7): 076011, 2016.

[108] Isabel Krebs, Matthias Hoelzl, Karl Lackner, and Sibylle Günter. Nonlinear excitation of low-n harmonics in reduced magnetohydrodynamic simulations of edge-localized modes. *Physics of plasmas*, 20(8):082506, 2013.

[109] Andrea M Garofalo, Keith H Burrell, David Eldon, Brian A Grierson, Jeremy M Hanson, Christopher Holland, Guido TA Huijsmans, Feng Liu, Alberto Loarte, Orso Meneghini, et al. The quiescent H-mode regime for high performance edge localized mode-stable operation in future burning plasmas. *Physics of Plasmas*, 22(5):056116, 2015.

[110] Hugo Peraza-Rodriguez, JM Reynolds-Barredo, Raul Sanchez, J Geiger, V Tribaldos, Steven Paul Hirshman, and M Cianciosa. Extension of the SIESTA MHD equilibrium code to free-plasma-boundary problems. *Physics of Plasmas*, 24(8):082516, 2017.

[111] Samuel A Lazerson, Joaquim Loizu, Steven Hirshman, and Stuart R Hudson. Verification of the ideal magnetohydrodynamic response at rational surfaces in the VMEC code. *Physics of Plasmas*, 23(1):012507, 2016.

[112] Yi-Min Huang, Stuart R Hudson, Joaquim Loizu, Yao Zhou, and Amitava Bhattacharjee. Numerical study of δ-function current sheets arising from resonant magnetic perturbations. *Physics of Plasmas*, 29(3):032513, 2022.

[113] Scott E Kruger, Carl R Sovinec, DD Schnack, and ED Held. Free-boundary simulations of DIII-D plasmas with the NIMROD code. *Computer physics communications*, 164(1-3):34–39, 2004.

[114] Rohan Ramasamy, Matthias Hoelzl, Erika Strumberger, Karl Lackner, and Sibylle Günter. Nonlinear MHD simulations of external kinks in quasi-axisymmetric stellarators using an axisymmetric external rotational transform approximation. *Nuclear Fusion*, 61(7):076017, 2021.

[115] Michael Drevlak, D Monticello, and A Reiman. PIES free boundary stellarator equilibria with improved initial conditions. *Nuclear fusion*, 45(7):731, 2005.

[116] Peter Merkel. Solution of stellarator boundary value problems with external currents. *Nuclear Fusion*, 27(5):867, 1987.

[117] R Ramasamy, M Hoelzl, E Strumberger, N Nikulsin, K Lackner, and S Günter. Towards linear and non-linear assessments of quasi-axisymmetric stellarators. Poster; 22nd International Stellarator and Heliotron Workshop, Madison, USA, 9 2019.

[118] HP Furth, PH Rutherford, and H Selberg. Tearing mode in the cylindrical tokamak. *The Physics of Fluids*, 16(7):1054–1063, 1973.

[119] Q Yu, S Günter, and K Lackner. Numerical modeling of nonlinear growth and saturation of neoclassical tearing modes. *Physics of Plasmas*, 11(1):140–150, 2004.

[120] E Strumberger, S Günter, et al. Linear, resistive stability studies for Wendelstein 7-X-type equilibria with external current drive. *Nuclear Fusion*, 60(10): 106013, 2020.

[121] BB Kadomtsev. Reconnection of field lines and disruptive instability in tokamaks. *ppcf*, 1:555–565, 1977.

[122] R Ramasamy, M Hoelzl, E Strumberger, Q Yu, K Lackner, S Günter, and the JOREK team. Non-linear MHD stability assessments of stellarators using an axisymmetric approximation. Poster; Theory of Fusion Plasmas, Joint Varenna-Lausanne International Workshop, Lausanne, Switzerland, 10 2020.

[123] HA Holties, GTA Huysmans, JP Goedbloed, W Kerner, VV Parail, and FX Soldner. Stability of infernal and ballooning modes in advanced tokamak scenarios. *Nuclear fusion*, 36(8):973, 1996.

[124] JBj Taylor. Relaxation and magnetic reconnection in plasmas. *Reviews of Modern Physics*, 58(3):741, 1986.

[125] Amitava Bhattacharjee and Robert L Dewar. Energy principle with global invariants. *The Physics of Fluids*, 25(5):887–897, 1982.

[126] Meskat, JP and Zohm, H and Gantenbein, G and Günter, S and Maraschek, M and Suttrop, W and Yu, Q and ASDEX Upgrade Team. Analysis of the structure of neoclassical tearing modes in ASDEX Upgrade. *Plasma physics and controlled fusion*, 43(10):1325, 2001.

[127] LA Charlton, RJ Hastie, and TC Hender. Resistive "infernal" modes. *Physics of Fluids B: Plasma Physics*, 1(4):798–803, 1989.

[128] W Dommaschk. Representations for vacuum potentials in stellarators. *Computer physics communications*, 40(2-3):203–218, 1986.

[129] P Merkel, C Nuehrenberg, and WA Cooper. Free-boundary ideal MHD modes in W7-AS, 1996.

Acknowledgements

This thesis belongs first and foremost to my family — to my mother for teaching me perseverance and ambition, my father for teaching me patience and perspective, and my brother for being an anchor point in my life, even though I never asked him to be. Special thanks goes also to my aunt, Indra, for taking an interest in my PhD and being a quiet voice of reason and support in my life. My achievements are your achievements.

Academically speaking, I am greatly indebted to my supervisors. Like all doctorates, this thesis has featured its highs and lows, and I am very grateful to have had Sibylle and Matthias in my corner, doing everything they could to empower me with the knowledge and skills to tackle the challenges at hand. Thanks for your constant and unwavering support. I owe a special thanks also to Karl Lackner, both for regularly meeting to discuss and help me through many of the challenges I encountered during my thesis, even though it was not within his remit to do so, as well as sharing his dedication to plasma physics and fusion with me.

I am also fortunate to have had the chance to work with some great collaborators. Erika Strumberger supported me from the outset of my thesis, and patiently taught me the ins and outs of CASTOR3D, providing me with everything I needed to attack the numerics and physics problems I was presented with, even though tutoring me was not part of my original thesis plan. In a similar vein, I owe Florian Hindenlang for assisting me with the use of GVEC, and interfacing it with JOREK, as well as agreeing to be my scientific advisor, and guiding me on the direction of my career development.

The work using VMEC was greatly assisted by the willingness of Jonathan Graves, Guillermo Bustos Ramirez, and Guillermo Suárez López to collaborate with me on the comparison of VMEC results with JOREK. I would not have been able to progress the work at the rate I did without their assistance. In addition, I have been very fortunate to be part of the lively JOREK community, who have all supported my work in one form or another. To my PhD contemporaries – Andres, Nina, Verena, and Fabian — thanks for being a joy to work with, and sharing with me in the trials and tribulations of being a JOREK user. In particular, I am lucky to have had the opportunity to work directly with Nikita Nikulsin on the stellarator project.

Last but not least, I am grateful to all of the people who have supported me

(old and new) throughout the last 4 years in all sorts of non-academic ways — to Maša and Marlies, in particular, for keeping me grounded during my lowest points, and to Ash, Colin, Danko, Jakob, Jelena, Johanna, Jonas, Katrin, Liliya, Mario, Marko, Matt, Monica and many more, for choosing to incorporate me into your lives. To list everyone would require an end credits roll, which I would not like to do, as I hope that our time together is not over. Thank you for making the last 4 years an unexpected pleasure I was not looking for, but will always treasure.